Università degli Studi di Torino
Scuola di Dottorato

UNIVERSITÀ
DEGLI STUDI
DI TORINO

Study of Quantum Mechanics foundations by exploiting novel paradigms of measurement

Salvatore Virzì

Università degli Studi di Torino
Scuola di Dottorato

Dottorato in Fisica ed Astrofisica

Study of Quantum Mechanics foundations by exploiting novel paradigms of measurement

Salvatore Virzì

Tutor: Dr. Marco Genovese

Contents

Acronyms

BBO - Barium Borate

CHSH - Clauser Horne Shimony Holt

CTC - Close Time-like Curve

EoF - Entanglement of Formation

GQM - Genetic Quantum Measurement

HWP - Half-Wave Plate

IF - Interference Filter

LBO - Lithium Triborate

OoI - Observable of Interest

OTC - Open Time-like Curve

PBS - Polarizing Beam Splitter

PDC - Parametric Down Conversion

PDO - Pseudo-Density Operator

PM - Protective Measurement

POVM - Positive Operator-Valued Measurement

QFI - Quantum Fisher Information

QGD - Quantum Geometric Discord

QM - Quantum Mechanics

QO - Quantum Optics

QWP - Quarter-Wave Plate

RoI - Region of Interest

SHG - Second-Harmonic Generation

SLD - Symmetric Logarithmic Derivative

SMF - Single-Mode Fiber

SPAD - Single-Photon Avalanche Diode

SPS - Single-Photon Source

SWM - Sequential Weak Measurement

Chapter 1

Introduction

Measurements are the fundamental tool of physics. In the past, to every progress in measurement capability, progresses corresponded both in fundamental science and technology, especially in the Quantum Mechanics (QM) framework.

In the last decades, novel quantum measurement paradigms have been introduced, paving the way to the fast, widespread development of quantum technologies, e.g. Quantum Information, Quantum Metrology, and Quantum Sensing. In particular, the recent scientific progress in quantum optics, atomic physics and nanotechnologies concerning the generation and manipulation of single quantum systems, gave rise to a second *quantum revolution*, based on the specific QM principles pertaining such systems, with predictions of a huge economic and social improvement in the next future.

Currently, the cutting-edge quantum technology is quantum cryptography [1–4]. Quantum key distribution (QKD) [5] devices, already marketed by a few companies, received a huge interest due to the need of communication security in our society. This is due to the fact that QKD security is granted by the laws of QM, differently from "traditional" cryptography algorithms, where the security is only computational and can be compromised by hardware progresses. Indeed, the security of present cryptographic protocols, as the Rivest-Shamir-Adleman (RSA) [6], can be threatened by the development of another relevant quantum technology, i.e. quantum computation [5].

Quantum computers allow resolving particular computational tasks much more efficiently with respect to their classical counterparts, the most relevant example being the implementation of Shor's algorithm [7], exploiting QM for factorizing prime numbers in a polynomial time with respect to the input length, instead of the exponential one needed by classical computers. At the state of the art, there are different approaches for realizing quantum processors [8–11] and, recently, the so-called *quantum supremacy* was achieved [12], i.e. the certification of a dramatic increase in speed compared with all known classical algorithms.

Quantum technologies look promising also in other frameworks. An emblematic example is represented by *quantum enhanced* measurement, e.g. quantum imaging and quantum sensing [13], developed in the last years and allowing to go beyond the limits of their respective classical counterparts. For example, quantum imaging techniques are able to surpass the so-called *shot noise* resolution limit [14,15], finding several applications in scenarios where there is a requirement for low-photon-flux illumination (e.g. with biological samples).

Finally, quantum technologies play a relevant role in the so-called "blue sky" research. To give an example, by exploiting quantum optics [16, 17] techniques it is possible to go beyond the *standard quantum limit* in interferometry [18], allowing better signal-to-noise

ratios in experimental setups for detecting gravitational waves [19], or for testing quantum gravity theories [20].

During my PhD studies, I exploited the techniques of quantum optics in order to inspect some aspects of QM foundations. In particular, I was involved in experimental research for novel measurement paradigms in QM applied onto single- and two-photon states, investigating quantum correlations such as the entanglement, temporal correlations, etc.

This thesis, is structured as follows: after this introductory chapter about the the QM formalism, in chapter 2 I describe the quantum optics techniques mostly exploited during my PhD work. Then, in chapters 3, 4 and 5 I present the experiments in which I was involved, regarding the study and the utilization of quantum correlations for achieving novel paradigm of measurements in QM. Finally, the conclusions are discussed in chapter 6.

1.1 The Quantum Mechanics postulates

Here we introduce the key concepts of the mathematical formulation of QM, together with the peculiar QM properties stemming from them, that will be used in the rest of this thesis.

1.1.1 Quantum states

Postulate I: Associated with any isolated physical system is a complex vector space with inner product (i.e. a Hilbert space) known as the *state space* of the system. The system is completely described by its *state vector*, which is a unit vector in the system's state space.

Into a n-dimensional Hilbert space $\mathcal{H}$, it is possible to identify infinite sets composed of n vectors $|\phi_i\rangle$, that follow the properties:

$$\begin{aligned} &\langle\phi_i|\phi_j\rangle = \delta_{ij} \\ &\sum_{i=1}^{n} |\phi_i\rangle\langle\phi_i| = \mathbb{1}_n \end{aligned} \tag{1.1}$$

where $\langle\phi_i|\phi_j\rangle$ is the inner product between the vectors $|\phi_i\rangle$ and $|\phi_j\rangle$, $|\phi_i\rangle\langle\phi_i|$ indicates the external product between $\langle\phi_i|$ and $|\phi_i\rangle$, δ_{ij} is the Kronecker delta, and $\mathbb{1}_n$ is the n-dimensional identity matrix. Each set $\mathcal{B} = \{|\phi_i\rangle\}$ composed by n vectors satisfying the conditions in Eq. 1.1 is (by definition) a complete orthonormal basis for the space $\mathcal{H}$.

A *pure* state $|\psi\rangle \in \mathcal{H}$ can be described as a linear combination of the vectors belonging to a complete orthonormal basis $\mathcal{B}$:

$$|\psi\rangle = \sum_{i=1}^{n} \alpha_i |\phi_i\rangle \quad , \quad \alpha_i \in \mathbb{C} \quad : \quad \sum_{i=1}^{n} |\alpha_i|^2 = 1 \tag{1.2}$$

Furthermore, a physical system can be in a *mixed* state, i.e. a statistical mixture of pure states $\rho = \sum_i c_i |\psi_i\rangle\langle\psi_i|$, with $c_i \in [0;1]$ and $\sum_i c_i = 1$. The quantity ρ takes the name of density operator, and it will be discussed in section §1.2.

1.1.2 Quantum observables

Postulate II: With each observable physical quantity A it is associated a self-adjoint operator $\hat{A}$, defined on the Hilbert space $\mathcal{H}$. The ensemble of the possible measurement outcomes of A is given by the eigenvalues spectrum of the operator $\hat{A}$.

Since $\hat{A}$ is self-adjoint, it is a linear operator. Then, if it has finite dimensions, it can be decomposed in a matrix form with respect to any basis of $\mathcal{H}$, and its spectrum consists of real eigenvalues only. The set of the $\hat{A}$ eigenvectors $|v\rangle$, i.e. the vectors defined by the eigenvalues equation $\hat{A}|v\rangle = v|v\rangle$ (where v is the eigenvalue corresponding to the eigenvector $|v\rangle$), constitutes a basis for $\mathcal{H}$.

Two operators $\hat{A}, \hat{B} \in \mathcal{H}$ are said to *commute* if it is valid the relation:

$$\left[\hat{A}, \hat{B}\right] = (\hat{A}\hat{B} - \hat{B}\hat{A}) = 0 \tag{1.3}$$

In this case, they also share the same eigenvectors basis. From this point, the hat over the operators will be implied in order to simplify the notation.

1.1.3 Quantum measurement

Postulate III: A measurement in QM is described by a complete set $\{M_m\}$ of operators [21] in $\mathcal{H}$, where the subscript m indicates one of the possible measurement outcomes. The measurement entails the collapse of $|\psi\rangle$ onto the eigenspace to which the eigenvector corresponding to the obtained eigenvalue belongs:

$$|\psi'\rangle = \frac{M_m|\psi\rangle}{\sqrt{\langle\psi|M_m^\dagger M_m|\psi\rangle}} \tag{1.4}$$

In order to be complete, the set $\{M_m\}$ must obey the relation $\sum_m M_m^\dagger M_m = \mathbb{1}$. The probability to obtain the outcome m is given by:

$$p(m) = \langle\psi|M_m^\dagger M_m|\psi\rangle \tag{1.5}$$

1.1.4 Quantum systems evolution

Postulate IV: The evolution of a closed quantum system is described by a unitary transformation.

Being the system at time t_1 in the state $|\psi(t_1)\rangle$, the evolution postulate states that, at time t_2, the system will evolve as:

$$|\psi(t_2)\rangle = U(t_1, t_2)|\psi(t_1)\rangle \tag{1.6}$$

where $U(t_1, t_2)$ is a unitary operator.

This postulate can be rephrased by exploiting the Schrödinger equation, i.e. the evolution of a closed quantum system is described by:

$$i\hbar\frac{\partial}{\partial t}|\psi(t)\rangle = H|\psi(t)\rangle \tag{1.7}$$

where $\hbar$ is the reduced Planck constant, and H is the operator corresponding to the system Hamiltonian.

1.2 Density operator

An alternative representation of a quantum system can be obtained by using the density operator formalism [5]. Given a generic quantum state $|\psi\rangle$, its corresponding density operator is:

$$\rho = \sum_i p_i |\psi_i\rangle\langle\psi_i| \quad , \quad p_i \in [0,1] \quad : \quad \sum_i p_i = 1 \tag{1.8}$$

where p_i is the probability associated with the pure state $|\psi_i\rangle$.

The QM postulates can be rewritten for this formalism. For example, the temporal evolution of the ρ in Eq. 1.8 is given by:

$$\rho(t_1) = \sum_i p_i |\psi_i(t_1)\rangle\langle\psi_i(t_1)| \xrightarrow{U} \rho(t_2) = \sum_i p_i U|\psi_i(t_1)\rangle\langle\psi_i(t_1)|U^\dagger = U\rho(t_1)U^\dagger \tag{1.9}$$

where, again, U is the unitary operator presented above.

By definition, a density operator must satisfy the following properties:

- being a self-adjoint operator;
- being semi-definite positive;
- having unit trace ($\mathrm{Tr}\,[\rho] = 1$).

It follows from the definition of ρ that:

$$\mathrm{Tr}\left[\rho^2\right] \begin{cases} = 1 & \text{for pure states} \\ < 1 & \text{for mixed states} \end{cases} \tag{1.10}$$

Another useful property is that, as stated from the 2nd QM postulate, the density matrix elements can be expressed with respect to any basis composed by the external product between the elements of a physical observable eigenvectors set. that will be used in the rest of this thesis.

1.3 The qubit: the quantum-mechanical extension of the bit

In computer language, the *bit* is a classical state able to assume value 0 or 1, and it represents the foundation of classical computation. In QM, the concept of bit is extended to the *quantum bit* (qubit). Starting from a two-level quantum system and fixing the computational basis $\{|0\rangle, |1\rangle\}$, the qubit si defined as:

$$|\psi\rangle = \alpha|0\rangle + \beta|1\rangle \quad , \quad \alpha, \beta \in \mathbb{C} \quad : \quad |\alpha|^2 + |\beta|^2 = 1 \tag{1.11}$$

Being $|e_1^Q\rangle$ and $|e_2^Q\rangle$ two vectors forming a complete orthonormal basis for the qubit Q, a N qubits state can be expressed as a function of the complete orthonormal basis $\mathcal{B}$, whose elements are given by the tensorial products of the N qubits basis vectors. Therefore, for $N = 2$, the whole state of the qubits A and B is:

$$|\psi_{AB}\rangle = \sum_{i=1}^{2}\sum_{j=1}^{2} \alpha_{ij}|e_i^A\rangle \otimes |e_j^B\rangle \quad , \quad \alpha_{ij} \in \mathbb{C} \quad : \quad \sum_{i,j} |\alpha_{ij}|^2 = 1 \tag{1.12}$$

In the following, we will use the notation $|e_i e_j\rangle \equiv |e_i^A\rangle \otimes |e_j^B\rangle$, in which it is implicit that the left element belongs to the A qubit basis, while the right one belongs to the B qubit basis.

The qubit is the foundation element of quantum information, and it grants several advantages with respect to its classical counterpart, e.g. the fact that it is not bound to be either "0" or "1", but it can be found in a state that is a superposition of the two. This fact is at the base of *quantum parallelism* [5], one of the key features of quantum computers, granting than the possibility to solve several computational problems in a much more efficient way with respect to their classical counterparts.

Another fundamental resource for quantum computation (as well as for other quantum technologies) is represented by quantum correlations within a multi-qubit system, e.g. the entanglement, described in the following section.

1.4 Entanglement

A multi-partite pure quantum state is defined *entangled* if it cannot be expressed as a tensorial product of mono-partite subsystems, i.e. if it is not separable. Analogously, exploiting the density operator formalism, a quantum state is entangled if its density matrix cannot be decomposed as a tensorial product of mono-partite density operators. In the case of bipartite states, this relation can be written as:

$$\rho^{(AB)} \text{ is entangled} \quad \Longleftrightarrow \quad \rho^{(AB)} \neq \sum_{i,j} \omega_{ij} \rho_i^{(A)} \otimes \rho_j^{(B)} \quad , \quad \forall \omega_{ij} \in [0;1] \quad : \quad \sum_{i,j} \omega_{ij} = 1 \tag{1.13}$$

An example of entangled two-qubit states is given by the Bell states [5], that form a complete orthonormal basis in $\mathbb{C}^4$:

$$\begin{aligned} |\phi_+\rangle &= \frac{|00\rangle + |11\rangle}{\sqrt{2}} \\ |\phi_-\rangle &= \frac{|00\rangle - |11\rangle}{\sqrt{2}} \\ |\psi_+\rangle &= \frac{|01\rangle + |10\rangle}{\sqrt{2}} \\ |\psi_-\rangle &= \frac{|01\rangle - |10\rangle}{\sqrt{2}} \end{aligned} \tag{1.14}$$

Historically, $|\psi_-\rangle$ is dubbed *singlet* state, while the three remaining Bell states are called *triplet* states, in analogy with the case of two entangled spin-1/2 particles.

The most important property of an entangled state is that, if one measures just one of the subsystems, the whole state collapses. For example, taking into account the singlet state $|\psi_-\rangle$, if the outcome of the measurement of the first qubit is 0 (1), then the second one collapses onto the state $|1\rangle$ ($|0\rangle$) even without undergoing a measurement.

Such property is due to the *non-local* behavior of QM, i.e. actions on a subsystem can affect the other subsystems of the global state, even though they are space-like separated. This opened a strong debate in the last century, started by the well known article of Einstein, Podolsky and Rosen (EPR) [22], because at that time this was in plain disagreement with the idea of completeness of a physical theory. Even if the debate whether QM is a complete theory and probabilities have a non-epistemic character (i.e. nature is intrinsically probabilistic) or whether it is a statistical approximation of a deterministic theory and probabilities are due to our ignorance of some parameters (i.e. they are epistemic) dates to the beginning of the theory itself, the EPR paper rose this question by considering an explicit example [22]. For this purpose, they introduced the concept of "element of reality" according to the following definition: if, without disturbing in any way a system,

one can predict without any uncertainty the value of a physical quantity, then there is an element of physical reality corresponding to this quantity (i.e. introducing the hypothesis of realism). They formulated also the reasonable hypothesis (in light of special relativity) that any non-local action was forbidden. A theory is complete when it describes every element of reality.

They concluded that either one of their premises was wrong or Quantum Mechanics was not a complete theory, in the sense that not every element of physical reality had a counterpart in the theory.

More in details, they considered a system consisting of two particles prepared in a state such that the sum of their momenta $(p_1 + p_2)$ and the difference of their positions $(x_1 - x_2)$ were both defined at the same time (situation possible in QM, since they correspond to commuting operators). The case in which $(x_1 - x_2)$ and $(p_1 + p_2)$ have eigenvalues a and 0, respectively, is described in QM by a Dirac delta function $\delta(x_1 - x_2 - a)$. This is an example of an entangled state: a state of two or more particles which cannot be factorized in single-particle states. By measuring the position of particle 1 (2), one can predict with certainty the position of particle 2 (1), without disturbing it in any way (although, at the moment of the measurement, the two particles might be very far from each other). Position of particle 2 (1) is therefore an element of reality, according to the previous definition. On the other hand, a measurement of particle 1 (2) momentum allows one to infer momentum of particle 2 (1) without acting on it, thus also momentum of particle 2 (1) must be an element of reality. Anyway, according to QM position and momentum are conjugate variables, and perfect knowledge of one of them implies complete ignorance on the value of the other: therefore, QM cannot predict all elements of reality, and thus it cannot be a complete theory.

Within this debate emerged the development of the so-called local hidden variable theories: namely, of the proposal that there exists a deterministic (and local) theory describing nature, where the precise value of all the observables of a physical system are fixed by some unknown variables (the hidden variables). Quantum Mechanics would only be a statistical approximation of this theory.

After some decades, Bell proved [23] that the quantum phenomena cannot be explained by any local hidden variable theory, by introducing a set of inequalities that only non-classical states can violate. In order to explain this concept, I will illustrate the Clauser-Horne-Shimony-Holt (CHSH) inequality [24], one of the best known Bell inequalities.

Imagine it is performed an experiment, schematized in Fig. 1.1, involving two observers: Alice and Bob. A third person, Charlie, prepares two-particle states. It does not matter how he prepares the particles, just that he is able to repeat the experimental procedure which he uses. Once he has performed the preparation, for each copy of the state he sends one particle to Alice, and the other one to Bob.

Once Alice receives her particle, she performs a measurement on it. She has available two different measurement apparatuses, so she can choose to do one of two different measurements. These measurements are of physical properties which are labeled P_Q and P_R respectively. She does not know in advance which measurement she will perform, because it is chosen randomly for each particle. Here, it is supposed for simplicity that the measurements can each have one of two outcomes, ± 1.

Suppose also that Alice's particle has a value Q for the property P_Q. Q is assumed to be an *objective property* of Alice's particle, which is merely revealed by the measurement, much as we imagine the position of a tennis ball to be revealed by the particles of light being scattered off it. Similarly, let R denote the value revealed by a measurement of the property P_R.

Figure 1.1: Schematic experimental setup for the Bell inequalities. Alice can choose to measure either Q or R, and Bob chooses to measure either S or T . They perform their measurements simultaneously. Alice and Bob are assumed to be space-like separated, i.e. far enough apart that performing a measurement on one system can not have any effect on the measurement results on the other.

Analogously, Bob randomly measures one fo the two properties P_S or P_T, achieving the corresponding existing value S or T, each taking value ± 1.

The timing of the experiment is arranged so that Alice and Bob do their measurements simultaneously (or, more precisely, in a causally-disconnected manner). Therefore, Alice's measurement cannot disturb the result of Bob's one (or vice ve), since physical influences cannot propagate faster than light.

Now, let us consider the quantity:

$$\mathcal{I} \equiv RS + QS + RT - QT = (R+Q)S + (R-Q)T \tag{1.15}$$

Since $R, Q = \pm 1$, then either $(R+Q)S = 0$ or $(R-Q)T = 0$. In either case, it follows that $\mathcal{I} = \pm 2$.

Next, suppose that $p(q,r,s,t)$ is the probability that, before the measurements are performed, the system is in a state where $Q = q$, $R = r$, $S = s$, and $T = t$. These probabilities can depend on how Charlie prepares the two-particle states, and on experimental noise. Then the expectation value of the quantity $\mathcal{I}$ defined in Eq. 1.15 is:

$$\begin{aligned} E(\mathcal{I}) &= \sum_{q,r,s,t} p(q,r,s,t)(rs + qs + rt - qt) \\ &\leq \sum_{q,r,s,t} p(q,r,s,t) \times 2 = 2 \end{aligned} \tag{1.16}$$

In addition, one can reformulate $E(\mathcal{I})$ as:

$$\begin{aligned} E(\mathcal{I}) &= \sum_{q,r,s,t} p(q,r,s,t)rs + \sum_{q,r,s,t} p(q,r,s,t)qs + \sum_{q,r,s,t} p(q,r,s,t)rt - \sum_{q,r,s,t} p(q,r,s,t)qt \\ &= E(RS) + E(QS) + E(RT) - E(QT) \end{aligned} \tag{1.17}$$

Comparing the Eqs. 1.16 and 1.17, one obtains the CHSH inequality:

$$E(RS) + E(QS) + E(RT) - E(QT) \leq 2 \tag{1.18}$$

By repeating the experiment many times, Alice and Bob can determine each quantity on the left hand side of the CHSH inequality. For example, after finishing a set of experiments, Alice and Bob get together to analyze their data. They look at all the experiments where Alice measured P_Q and Bob measured P_S. By averaging over this sample, they can estimate $E(QS)$ to an accuracy only limited by the number of experiments they performed. Analogously, they can estimate all the other quantities on the left hand side of the CHSH inequality, and then check whether it is fulfilled in a real experiment.

However, if Charlie starts to produce quantum entangled bipartite states, e.g. identical copies of the singlet state $|\psi_-\rangle$ defined in Eq. 1.14, the scenario can radically change.

Suppose that Charlie sends the first qubit to Alice, and the second qubit to Bob. Then, they perform measurements of the following observables:

$$\begin{aligned} Q &= Z \qquad S = -\frac{Z+X}{\sqrt{2}} \\ R &= X \qquad T = \frac{Z-X}{\sqrt{2}} \end{aligned} \tag{1.19}$$

where X and Z indicate the first and the third 2×2 Pauli matrices, respectively.

Using the QM formalism, the expectation values of the observables involved in Eq. 1.18 are:

$$\langle RS\rangle = \langle QS\rangle = \langle RT\rangle = \frac{1}{\sqrt{2}} \; ; \; \langle QT\rangle = -\frac{1}{\sqrt{2}} \tag{1.20}$$

Thus, for the singlet state, we obtain:

$$\langle RS\rangle + \langle QS\rangle + \langle RT\rangle - \langle QT\rangle = 2\sqrt{2} \tag{1.21}$$

violating the CHSH inequality in Eq. 1.18.

This means that one or more of the assumptions made for the derivation of the Bell inequality must be incorrect. There are two assumptions needed for the proof of Eq. 1.18 which are questionable. The first assumption is that the involved physical properties have definite values, which exist independently with respect to a possible observation. This is known as the assumption of *realism*. The second one is that Alice performing her measurement does not influence the result of Bob's measurement, known as the assumption of *locality*.

These two assumptions together are known as *local realism*. Intuitively, they are plausible assumptions about how the world works, and they fit our everyday experience. However, Bell inequalities show that at least one of these assumptions is not correct.

Experimentally, the violation of a Bell's inequality exploiting entangled state is proved by a number of works, e.g. the loophole-free ones [25, 26], demonstrating that a local hidden variable theory cannot explain quantum phenomena.

1.5 Measurement in Quantum Mechanics

As mentioned before, measurement operations in QM follow the 3rd postulate. This causes some peculiarities completely new with respect to classical measurement, e.g. the wave function collapse, that makes not possible subsequent nor simultaneous measurements of two non-commuting observables.

In this section, it is described the concept of *projective* measurement, that comes out directly from the 3rd QM postulate. Furthermore, Positive Operator-Valued Measurement

(POVM) [5] is introduced, and it is shown a formalism describing *indirect* measurements in QM.

1.5.1 Projective measurements

As stated by the 3rd QM postulate, the measured state undergoes a projection onto the eigenvector corresponding to the obtained eigenvalue. For this reason, "traditional" quantum measurements are usually dubbed as projective measurements.

The projective measurement of a quantum observable is represented by a self-adjoint operator $M \in \mathcal{H}$. It is possible to define M by exploiting its decomposition in the projector basis:

$$M = \sum_m m\Pi_m \tag{1.22}$$

where the sum is extended to all the possible eigenvalues m of the observable spectrum, and $\Pi_m = |\phi_m\rangle\langle\phi_m|$ is the projection operator onto the eigenstate $|\phi_m\rangle$, corresponding to the eigenvalue m.

Being the system before the measurement in the quantum state represented by the density matrix ρ, the probability to obtain as an outcome the eigenvalue m is:

$$p(m) = \mathrm{Tr}\left[\rho\Pi_m\right] \tag{1.23}$$

Then, following the measurement postulate, after the measurement the system collapses into the state:

$$|\psi'\rangle = \frac{\Pi_m|\psi\rangle}{\sqrt{p(m)}} = |\phi_m\rangle \tag{1.24}$$

where $|\phi_m\rangle$ was defined in Eq. 1.2 .

By definition, the expectation value of a projective measurement M related to a quantum observable is given by:

$$\begin{aligned}\mathbf{E}(M) &= \sum_m m\, p(m) = \sum_m \langle\psi|\Pi_m|\psi\rangle \\ &= \langle\psi|\left(\sum_m \Pi_m\right)|\psi\rangle = \langle\psi|M|\psi\rangle \equiv \langle M\rangle\end{aligned} \tag{1.25}$$

where, again, m indicates a possible eigenvalue (outcome), and $p(m)$ its related probability, defined in Eq. 1.23.

Therefore, experimentally it is required a statistically-relevant sample of N identical copies of the state $|\psi\rangle$ for extracting the expectation value $\mathbf{E}(M)$, and the related uncertainty is given by the standard deviation:

$$\sigma_M = \sqrt{\frac{\langle M^2\rangle - \langle M\rangle^2}{N}} \tag{1.26}$$

1.5.2 Positive operator-valued measure formalism

The quantum measurement postulate involves two elements. First, it provides a description for the measurement statistics, that is, the respective probabilities of the different possible measurement outcomes defined in Eq. 1.23. Second, it gives a rule describing the post-measurement state of the system (Eq. 1.24). However, for some applications the post-measurement state of the system could result of little interest, with the main item of interest being the probabilities of the respective measurement outcomes.

In such instances, there is a mathematical tool known as the POVM formalism, focused on the analysis of the measurement results. Let us consider the measurement of the state $|\psi\rangle$ realized by the operators M_m. Exploiting Eq. 1.5, it is possible to associate with each operator M_m the probability $p(m) = \langle\psi|M_m^\dagger M_m|\psi\rangle$.

Suppose to define the operator E_m as:

$$E_m \equiv M_m^\dagger M_m \tag{1.27}$$

From the 3rd postulate and elementary linear algebra, it is immediate to demonstrate that E_m is positive defined. In addition, $\sum_m E_m = \mathbb{1}$ and $p(m) = \langle\psi|E_m|\psi\rangle$. Thus, the set of operators E_m is sufficient to determine the probabilities of the different measurement outcomes. Such operators are known as the POVM elements associated with the measurement, and the complete set $\{E_m\}$ constitutes the POVM.

Projective measurements are a specific case of POVM, because the projectors observe the equality $\Pi_m = E_m$.

1.5.3 Indirect quantum measurements

The measurement postulate and the POVM formalism do not take into account the measurement apparatus and its interaction with the measured system. To amend this, the indirect quantum measurement scheme is introduced.

Such scheme exploits an additional degree of freedom, in which ancillary observables are defined able to extract information about the measured observable, by knowing the interaction between the state $|\psi\rangle$ and the measurement device. Considering an observable of interest (OoI) with its associated operator A in the Hilbert space $\mathcal{H}_A$, a related orthonormal and complete basis $\mathcal{B}_A$ is composed of the $\mathcal{H}_A$ eigenstates $|\psi_i\rangle$, with $i = 1, 2, \ldots, \dim\mathcal{H}_A$, from which the projectors $\Pi_i = |\psi_i\rangle\langle\psi_i|$ are defined.

For simplicity, in this dissertation the Hamiltonian associated with A is considered null, being ρ_0^A the initial density matrix of the measured system.

The indirect measurement of the OoI is performed onto the *meter* operator $\mathcal{M}$ acting in the ancillary Hilbert space $\mathcal{H}_\mathcal{M}$. A set of eigenvectors $|x_k\rangle$, with $k = 1, 2, \ldots, \dim\mathcal{H}_\mathcal{M}$, is associated with the meter, and it constitutes an orthonormal and complete basis in $\mathcal{H}_\mathcal{M}$, as stated by the 1st and the 2nd QM postulates.

Again, the Hamiltonian related to $\mathcal{M}$ is supposed to be null, and the meter is prepared into the initial state $|x^{(0)}\rangle$. Then, the meter (initial) density matrix is $\rho_0^x = |x^{(0)}\rangle\langle x^{(0)}|$.

In this indirect approach, the total system $\mathcal{T}$ is given by the union of meter and OoI, i.e. the global state is defined into the Hilbert space $\mathcal{H}_\mathcal{T} = \mathcal{H}_\mathcal{M} \otimes \mathcal{H}_A$.

The density matrix related to the initial state is:

$$\rho_0 = \rho_0^x \otimes \rho_0^A \tag{1.28}$$

Therefore, the initial state of $\mathcal{T}$ is separable, i.e. not entangled.

The corresponding Hamiltonian is given by:

$$H_\mathcal{T} = H_\mathcal{M} + H_A + H_{int} = H_{int} \tag{1.29}$$

where $H_\mathcal{M}$ and H_A are the meter and the OoI Hamiltonians respectively (null for simplicity, as mentioned before), whereas H_{int} is the Hamiltonian describing the interaction between measured system and measurement apparatus.

As established by the 4th QM postulate, the initial state of the total system $\mathcal{T}$ will evolve in time undergoing the action of an unitary operator U in what is called *pre-measurement*:

$$\rho_0 = \rho_0^x \otimes \rho_0^A \xrightarrow{U} U(\rho_0^x \otimes \rho_0^A)U^\dagger \equiv \rho_1 \tag{1.30}$$

For this evolution to be considered a pre-measurement with respect to A, the operator U has to be able to discriminate between states that compose the basis $\mathcal{B}_A = \{|\psi_i\rangle\}$ defined above. By assuming that the initial state of the overall system $|\Psi_{in}\rangle = |x^{(0)}\rangle \otimes |\psi_i\rangle$ is pure, it evolves as:

$$|\Psi_{in}\rangle = |x^{(0)}\rangle \otimes |\psi_i\rangle \xrightarrow{U} U(|x^{(0)}\rangle \otimes |\psi_i\rangle) = |x^{(i)}\rangle \otimes |\psi_i\rangle \tag{1.31}$$

where $i = 1, 2, \ldots, \dim\mathcal{H}_A$, and the meter state $|x^{(i)}\rangle$ acts as an indicator of $|\psi_i\rangle$. The linearity of QM allows extending this treatise to the case in which the initial measured state is in a superposition of eigenstates belonging to the basis:

$$|x^{(0)}\rangle \otimes |\psi\rangle \xrightarrow{U} U(|x^{(0)}\rangle \otimes |\psi\rangle) = \sum_{i=1}^{\dim\mathcal{H}_A} |x^{(i)}\rangle \otimes |\psi_i\rangle \tag{1.32}$$

Remembering Eq. 1.30, the evolution of the total state density matrix during the pre-measurement is given by:

$$\begin{aligned} \rho_0 \xrightarrow{U} \rho_1 &= U(\rho_0^x \otimes \rho_0^A)U^\dagger \\ &= \sum_{i,j} \Big(|x^{(i)}\rangle \otimes |\psi_i\rangle\langle\psi_i|\rho_0^A|\psi_j\rangle\langle x^{(j)}| \otimes \langle\psi_j| \Big) \\ &= \sum_{i,j} \Big(|x^{(i)}\rangle\Pi_i\rho_0^A\Pi_j\langle x^{(j)}| \Big) \end{aligned} \tag{1.33}$$

where $\Pi_i = |\psi_i\rangle\langle\psi_i|$.

From Eq. 1.33 one can observe that:

- The eigenstates $|\psi_i\rangle$ are still unchanged;
- After the pre-measurement evolution, the total system state becomes entangled;
- In general, the meter states $|x^{(i)}\rangle$ are not eigenstates of the operator $\mathcal{M}$, then the temporal evolution correlates the state $|\psi_i\rangle$ with the meter one in a non-univocal way, i.e $\langle x^{(i)}|x^{(j)}\rangle \neq \delta_{ij}$, since the states $|x^{(i)}\rangle$ and $|x^{(j)}\rangle$ might be non-orthogonal.

By performing a projective measurement of the meter observable $\mathcal{M}$, one obtains:

$$\rho_2 = \sum_k \frac{(\Pi_{x_k} \otimes \mathbb{1}_A)\rho_1(\Pi_{x_k} \otimes \mathbb{1}_A)}{p(x_k|\rho_1)} \tag{1.34}$$

where $\mathbb{1}_A$ is the unity matrix in $\mathcal{H}_A$, the x_k are the eigenvalues of the meter eigenvectors $|x_k\rangle$ (with $\Pi_{x_k} = |x_k\rangle\langle x_k|$), and $p(x_k|\rho_1)$ is the probability to obtain the eigenvalue x_k given the (pre-measurement) state ρ_1, defined in Eq. 1.33. Finally, by partially tracing ρ_2 with respect to the meter, it is possible to extract the information about the OoI.

An example of indirect measurement approach is given by the von Neumann protocol [27], presented in section §4.1.

After this brief introduction of the QM formalism foundations, in the next chapter the quantum optics theoretical framework is presented.

Chapter 2

From blackboard to lab: quantum optics

Quantum optics (QO) [16, 17] is the scientific discipline that deals with optical phenomena when quantization of the optical field cannot be neglected. We can recognize three general approaches in the progressive development of the theory to light: classical, semi-classical and quantum approach.

Despite Planck's *quanta* hypothesis for the black-body radiation and Einstein's theory of the photoelectric effect appeared at the beginning of 20th century, the real QO development started after the realization of the laser. The first unambiguous quantum optical effect was introduced by Glauber [28] in 1963, with the description of new states of light having different statistical properties to those of classical light.

Nowadays, QO phenomena are both a very important tool for studying the very foundations of Quantum Mechanics, and a key feature of many rising quantum technologies.

2.1 Nonlinear optics

Nonlinear optics [16, 29] is the study of phenomena that occur as a consequence of the nonlinear behavior of a dielectric interacting with intense electromagnetic fields. Typically, only laser light is sufficiently intense to make not-negligible the nonlinear behavior of a dielectric. The beginning of the field of nonlinear optics is often taken to be the discovery of second-harmonic generation by Franken et al. [30].

Nonlinear optical phenomena are "nonlinear" in the sense that they occur when the response of a material system to an applied optical field does not depend linearly on the intensity of the optical field. In classical electromagnetic theory, it is shown that the energy H of electromagnetic field within a non-magnetic medium is

$$H = \frac{1}{2\mu_0} \int \mathrm{d}^3 r \, \mathbf{B}^2(\mathbf{r}, t) + \int \mathrm{d}^3 r \int_0^{\mathbf{D}(\mathbf{r},t)} \mathbf{E}(\mathbf{r}, t) \cdot \mathrm{d}\mathbf{D}(\mathbf{r}, t) \tag{2.1}$$

where $\mathbf{D}(\mathbf{r}, t)$ is the electric displacement vector, while $\mathbf{E}(\mathbf{r}, t)$ and $\mathbf{B}(\mathbf{r}, t)$ are respectively the electric and magnetic fields. It is possible to express $\mathbf{D}$ by exploiting the polarization vector $\mathbf{P}$:

$$\mathbf{D}(\mathbf{r}, t) = \varepsilon_0 \mathbf{E}(\mathbf{r}, t) + \mathbf{P}(\mathbf{r}, t) \tag{2.2}$$

where ε_0 is the vacuum dielectric constant. Moreover, one can expand the polarization induced in the medium in a power series in $\mathbf{E}$:

$$P_i = \varepsilon_0 (\chi_{ij}^{(1)} E_j + \chi_{ijk}^{(2)} E_j E_k + \ldots) \tag{2.3}$$

where $\chi^{(n)}$, $(n = 1, 2, ...)$ is a $n+1$ rank tensor representing the n-th order electric susceptibility. This is valid inside a non-dispersive medium or, in general, if the effective frequencies of the field are not too close with respect the resonance frequencies of the medium.

When the susceptibility is strongly frequency-dependent, it is more natural to perform a Fourier decomposition of both P_i and E_i, and to relate the Fourier components $P_i(\omega)$ and $E_i(\omega)$ via a power series. Since each of the $\chi^{(n)}$ involves a different frequency, it is possible to rewrite Eq. 2.3:

$$P_i(\omega_1) = \chi^{(1)}_{ij}(\omega_1;\omega_1)E_j(\omega_1) + \chi^{(2)}_{ijk}(\omega_1;\omega_1-\omega_2,\omega_2)E_j(\omega_1-\omega_2)E_k(\omega_2) + \dots \tag{2.4}$$

By using Eqs. 2.2 and 2.4, Eq. 2.1 becomes:

$$H = \int \left[\frac{1}{2\mu_0}\mathbf{B}^2(\mathbf{r},t) + \frac{1}{2}\varepsilon_0\mathbf{E}^2(\mathbf{r},t) + X_1(\mathbf{r}) + X_2(\mathbf{r}) + \dots\right] \mathrm{d}r \tag{2.5}$$

where

$$X_1((r)) \equiv \frac{1}{2}\int\int \mathrm{d}\omega\mathrm{d}\omega'\, \chi^{(1)}_{ij}(\omega,\omega')E_i(\mathbf{r},\omega')E_j(\mathbf{r},\omega)$$

and

$$X_2((r)) \equiv \frac{1}{3}\int\int\int \mathrm{d}\omega\mathrm{d}\omega'\mathrm{d}\omega''\, \chi^{(2)}_{ijk}(\omega'';\omega-\omega',\omega')E_i(\mathbf{r},\omega'')E_j(\mathbf{r},\omega-\omega')E_k(\mathbf{r},\omega')$$

The canonical quantization of the macroscopic field into a nonlinear medium is a non-trivial problem [31–34]. For this reason, approximations are usually introduced depending on the physical system conditions. A natural choice is trying to replace $\mathbf{E}(\mathbf{r},t)$ and $\mathbf{B}(\mathbf{r},t)$ by the corresponding free-field operators, as long as the nonlinearities are small, provided the resulting Hamiltonian operator is Hermitian. Furthermore, when attention is focused on a particular nonlinear process, it is possible to discard the expansion terms that do not characterize the interaction, e.g. in second harmonic generation and parametric down-conversion, for which only the second-order electric susceptibility is to be taken into account.

2.1.1 Second harmonic generation

Second harmonic generation (SHG) is a process in which a monochromatic light beam of frequency ω_1, incident on a nonlinear medium, generates a new field at the harmonic frequency $\omega_2 = 2\omega_1$. This process is mediated by combinations of creation and annihilation operators ($\hat{a}$ and $\hat{a}^\dagger$). Therefore, it can be described by using the nonlinear terms in Eq. 2.5.

The energy of the two-mode field is expressed in the reduced form as:

$$\hat{H} = \sum_{i=1}^{2}\hbar\omega_i\left(\hat{n}_i + \frac{1}{2}\right) + \hbar g\left[\hat{a}_2^\dagger\hat{a}_1^2 + \hat{a}_1^{\dagger 2}\hat{a}_2\right] \tag{2.6}$$

in which subscrits 1 and 2 correspond to the fundamental and to the second-harmonic modes, respectively, and g is the coupling constant that contains the nonlinear susceptibility $\chi^{(2)}$.

The Hamiltonian in Eq. 2.6 describes a process in which two photons at frequency ω_1 are absorbed in the dielectric and give rise to a new photon at the armonic frequency $\omega_2 = 2\omega_1$, together with the inverse process. It is easy to see from Eq. 2.6, by using the commutation relations among operators $\hat{a}$, $\hat{a}^\dagger$ and $\hat{n}$, that:

$$\left[\hat{n}_1 + 2\hat{n}_2, \hat{H}\right] = 0 \tag{2.7}$$

therefore the sum $\hat{n}_1 + 2\hat{n}_2$ is a constant of motion. Hence, two photons of the fundamental mode are absorbed for every second-harmonic photon emitted.

It is convenient to replace $\hat{a}_1$ and $\hat{a}_2$ with the explicitly time-dependent operators $\hat{\mathcal{A}}_1$ and $\hat{\mathcal{A}}_2$, defined as:

$$\begin{aligned} \hat{\mathcal{A}}_1 &= \hat{a}_1 \exp^{i\omega_1 t} \\ \hat{\mathcal{A}}_2 &= \hat{a}_2 \exp^{i\omega_2 t} \end{aligned} \tag{2.8}$$

which have the same commutation rules as $\hat{a}_1$ and $\hat{a}_2$. Therefore, Heisenberg equations of motion for operators $\hat{\mathcal{A}}_1$ and $\hat{\mathcal{A}}_2$ become:

$$\dot{\hat{\mathcal{A}}}_1 = \frac{1}{i\hbar}\left[\hat{\mathcal{A}}_1, \hat{H}\right] + \frac{\partial \hat{\mathcal{A}}_1}{\partial t} = -2ig\hat{\mathcal{A}}_1^\dagger \hat{\mathcal{A}}_2 \tag{2.9}$$

$$\dot{\hat{\mathcal{A}}}_2 = \frac{1}{i\hbar}\left[\hat{\mathcal{A}}_2, \hat{H}\right] + \frac{\partial \hat{\mathcal{A}}_2}{\partial t} = -ig\hat{\mathcal{A}}_1^2 \tag{2.10}$$

For the Fourier expansion of these operators, it is possible to calculate the second derivatives:

$$\ddot{\hat{\mathcal{A}}}_1 = -2ig\left(\dot{\hat{\mathcal{A}}}_1^\dagger \hat{\mathcal{A}}_2 + \hat{\mathcal{A}}_1^\dagger \dot{\hat{\mathcal{A}}}_2\right) = 4g^2\left(\hat{n}_2 - \frac{\hat{n}_1}{2}\right)\hat{\mathcal{A}}_1 \tag{2.11}$$

$$\ddot{\hat{\mathcal{A}}}_2 = -ig\left(\dot{\hat{\mathcal{A}}}_1 \hat{\mathcal{A}}_1 + \hat{\mathcal{A}}_1 \dot{\hat{\mathcal{A}}}_1\right) = -4g^2\left(\hat{n}_1 + \frac{1}{2}\right)\hat{\mathcal{A}}_2 \tag{2.12}$$

When a plane wave with fixed both frequency and direction propagates through the medium, distance and time are mutually proportional, so they can be used interchangeably. Because the interaction time t effectively corresponds to the propagation time through the medium, provided it is sufficiently short, $\hat{\mathcal{A}}_1$ and $\hat{\mathcal{A}}_2$ can be approximated by a Taylor expansion about $t = 0$. This leads to the equations:

$$\begin{aligned} \hat{\mathcal{A}}_1(t) &= \hat{\mathcal{A}}_1(0) + t\dot{\hat{\mathcal{A}}}_1(t) + \frac{t^2}{2!}\ddot{\hat{\mathcal{A}}}_1(0) + \dots \\ &= \hat{\mathcal{A}}_1(0) - 2igt\hat{\mathcal{A}}_1^\dagger(0)\hat{\mathcal{A}}_2(0) + 2g^2t^2\left[\hat{n}_2 + \frac{1}{2}\hat{n}_1\right]\hat{\mathcal{A}}_1(0) + \dots \end{aligned} \tag{2.13}$$

$$\begin{aligned} \hat{\mathcal{A}}_2(t) &= \hat{\mathcal{A}}_2(0) + t\dot{\hat{\mathcal{A}}}_2(t) + \frac{t^2}{2!}\ddot{\hat{\mathcal{A}}}_2(0) + \dots \\ &= \hat{\mathcal{A}}_2(0) - 2igt\hat{\mathcal{A}}_1^2(0) - 2g^2t^2\left[\hat{n}_1 + \frac{1}{2}\right]\hat{\mathcal{A}}_2(0) + \dots \end{aligned} \tag{2.14}$$

up to terms of order $(gt)^2$. These expansions are valid as long as $\langle\hat{n}_1\rangle(gt)^2 \ll 1$.

Eqs. 2.13 and 2.14 can be exploited both to construct other operators like the photon numbers $\hat{n}_1$ and $\hat{n}_2$, and to calculate their moments. If it is assumed that the state$|\psi\rangle$ of the field at time $t = 0$ is a coherent state with complex amplitude v (that well approximates a laser pump beam) for the first mode and the vacuum for the second mode, then:

$$\begin{aligned} \hat{\mathcal{A}}_1(0)|\psi\rangle &= v|\psi\rangle \\ \hat{\mathcal{A}}_2(0)|\psi\rangle &= 0 \end{aligned} \tag{2.15}$$

and it follows from Eqs. 2.13, that:

$$\langle\hat{n}_1\rangle = \langle\psi|\hat{\mathcal{A}}_1^\dagger(t)\hat{\mathcal{A}}_1(t)|\psi\rangle = |v|^2 - 2(gt)^2|v|^4 + \dots \tag{2.16}$$

$$\langle \hat{n}_2 \rangle = \langle \psi | \hat{\mathcal{A}}_2^\dagger(t) \hat{\mathcal{A}}_2(t) | \psi \rangle = (gt)^2 |v|^4 + \dots \tag{2.17}$$

Therefore, the intensity of the harmonic component grows with the square of both the propagation time and the fundamental harmonic intensity.

With the same approach, it is possible to calculate the fluctuations of the photon numbers and, by exploiting Eqs. 2.13,2.14, it follows that the differences between variance and mean of both modes are given by [35]:

$$\langle (\Delta \hat{n}_1)^2 \rangle - \langle \hat{n}_1 \rangle = -2(gt)^2 |v|^4 + \dots \tag{2.18}$$

$$\langle (\Delta \hat{n}_2)^2 \rangle - \langle \hat{n}_2 \rangle = O\left((gt)^6\right) \tag{2.19}$$

where $O(x)$ denotes the order of magnitude. Therefore, the statistics of the second-harmonic photons are close to Poissonian, but the fundamental mode presents a narrowing of the photon distribution, or sub-Poissonian statistics [16], even if the effect is tiny for small $\langle \hat{n}_2 \rangle$.

2.1.2 Parametric down-conversion

Parametric down-conversion (PDC) is a nonlinear process in which a photon from a strong pump laser is converted into two daughter photons usually called *signal* and *idler*, under momentum and energy conservation. The whole process is summarized in Fig. 2.1. PDC is simple to implement, well understood and it produces well-defined photons in spatio-temporal modes at high rates. For these reasons, PDC is the most widely used technique for generating entangled two-photon states [36] (see section §2.2).

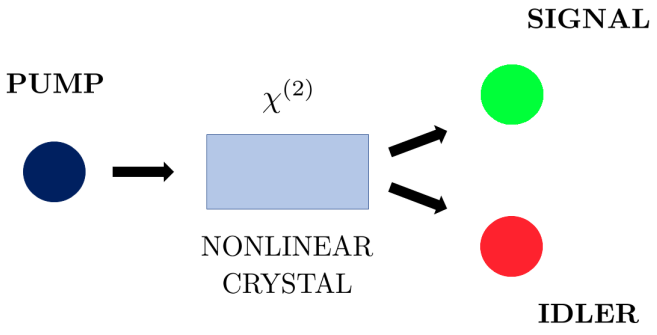

Figure 2.1: Sketch of PDC. A pump field is propagating through a medium exhibiting a $\chi^{(2)}$ nonlinearity. During this interaction, a pump photon generates a pair of daughter photons named *signal* and *idler*.

PDC-generated photon pairs were first observed between the late 1960s and the early 1970s [37–40]. One of the most significant properties of the light, that makes it a very useful tool in several quantum technologies, is that photon pairs generated in this process are naturally entangled. Kwiat *et al.* demonstrated in 1995 the first bright source of highly entangled photons by exploiting PDC [41]. Thanks to this kind of sources, they were increased the studies of the nature of entanglement, such as Bell tests with space-like separated observers [42], entanglement-based quantum cryptography [43], quantum

teleportation [44], multi-particle entanglement [45], *etc.* The development of these applications increased the demands on PDC-based photon sources [36]. In particular, the spreading of these technologies took advantage of an enhancement in the production of bulk and periodically-poled crystals.

PDC can be entirely described only using a quantum mechanical approach, but (just for simplicity) it is possible to start by describing a classical form of a nonlinear parametric process like sum-frequency generation. Many of the relations between the classically interacting fields will also hold for the PDC case.

If an electromagnetic field interacts with a dielectric medium, then it induces a polarization into the material. Usually, the response of the material can be approximated as linear, i.e. the incoming electromagnetic field is not altered in frequency. However, if the electromagnetic field intensity is sufficiently high, then nonlinear properties cannot be neglected anymore. In terms of the electromagnetic field, the polarization P can be expanded as in Eq. 2.3, depending on the electric susceptibility χ. The nonlinearity allows the interaction between electromagnetic waves with different frequencies, and then frequency conversion may occur. In the first nonlinear term ($\chi^{(2)}$), three electromagnetic fields interact in a non-centrosymmetric medium and energy can be transferred from one field to another (three-wave mixing process). To describe the PDC process it is enough to consider this order.

The $\chi^{(2)}$ frequency conversion can roughly be divided into two types. The first one has two input fields and produces a single output field (SHG), the other has a single input field that is converted into two output fields (as previously shown in Fig. 2.1). Historically, for PDC the resulting fields have been named signal and idler, with the former having the higher frequency.

The susceptibility $\chi^{(2)}$ is a rank-3 tensor, and its components are defined through the nonlinear part of the polarization and the electric field components (by exploiting Eq. 2.3):

$$P_i^{(2)} = \varepsilon_0 \sum_{j,k=1}^{3} \chi_{i,j,k}^{(2)} E_j E_k \tag{2.20}$$

with $i = 1, 2, 3$. Usually, the cartesian coordinates x, y, z are assigned to the indices values $1, 2, 3$. Since the fields E_j and E_k can be permuted without changing the polarization, only 18 elements of the $\chi^{(2)}$ tensor are linearly independent. Thus, it is possible to exploit the 3×6 matrix $D_{\chi^{(2)}}$ composed by these 18 elements for reducing the $\chi^{(2)}$ tensor, in order to obtain:

$$\begin{pmatrix} P_x^{(2)} \\ P_y^{(2)} \\ P_z^{(2)} \end{pmatrix} = \varepsilon_0 D_{\chi^{(2)}} \times \begin{pmatrix} E_x^2 \\ E_y^2 \\ E_z^2 \\ 2E_yE_z \\ 2E_xE_z \\ 2E_xE_y \end{pmatrix} \tag{2.21}$$

If the nonlinear interaction couples pump, signal and idler fields with the same polarization, and these fields are coplanar, the process is called type-0 PDC. If signal and idler have the same polarization (orthogonal to the pump one), then the process is labeled type-I PDC, whereas if the two output fields are orthogonally polarized and one of their polarizations is the same as the pump one it is called type-II PDC.

It is possible to add the nonlinear part of the polarization to the (macroscopic) Maxwell equations, in order to derive the electric fields. Assuming collinear propagation of the waves

along the x-direction, it follows the wave equation:

$$\frac{\partial^2 E}{\partial x^2} = -\mu_0 \left(\varepsilon_0 \frac{\partial^2 E}{\partial t^2} + \frac{\partial^2 P^{(2)}}{\partial t^2} \right) \tag{2.22}$$

In the case of sum-frequency generation, let us assume two incident monochromatic plane waves in the form of

$$E_j = A_j(x) e^{i(\omega_j t - k_j x)} \tag{2.23}$$

with $j = 1, 2$, frequencies ω_1 and ω_2, propagation constants k_1 and k_2, and a possible varying amplitude $A_j(x)$ along the propagation direction. This will induce a periodic modulation of the polarization at frequency:

$$\omega_3 = \omega_1 + \omega_2 \tag{2.24}$$

generating a new field E_3 at frequency ω_3. The expression for the new field can be derived from Eq. 2.22 by replacing $P^{(2)}$ with the input fields E_1 and E_2 coupled to $\chi^{(2)}$. The E_3 amplitude along propagation direction is then:

$$\frac{\mathrm{d}A_3}{\mathrm{d}x} = -\frac{i\omega_3}{2n_3 c} d_{jl} A_1 A_2 e^{i\Delta k x} \tag{2.25}$$

using the slowly varying amplitude approximation $\left(\frac{\mathrm{d}^2 E}{\mathrm{dx}^2} \ll k \frac{\mathrm{d}E}{\mathrm{d}x} \right)$, where n_3 is the refractive index associated with the E_3 propagating field. Similar expressions can be obtained for E_1 and E_2. The nonlinear coefficient d_{jl} is derived from the proper matrix $D_{\chi^{(2)}}$ element in Eq. 2.21, depending on the polarization of the fields. The wave-vector mismatch Δk is given by:

$$\Delta k = k_3 - k_1 - k_2 = \frac{n_3 \omega_3}{c} - \frac{n_1 \omega_1}{c} - \frac{n_2 \omega_2}{c} \tag{2.26}$$

By integrating Eq. 2.25, the amplitude of the generated field after a propagation distance L results:

$$A_3(L) = -\frac{d_{jl} \omega_3 A_1 A_2}{2n_3 c} \left(\frac{e^{i\Delta k L} - 1}{\Delta k} \right) \tag{2.27}$$

were the fields E_1 and E_2 are assumed constant throughout the interaction (the so-called undepleted-pump approximation). The intensity of E_3 after a length L is obtained by exploiting the relation $I_k = \frac{1}{2} n_k \varepsilon_0 c E_k E_k^*$, with $k = 1, 2, 3$. The result is:

$$I_3(L) = \frac{d_{jl}^2 \omega_3^2 I_1 I_2 L^2}{2n_1 n_2 n_3 c^3 \varepsilon_0} \mathrm{sinc}^2 \left(\frac{\Delta k L}{2} \right) \tag{2.28}$$

Therefore, the efficiency of the conversion process strongly depends on Δk. If $\Delta k \neq 0$, then the generated field becomes out of phase by π after an interaction length of

$$L_c = \frac{\pi}{\Delta k} \tag{2.29}$$

which is also called the coherence length. In this case, the generated field starts to interfere destructively, until the conversion efficiency reaches zero at length $L = 2L_c$. Hence, to obtain an optimal frequency conversion, the phase-matching condition must be $\Delta k = 0$, so generalizing in three dimensions [36]:

$$\mathbf{k}_3 = \mathbf{k}_1 + \mathbf{k}_2 \tag{2.30}$$

This derivation only regards interactions where at least two fields are present, as in sum-frequency generation. However, in a PDC interaction just one pump field is present, and a purely classical treatment cannot explain the generation of two daughter fields. To describe properly this phenomenon, a second-quantization formalism is needed.

As shown in Eq. 2.1, the classical Hamiltonian of an electric field can be written as:

$$H_{\mathrm{EM}} \propto \int \mathrm{d}r^3\, \mathbf{E}(\mathbf{r},t)\cdot\mathbf{D}(\mathbf{r},t) \tag{2.31}$$

By focusing only on the second order term, in the displacement vector $\mathbf{D}$ yields the interaction Hamiltonian for the $\chi^{(2)}$ process

$$H_{\chi^{(2)}} \propto \int \mathrm{d}r^3\, \chi^{(2)}\mathbf{E}_p(\mathbf{r},t)\mathbf{E}_s(\mathbf{r},t)\mathbf{E}_i(\mathbf{r},t) \tag{2.32}$$

where p, s, i stand for pump, signal and idler respectively.

In second quantization, Eq. 2.32 becomes:

$$\hat{H}_{\mathrm{PDC}} \propto \chi^{(2)} \int_{-\frac{L}{2}}^{\frac{L}{2}} \mathrm{d}z\, \hat{E}_p^{(+)}\hat{E}_s^{(-)}\hat{E}_i^{(-)} + h.c. \tag{2.33}$$

where the z-axis is the pump field propagation direction inside a crystal of length L, neglecting the transverse degrees of freedom. The positive and negative frequency parts of the quantum fields in Eq. 2.33 are defined as follows:

$$\hat{E}_{\mathrm{x}}^{(+)} = \hat{E}_{\mathrm{x}}^{(-)\dagger} = A \int \mathrm{d}\omega_{\mathrm{x}}\, e^{i(k_{\mathrm{x}}z-\omega_{\mathrm{x}}t)}\hat{a}_{\mathrm{x}}(\omega_{\mathrm{x}}) \tag{2.34}$$

where $\mathrm{x} = p, s, i$, all constant factors have been merged into the overall constant A, and $\hat{a}_{\mathrm{x}}(\omega_{\mathrm{x}})$ is the photon annihilation operator for a monochromatic frequency ω_{x} with wave vector component along the z axis k_{x}. The PDC process type (0, I or II) depends on both the applied pump field and the $\chi^{(2)}$-nonlinearity of the crystal. Since the incoming pump field must be relatively strong because of the weakness of the nonlinear interaction, it can be treated as a classical field:

$$E_p^{(+)} = E_p^{(-)*} = \int \mathrm{d}\omega_p\, \alpha(\omega_p) e^{i(k_p(\omega_p)z-\omega_p t)} \tag{2.35}$$

where $\alpha(\omega_p)$ describes the spectrum and the amplitude of the pump field: it can vary from a delta function $E_p\delta(\omega_p-\omega_c)$ for continuous-wave laser sources with central frequency ω_c, to more complex distributions.

In Schrödinger picture, the state generated in the PDC process can be described as in [46]:

$$|\psi\rangle_{\mathrm{PDC}} = \exp\left[-\frac{i}{\hbar}\int_{t_0}^{t}\mathrm{d}t'\,\hat{H}_{\mathrm{PDC}}(t')\right]|0\rangle \tag{2.36}$$

With a perturbation expansion, the PDC output state becomes:

$$|\psi\rangle_{\mathrm{PDC}}^{\mathrm{full}} = |0\rangle - \frac{i}{\hbar}\int_{t_0}^{t}\mathrm{d}t'\,\hat{H}_{\mathrm{PDC}}(t')|0\rangle + \left(\frac{i}{\hbar}\right)^2\int_{t_0}^{t}\mathrm{d}t'\,\hat{H}_{\mathrm{PDC}}(t')\int_{t_0}^{t'}\mathrm{d}t''\,\hat{H}_{\mathrm{PDC}}(t'')|0\rangle + \cdots \tag{2.37}$$

where the zero-order term describes the vacuum, the first-order term the photon-pair emission, the second-order term the double pair emission, and so on. When the pump field

is not too intense and the probability of multi-pair generation is negligible [47, 48], it is possible to truncate the expansion up to the first order:

$$|\psi\rangle_{\mathrm{PDC}} \cong |0\rangle - \frac{i}{\hbar}\int_{t_0}^{t} \mathrm{d}t'\, \hat{H}_{\mathrm{PDC}}(t')|0\rangle \tag{2.38}$$

which describes the non-normalized two-photon PDC state emitted.

Exploiting Eqs. 2.33 2.34, 2.35, and 2.38, it follows [36]:

$$\begin{aligned}\int_{t_0}^{t} \mathrm{d}t'\, \hat{H}_{\mathrm{PDC}}(t') = B\int_{t_0}^{t}\mathrm{d}t' \int_{-\frac{L}{2}}^{\frac{L}{2}}\mathrm{d}z \int\int\int \mathrm{d}\omega_p \mathrm{d}\omega_s \mathrm{d}\omega_i\, \alpha(\omega_p) e^{-i(\omega_p-\omega_s-\omega_i)t'} \\ \times\ e^{i[k_p(\omega_p)-k_s(\omega_s)-k_i(\omega_i)]z}\hat{a}_s^\dagger \hat{a}_i^\dagger + h.c.\end{aligned} \tag{2.39}$$

where all the constants are merged into the B term. By integrating along the z direction, Eq. 2.39 becomes:

$$\begin{aligned}\int_{t_0}^{t} \mathrm{d}t'\, \hat{H}_{\mathrm{PDC}}(t') = B\int_{t_0}^{t}\mathrm{d}t' \int\int\int \mathrm{d}\omega_p \mathrm{d}\omega_s \mathrm{d}\omega_i\, \alpha(\omega_p) e^{-i(\omega_p-\omega_s-\omega_i)t'} \\ \times\ L\,\mathrm{sinc}\left[\frac{L}{2}\left(k_p(\omega_p)-k_s(\omega_s)-k_i(\omega_i)\right)\right]\hat{a}_s^\dagger \hat{a}_i^\dagger + h.c.\end{aligned} \tag{2.40}$$

The integration over the range $\left[-\frac{L}{2}, \frac{L}{2}\right]$ assumes a pump with no extra phase factors in the center of the crystal (a pump pulse with no additional phase factor at the beginning of the interaction leads to an additional phase factor in the final result).

Concerning the integration over the time variable, the range can be expanded to plus and minus infinity if one is interested in the state long before and after the interaction inside the crystal. Then, the integration of the time-dependent part results in a delta function $2\pi\delta(\omega_p - \omega_s - \omega_i)$. This allows to take the integral over the pump frequencies ω_p:

$$\begin{aligned}\int_{-\infty}^{+\infty} \mathrm{d}t\, \hat{H}_{\mathrm{PDC}}(t) = 2\pi B\int\int \mathrm{d}\omega_s \mathrm{d}\omega_i\, \alpha(\omega_s+\omega_i) \\ \times\ L\,\mathrm{sinc}\left[\frac{L}{2}\left(k_p(\omega_s+\omega_i)-k_s(\omega_s)-k_i(\omega_i)\right)\right]\hat{a}_s^\dagger \hat{a}_i^\dagger + h.c.\end{aligned} \tag{2.41}$$

With the last equation, it is now possible to write the formula of the generated PDC state:

$$\begin{aligned}|\psi\rangle_{\mathrm{PDC}} &= |0\rangle + B'\int\int \mathrm{d}\omega_s \mathrm{d}\omega_i\, \alpha(\omega_s+\omega_i)\mathrm{sinc}\left[\frac{L}{2}\Delta k(\omega_s,\omega_i)\right]\hat{a}_s^\dagger \hat{a}_i^\dagger|0\rangle \\ &= |0\rangle + B'\int\int \mathrm{d}\omega_s \mathrm{d}\omega_i\, \alpha(\omega_s+\omega_i)\Phi(\omega_s,\omega_i)\hat{a}_s^\dagger \hat{a}_i^\dagger|0\rangle \\ &= |0\rangle + B'\int\int \mathrm{d}\omega_s \mathrm{d}\omega_i\, f(\omega_s,\omega_i)\hat{a}_s^\dagger \hat{a}_i^\dagger|0\rangle\end{aligned} \tag{2.42}$$

where $\Delta k(\omega_s, \omega_i) = k_p(\omega_s+\omega_i) - k_s(\omega_s) - k_i(\omega_i)$, and the constant factor $B' \propto E_p L$ linearly depends on the crystal lenght L and the amplitude of the pump field (Eq. 2.35).

As described before, PDC generates two-photon states with a given joint-spectral amplitude (JSA) $f(\omega_s, \omega_i)$. The exact shape of the JSA is defined both by the form of the pump distribution $\alpha(\omega_s, \omega_i)$, and the phase-matching function $\Phi(\omega_s, \omega_i)$ determined by the length and the dispersion of the crystal. In Eq. 2.42 we can recover the conservation

of energy and momentum disclosed in Eqs. 2.24, 2.30, because all the signal-idler pairs generated satisfy the so-called phase-matching conditions:

$$\begin{cases} \omega_p = \omega_s + \omega_i \\ \mathbf{k}_p = \mathbf{k}_s + \mathbf{k}_i \end{cases} \tag{2.43}$$

The phase-matching conditions in Eq. 2.43 represent the ideal case of infinite crystals ($L \to +\infty$). For finite crystals, Eq. 2.40 gives a solution $\propto \text{sinc}\left[\frac{L}{2}\left(k_p(\omega_p) - k_s(\omega_s) - k_i(\omega_i)\right)\right]$, implying that signal and idler are emitted within slight bands of momenta $\mathbf{k}$. Typically, this contribution is negligible, because one has to consider the finite frequency bandwidth in the experimental configuration.

and this effect can be neglected experimentally because of the mandatory filtering performed by the photon detection.

The phase-matching conditions are subject to dispersion in the nonlinear medium, through $k = \omega n(\omega)/c$ (see also Eq.2.26). In order to satisfy the condition over the wave vectors, polarizations and the same wave vectors of the interacting field have to be selected such that $\omega_p n_p(\omega_p) = \omega_s n_s(\omega_s) + \omega_i n_i(\omega_i)$. However, inside an isotropic bulk crystal, the normal dispersion ensures that this is not possible while also fulfilling the condition over the frequencies. For this reason, anisotropic materials are used, in which fields with different polarizations undergo different refractive indices. The plane containing the optical axis and the pump wave vector is called the principal plane, and a light beam polarized orthogonally to that plane is denoted as *ordinary (o)* while a beam whose polarization lies within that plane is dubbed *extraordinary (e)*.

In these materials, phase-matching can be achieved for orthogonally polarized fields through birefringent phase-matching, which is most commonly done by tuning the angle between the crystal axes and the interacting fields. This method is also known as "critical phase-matching", because it is quite sensitive to deviations from optimal conditions, then it limits the angular, spectral, and temperature acceptance bandwidth. Otherwise, angle θ between the field vector and the optical axis of the crystal can be set to 90°, and the phase matching occurs by varying the temperature of the crystal. This technique is defined *non-critical* phase-matching.

Angular phase matching is schematically shown in Fig. 2.2.a [36]. In Fig. 2.2.b [36] two phase-matching possibilities are shown: type-I down-conversion of a pump beam orthogonally polarized to the two co-polarized down-conversion fields, and type-II down-conversion, where the down-converted fields are orthogonally polarized and one of them has the same polarization as the pump photon.

In general, the type-0 phase-matching option, where all fields are co-polarized, cannot be implemented in bulk materials, but is often exploited with periodically-poled crystals in the case of collinear or quasi-collinear PDC configuration.

Inside periodically-poled crystals, the nonlinear properties are spatially modulated along the propagation direction. The dissertation of this kind of crystals is beyond this thesis, but the reader can see the concept of quasi-phase-matching conditions needed for PDC in periodically-poled crystals in Ref. [49].

2.2 PDC-based sources

As quantum optics applications evolved, they placed increasing demands on photon sources. The biggest improvement to both pair creation rate and flexibility was due to rapid advances in nonlinear optics, specifically, the development of periodically-poled crystals.

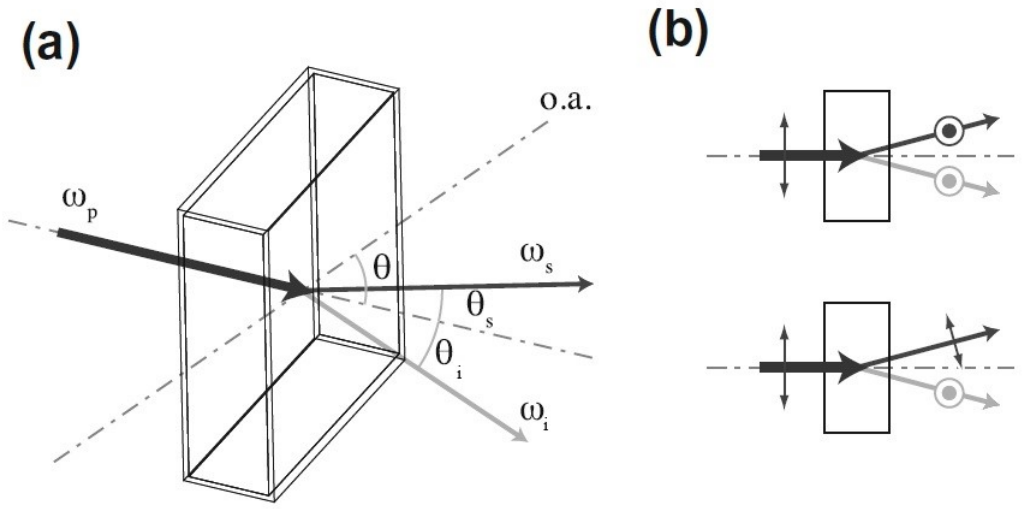

Figure 2.2: Parametric down-conversion in a bulk crystal. (a) Angular phase matching. The optical crystal axis (o.a.) spans an angle θ with the pump field. The down-converted fields emerge at angles θ_s and θ_i. (b) PDC in birefringent materials can be achieved via type-I (top) or type-II (bottom) phase matching.

PDC is largely exploited for both single photons and entangled photon pairs production, because it is a well-known and simple-manageable process.

2.2.1 Heralded single-photon sources

If the two photons generated by PDC can be efficiently and deterministically separated, for example distinguishing them by their polarizations or their wavelengths, then the detection of one photon heralds the presence of a correlated photon, i.e. the one belonging to the same pair. Thus, by detecting the idler photon one has a trigger for the presence of the signal photon from the PDC state in Eq. 2.42. In presence of a single photon, a detector with detection efficiency η can be modeled by a "click" detection operator $\hat{\pi}_1$ and a "no-click" non-detection operator $\hat{\pi}_0$:

$$\begin{aligned} \hat{\pi}_0 &= \int \mathrm{d}\omega \, |0,\omega\rangle\langle 0,\omega| \\ \hat{\pi}_1 &= \int \mathrm{d}\omega \, \eta |1,\omega\rangle\langle 1,\omega| \end{aligned} \tag{2.44}$$

where $|0,\omega\rangle$ implies vacuum at frequency ω and $|1,\omega\rangle$ a single photon at the same frequency. Since this dissertation concerns single photons detections, higher-photon-number components in $\hat{\pi}_0$ and $\hat{\pi}_1$ are omitted. Most of the commonly used detectors are also called binary, because they are not able to resolve the number of photons arriving simultaneously.

The probability of detecting the trigger photon and successfully heralding a single-photon state depends on both the efficiency η of the detector and the spectral amplitude of the two-photon state generated in the PDC process. Obviously, employing efficient detectors is the simplest method for increasing the heralding efficiency. Furthermore, it is also possible to increase the pump intensity, in order to boost the amplitude of the two-photon component in the PDC state. However, at some point the perturbation expansion of Eq. 2.38 breaks down, and higher-order terms have to be considered to correctly model the process.

Thus, the *non-normalized* heralded single-photon state after a successful detection event (Eqs. 2.42, 2.44) is:

$$\begin{aligned}\rho_s &= \mathrm{Tr}\left[\hat{\pi}_1|\psi\rangle\langle\psi|\right] \\ &= \int \mathrm{d}\omega_t'' \,\langle\omega_t''|\left[\eta^2 \int\int \mathrm{d}\omega_s \mathrm{d}\omega_t \, f(\omega_s,\omega_t) \int\int \mathrm{d}\omega_s' \mathrm{d}\omega_t' \, f^*(\omega_s',\omega_t')|\omega_s,\omega_t\rangle\langle\omega_s',\omega_t'|\right]|\omega_t''\rangle \\ &= \eta^2 \int\int \mathrm{d}\omega_s \mathrm{d}\omega_s' \left[\int \mathrm{d}\omega_t'' \, f(\omega_s,\omega_t'') f^*(\omega_s',\omega_t'')\right]|\omega_s\rangle\langle\omega_s'| \\ &= \eta^2 \int\int \mathrm{d}\omega_s \mathrm{d}\omega_s' j(\omega_s,\omega_s')|\omega_s\rangle\langle\omega_s'|\end{aligned} \tag{2.45}$$

In the last equation, the heralded single-photon state is described with the density matrix entries $j(\omega_s,\omega_s')$, determined by the joint spectral amplitude $f(\omega_s,\omega_t)$ of the PDC state. The $j(\omega_s,\omega_s')$ density matrix already provides information concerning the purity of the state: if it is separable, then it can be written as $j(\omega_s,\omega_s') = f(\omega_s)f^*(\omega_s')$, and the photon is heralded in a pure state. In this case Eq. 2.45 becomes:

$$\begin{aligned}\rho_s &= \eta^2 \int\int \mathrm{d}\omega_s \mathrm{d}\omega_s' \, f(\omega_s) f^*(\omega_s')|\omega_s\rangle\langle\omega_s'| \\ &= \eta^2 \int \mathrm{d}\omega_s \, f(\omega_s)|\omega_s\rangle \int \mathrm{d}\omega_s' \, f^*(\omega_s')\langle\omega_s'| = |\psi_s\rangle\langle\psi_s|\end{aligned} \tag{2.46}$$

because pure states always correspond to circular-shaped $j(\omega_s,\omega_s')$ [50, 51].

To obtain further insight into the PDC process, one can exploit the Schmidt decomposition theorem [5]. It states that every well-behaved *normalized* two-dimensional function could be decomposed as a sum over a range of possible values m_k and complete sets of orthonormal functions $g_k(x)$ and $h_k(y)$:

$$f(x,y) = \sum_k m_k g_k(x) h_k(y)\,, \quad \sum_k m_k^2 = 1 \tag{2.47}$$

By exploiting this decomposition, the PDC state (Eq. 2.42) becomes:

$$|\psi\rangle_{\mathrm{PDC}} = |0\rangle + b \int\int \mathrm{d}\omega_s \mathrm{d}\omega_t \sum_k m_k g_k(\omega_s) h_k(\omega_t) \hat{a}_s^\dagger(\omega_s) \hat{a}_t^\dagger(\omega_t)|0\rangle \tag{2.48}$$

where b is a constant for normalizing $B' f(\omega_s,\omega_t)$, with B' defined in Eq. 2.42. If it is performed a basis transformation from the single-frequency modes $\hat{a}_s^\dagger(\omega_s)$ and $\hat{a}_t^\dagger(\omega_t)$ to the broadband frequency modes $\hat{A}_k^\dagger$ and $\hat{B}_k^\dagger$, defined as:

$$\begin{aligned}\hat{A}_k^\dagger &= \int \mathrm{d}\omega_s g_k(\omega_s) \hat{a}_s^\dagger(\omega_s) \\ \hat{B}_k^\dagger &= \int \mathrm{d}\omega_t h_k(\omega_t) \hat{a}_t^\dagger(\omega_t)\end{aligned} \tag{2.49}$$

then, the PDC behaves as a sum over the broadband modes $\hat{A}_k^\dagger$ and $\hat{B}_k^\dagger$

$$|\psi\rangle_{\mathrm{PDC}} = |0\rangle + b \sum_k m_k \hat{A}_k^\dagger \hat{B}_k^\dagger |0\rangle \tag{2.50}$$

Therefore, the photon pair generated from the PDC with a given frequency distribution $f(\omega_s,\omega_t)$ is emitted into a superposition of strictly-correlated broadband frequency modes

$\hat{A}_k^\dagger$ and $\hat{B}_k^\dagger$: if the signal one is detected in the $\hat{B}_k^\dagger$ mode, then the heralding one is present in mode $\hat{A}_k^\dagger$, and vice versa.

It is possible to expand also the detection observables $\hat{\pi}_0$ and $\hat{\pi}_1$ (Eq. 2.44) in the broadband basis of the trigger modes:

$$\begin{aligned} \hat{\pi}_0 &= \sum_k |0, h_k(\omega_t)\rangle\langle 0, h_k(\omega_t)| \\ \hat{\pi}_1 &= \eta \sum_k |1, h_k(\omega_t)\rangle\langle 1, h_k(\omega_t)| \end{aligned} \tag{2.51}$$

With the last two equations, the density operator of the heralded single photon can be written as:

$$\rho_s = \sum_k m_k^2 |1, g_k(\omega_s)\rangle\langle 1, g_k(\omega_s)| \tag{2.52}$$

Hence, after the detection process, the signal photon is projected into a statistical mixture of broadband single-photon states with probabilities m_k. The amount of possible m_k and their respective amplitudes depend on the joint spectrum of the initial PDC state.

This behavior is due to the single-photon detector, because it can not discriminate optical modes. In principle, it is impossible to know which optical mode was responsible for triggering the detection event. Therefore, the heralded signal photon is emitted into a statistical mixture of broadband modes. There are different measurement standards to characterize the purity of the heralded signal photons [36], e.g. the cooperativity [52] $K = 1/(\sum_k m_k^4)$, which is equal to one if the signal photon is in a pure state and it increases with the amount of mixedness, or the von Neumann entropy [53] $S = -\sum_k m_k^2 \log_2 m_k^2$, which ranges from zero for pure states to infinity for rising degrees of impurity.

2.2.2 Two-photon entangled states sources

The generation of entangled bipartite states is crucial for studying quantum foundations. PDC allows producing polarization-entangled photon pairs by conveniently selecting the phase-matching conditions. By using bulk PDC crystals, there are two most common ways for creating entanglement between corresponding signal and idler photons. In Fig. 2.3 these two possibilities are shown. The first one (Fig. 2.3.a) is to exploit two identical type-I PDC crystals, with corresponding optical axes orthogonally placed. Signal and idler have the same polarization, thus they are spatially distributed belong two concentric cones, with the surfaces that depend on the frequency of the photons. If the thickness of the crystals is small enough, it is impossible to know in which one signal and idler were generated and the relative amplitudes add coherently. Thus, by selecting signal and idler photons with frequency $\omega_s = \omega_i = \omega_p/2$, this method produces entangled photon pairs with polarization state $|\psi\rangle_{\text{PDC-I}} = (|HH\rangle + e^{i\phi}|VV\rangle)/2$.

The second one (Fig. 2.3.b) consists of using a type-II PDC crystal. Since signal and idler are orthogonally polarized, they are spatially distributed in two non-concentric cones, because of the different refractive index they undergo inside the crystal. As in the previous case, the surfaces of the cones depend on the frequency of their photons. By considering again just signal and idler with frequency $\omega_s = \omega_i = \omega_p/2$, the photon pairs that belong to the intersections of the cones are entangled in polarization, and their state is $|\psi\rangle_{\text{PDC-II}} = (|HV\rangle + e^{i\phi}|VH\rangle)/2$.

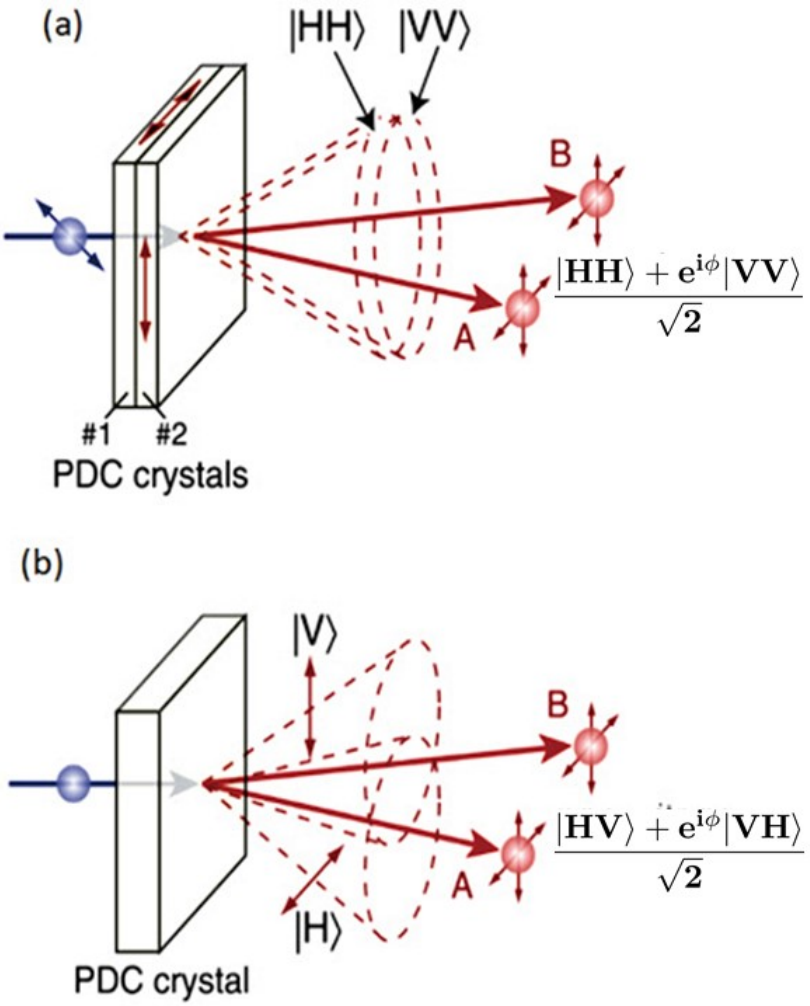

Figure 2.3: Sketches of entangled photon pairs production with PDC. a) The pump photon passes through two type-I PDC crystals with orthogonal optical axes. Thus, if the crystals are thin enough, it is impossible to know in which crystal signal and idler were generated. If they have the same frequency (equal to the half of the pump frequency), they are in an entangled polarization state. b) The pump photon passes throug a type-II PDC crystal. Since signal and idler are orthogonally polarized, they are spatially distributed in two different cones, because of the different refractive index they undergo. The photon pairs that belong to the intersections of the two cones are in an entangled polarization state.

Chapter 3

Optimal estimation of entanglement and discord in bipartite states

3.1 Quantum correlation parameters and their estimation

The presence of quantum correlations in a multi-partite state plays a crucial role in quantum information as well as in other quantum technologies, e.g. quantum metrology and sensing [5, 17, 54]. Therefore, characterization and quantification of quantum correlations represent a crucial task for the development of these new technologies. Undoubtedly, the best known example of quantum correlations is entanglement [5], but there are other kind of non-classical correlations, e.g. quantum discord [55, 56]. In this section, I am going to describe an experiment about entanglement and discord estimation in bipartite states, performed by exploiting polarization-entangled photon pairs [57].

In QM, a state can be completely described by its density matrix operator [5, 54]. Each property of the state, including correlations, are described by the density matrix. Experimentally, this operator can be reconstructed by performing a quantum state tomography [58,59], but such a procedure requires a big amount of measurements (especially for multi-partite states), and it is very expensive computationally.

Alternatively, it is possible to find parameters suited to quantify entanglement and discord in particular families of multi-partite states, and efficiently implement estimation algorithms for such parameters of interest. The aim of this work is to experimentally demonstrate a technique for the estimation of quantum parameters quantifying the amount of non-classical correlations within bipartite states, with the smallest uncertainty available. This result can be achieved if one has some *a priori* knowledge regarding the state under exam.

In particular, we realized a source able to prepare two-photon polarization states described by the following density matrix:

$$\rho^{th} = p \begin{pmatrix} 0 & 0 & 0 & 0 \\ 0 & \frac{1}{2} & -\frac{1}{2} & 0 \\ 0 & -\frac{1}{2} & \frac{1}{2} & 0 \\ 0 & 0 & 0 & 0 \end{pmatrix} + (1-p) \begin{pmatrix} 0 & 0 & 0 & 0 \\ 0 & \frac{1}{2} & 0 & 0 \\ 0 & 0 & \frac{1}{2} & 0 \\ 0 & 0 & 0 & 0 \end{pmatrix} \quad , \quad p \in [0,1] \tag{3.1}$$

that is a mixture between the pure, maximally-entangled state $|\psi_-\rangle = (|HV\rangle - |VH\rangle)/\sqrt{2}$ and a completely decoherent state $\rho_{mix} = (|HV\rangle\langle HV| + |VH\rangle\langle VH|)/2$, where H and V are respectively the horizontal and vertical polarization components, and $|XY\rangle = |X\rangle_A \otimes |Y\rangle_B$.

In order to estimate the amount of entanglement, we considered three different parameters: Negativity [53, 60], Concurrence [61], Log-Negativity [53]; whereas for the discord

we considered Quantum Geometric Discord [62].

Bennett *et al.* [63] demonstrated that it is possible to quantify the amount of entanglement inside a bipartite quantum system in terms of the von Neumann entropy [5] calculated with respect to one of the two subsystems. If $|\psi\rangle$ is a pure two-photon state and $\rho^{AB} = |\psi\rangle\langle\psi|$ is its corresponding density operator, the amount of entanglement inside $|\psi\rangle$ is:

$$E(\psi) = -\mathrm{Tr}\left[\rho^A \log_2 \rho^A\right] \tag{3.2}$$

where $\rho^A = \mathrm{Tr}_B\left[\rho^{AB}\right]$ is the partial trace of the global density operator ρ^{AB} with respect to the subsystem B. From Eq. 3.2 it is clear that if $|\psi\rangle$ is a separable state, then $E(\psi)$ would be null.

In general, a measure of the entanglement $E(\rho)$ must have the following properties:

- $E(\rho) = 0$ for separable states;
- $E(\rho)$ is maximum for maximally-entangled states;
- $E(\rho)$ is a continuous function;
- $E(\rho)$ is a convex function, i.e. $E(\lambda\rho + (1-\lambda)\rho') \leq \lambda E(\rho) + (1-\lambda)E(\rho')$, $\forall\lambda \in [0,1]$.

Von Neumann entropy can be exploited for measuring entanglement inside pure states only, while for mixtures other approaches have to be introduced. Several theoretical and experimental works have addressed this topic [64–67], providing different strategies to efficiently estimate the amount of entanglement of a quantum state from a reduced set of measurements [68–72], e.g. visibility measurements [73], Bell tests [24], entanglement witnesses [74–78], Schmidt number [79–81]. Many of these techniques have also been implemented in laboratory [82–90].

As mentioned before, we chose three parameters for entanglement and one for quantum discord. For each parameter, we implemented two estimators: one optimal and the other non-optimal (an estimator is optimal if it allows achieving the minimum uncertainty possible).

If we consider a quantum observable $\mathcal{O}$, described by the parameter λ, the theoretical limit of the uncertainty σ_λ is fixed by the quantum Cramér-Rao bound:

$$Var(\lambda) \geq \frac{1}{MH(\lambda)} \tag{3.3}$$

where $Var(\lambda)$ is the variance related to the parameter λ, M is the number of realized measurements and $H(\lambda)$ is the quantum Fisher information [91]. The Fisher information is a parameter connected to the entropy of the system under exam, and it is already present in classical information theory together with the Cramér-Rao bound, although they have to be generalized to the quantum case.

If one classically measure the estimation parameter λ and the obtained outcome is x, the Fisher information is defined as:

$$F(\lambda) = \int dx\, p(x|\lambda) \left(\frac{\partial \ln p(x|\lambda)}{\partial\lambda}\right)^2 = \int dx\, \frac{1}{p(x|\lambda)} \left(\frac{\partial p(x|\lambda)}{\partial\lambda}\right)^2 \tag{3.4}$$

Therefore, the classical counterpart of Eq. 3.3 is:

$$Var(\lambda) \geq \frac{1}{MF(\lambda)} \tag{3.5}$$

In order to rewrite Eq. 3.4 in terms of quantum operators, the system has to be described as a function of the parameter λ by exploiting the density operator ρ_λ. The estimator O_λ is a self-adjoint operator, defined in the same Hilbert space associated with ρ_λ, and it describes a quantum measurement with possible outcomes x.

By using an indirect procedure as an estimation algorithm, it is introduced a greater uncertainty over the parameter under exam with respect a direct measurement. Thus, the aim of quantum estimation theory is to minimize this induced uncertainty.

In QM, by measuring over a complete set of positive operator-valued measures (POVMs) [5] $\{\Pi_x\}$, $\int dx\, \Pi_x = \mathbb{1}$, one can express the probability in Eq. 3.4 as $p(x|\lambda) = \mathrm{Tr}\left[\Pi_x \rho_\lambda\right]$, according to the Born's rule [27]. By introducing the Symmetric Logarithmic Derivative (SLD) L_λ as the self-adjoint operator satisfying the following equation:

$$\frac{L_\lambda \rho_\lambda + \rho_\lambda L_\lambda}{2} = \frac{\partial \rho_\lambda}{\partial \lambda} \tag{3.6}$$

it is obtained that $\partial_\lambda p(x|\lambda) = \mathrm{Tr}\left[\partial_\lambda \rho_\lambda \Pi_x\right] = \mathrm{Re}(\mathrm{Tr}\left[\rho_\lambda \Pi_x L_\lambda\right])$. Thus, Eq. 3.4 can be rewritten as:

$$F(\lambda) = \int dx\, \frac{\mathrm{Re}(\mathrm{Tr}\left[\rho_\lambda \Pi_x L_\lambda\right])^2}{\mathrm{Tr}\left[\rho_\lambda \Pi_x\right]} \tag{3.7}$$

For a classical measurement, the lower limit of the related uncertainty can be predicted by using Eqs. 3.4 and 3.5. It is possible to extend this limit to the QM framework by maximizing the Fisher information referred to a quantum measurement set by increasing the real part inside the integral in Eq. 3.7:

$$\begin{aligned} F(\lambda) &\leq \int dx \left| \frac{\mathrm{Tr}\left[\rho_\lambda \Pi_x L_\lambda\right]}{\sqrt{\mathrm{Tr}\left[\rho_\lambda \Pi_x\right]}} \right|^2 \\ &= \int dx \left| \mathrm{Tr}\left[\frac{\sqrt{\rho_\lambda}\sqrt{\Pi_x}}{\sqrt{\mathrm{Tr}\left[\rho_\lambda \Pi_x\right]}} \sqrt{\Pi_x} L_\lambda \sqrt{\rho_\lambda} \right] \right|^2 \\ &\leq \int dx\, \mathrm{Tr}\left[\Pi_x L_\lambda \rho_\lambda L_\lambda\right] \\ &= \mathrm{Tr}\left[L_\lambda \rho_\lambda L_\lambda\right] = \mathrm{Tr}\left[\rho_\lambda L_\lambda^2\right] \end{aligned} \tag{3.8}$$

Thanks to this chain of inequalities it is demonstrated that the Fisher information is always equal or smaller than a quantity $H(\lambda)$ called quantum Fisher information (QFI):

$$F(\lambda) \leq \mathrm{Tr}\left[\rho_\lambda L_\lambda^2\right] = \mathrm{Tr}\left[\partial_\lambda \rho_\lambda L_\lambda\right] \equiv H(\lambda) \tag{3.9}$$

from which Eq. 3.3 is obtained.

In the following sections, we introduce the entanglement and discord parameters examined during our experiment [57].

Negativity

Negativity is a parameter introduced for estimating the amount of entanglement inside a bipartite quantum system. It exploits the Peres' criterion [92], which states that any separable state must have the partial-transpose density matrix with non-negative eigenvalues. Negativity is defined by:

$$\mathcal{N}(\rho) \equiv \|\rho^{T_A}\| - 1 \tag{3.10}$$

where ρ^{T_A} is the partial transpose (with respect the A subsystem) of the density operator, while $\|X\| = \mathrm{Tr}\left[\sqrt{X^T X}\right]$ is the *trace norm* of the X matrix.

Being $\{|i_A\rangle\}$ and $\{|i_B\rangle\}$ two orthonormal and complete bases respectively for the $\mathcal{H}_A$ and $\mathcal{H}_B$ subspaces, an orthonormal and complete basis for the Hilbert space where the bipartite-state density operator is given by the tensorial product between vectors of $\{|i_A\rangle\}$ and $\{|i_B\rangle\}$, i.e. $|i_A, i_B\rangle \equiv |i_A\rangle \otimes |i_B\rangle$. The partial transpose of the ρ matrix with respect to the A subspace is given by:

$$\langle i_A, i_B|\rho^{T_A}|j_A, j_B\rangle \equiv \langle j_A, i_B|\rho|i_A, j_B\rangle \tag{3.11}$$

From Eq. 3.11 immediately follows the equality $\mathrm{Tr}\left[\rho^{T_A}\right] = \mathrm{Tr}\left[\rho\right] = 1$. If ρ represents a completely-separable state, also $\|\rho^{T_A}\| = \mathrm{Tr}\left[\rho^{T_A}\right] = 1$ for the Peres' criterion. Hence, by using the Eq. 3.10 one obtains $\mathcal{N}(\rho) = 0$. Otherwise, if the state is entangled, at least one eigenvalue μ_i of ρ^{T_A} is negative, and it follows:

$$\|\rho^{T_A}\| = \sum_{i=1}^{4} |\mu_i| = \sum_{i=1}^{4} \mu_i + 2\left|\sum_{\mu_i<0} \mu_i\right| \equiv 1 + \mathcal{N}(\rho) \tag{3.12}$$

Thus, the Negativity can be expressed depending on the negative μ_i eigenvalues:

$$\mathcal{N}(\rho) = 2\left|\sum_{\mu_i<0} \mu_i\right| \tag{3.13}$$

Eqs.3.10 and 3.13 give a Negativity definition that is simple to implement computationally, and show that for separable states $\mathcal{N}(\rho) = 0$, otherwise $\mathcal{N}(\rho) > 0$.

It is possible to demonstrate that the Negativity $\mathcal{N}$ is an increasing monotone function with respect to the amount of entanglement present inside the state under exam. First, $\mathcal{N}$ is a convex function. Given $\rho = \sum_i p_i\rho_i$ a density matrix referred to a mixed state, with $p_i \geq 0$, $\sum_i p_i = 1$, and where the ρ_i represent pure states density operators, then:

$$\mathcal{N}\left(\sum_i p_i\rho_i\right) \leq \sum_i p_i\mathcal{N}(\rho_i) \tag{3.14}$$

because the trace norm satisfies the triangular inequality (as every norm).

By exploiting an orthonormal and complete set of projective measurements $\{\mathcal{M}_i(\rho) = p_i\rho_i'\}$ onto the B subsystem, it applies that $\sum_i \mathrm{Tr}\left[\mathcal{M}_i(\rho)\right] = \mathrm{Tr}\left[\rho\right]$. Furthermore, by assuming that the decompositions of the projectors $\mathcal{M}_i$ do not exist, it follows:

$$\mathcal{M}_i(\rho) = (\mathbb{1}_A \otimes M_i)\rho(\mathbb{1}_A \otimes M_i^\dagger) \tag{3.15}$$

where all the M_i constitute a Kraus operator set [21], i.e. they satisfy the condition $\sum_i M_i^\dagger M_i \leq \mathbb{1}_B$. From Eq. 3.15, it is evident that by construction:

$$\mathcal{M}_i(\rho)^{T_A} = \mathcal{M}_i(\rho^{T_A}) \tag{3.16}$$

Since ρ^{T_A} is a self-adjoint operator, it can be decomposed as the linear combination of two positive operators [53]:

$$\rho^{T_A} = (1 + (N/2))\rho^+ - (N/2)\rho^- \tag{3.17}$$

where the operators $\rho^\pm$are density matrices, and $N = \mathcal{N}(\rho)$. By exploiting Eq. 3.16 it is obtained:

$$p_i(\rho_i')^{T_A} = \mathcal{M}_i(\rho)^{T_A} = \mathcal{M}_i(\rho^{T_A}) = (1 + (N/2))\mathcal{M}_i(\rho^+) - (N/2)\mathcal{M}_i(\rho^-) \tag{3.18}$$

Let me introduce the following lemma:

Lemma. *For each Hermitian operator A, there exists a minimal decomposition for which* $A = a_+\rho^+ - a_-\rho^-$. *Hence, one has that* $\|A\| = a_+ + a_-$, *where* $a_{-(+)}$ *is the absolute value of the A negative (positive) eigenvalues sum.*

By exploiting $(\rho_i')^{T_A}$ defined in Eq. 3.18, it is possible both to recognize the coefficient $a_- = (N/2p_i)$ and to define $\mathcal{N}(\rho_i')$, where the latter is subject to the constraint $\mathcal{N}(\rho_i') \leq (N/2p_i)$. Finally, by multiplying by p_i and by summing over the i it is obtained:

$$\sum_i p_i \mathcal{N}(\rho_i') \leq \mathcal{N}(\rho) \tag{3.19}$$

demonstrating that the Negativity is increasing monotonically with respect to the amount of entanglement.

Then, in order to have the maximum allowed value for Negativity one can simply calculate its value for a maximally-entangled state, e.g. for a Bell state [5] as $|\psi_-\rangle = (|01\rangle - |10\rangle)/\sqrt{2}$.

$$\rho_{\psi_-} = |\psi_-\rangle\langle\psi_-| = \begin{pmatrix} 0 & 0 & 0 & 0 \\ 0 & \frac{1}{2} & -\frac{1}{2} & 0 \\ 0 & -\frac{1}{2} & \frac{1}{2} & 0 \\ 0 & 0 & 0 & 0 \end{pmatrix}$$

$$\rho_{\psi_-}^{T_A} = \begin{pmatrix} 0 & 0 & 0 & -\frac{1}{2} \\ 0 & \frac{1}{2} & 0 & 0 \\ 0 & 0 & \frac{1}{2} & 0 \\ -\frac{1}{2} & 0 & 0 & 0 \end{pmatrix}$$

$$\mathcal{N}(\rho_{\psi_-}) = ||\rho_{\psi_-}^{T_A}|| - 1 = 1 \tag{3.20}$$

Therefore, by using Eqs. 3.13, 3.19 and3.20 it follows that:

$$0 \leq \mathcal{N}(\rho) \leq 1 \tag{3.21}$$

with $\mathcal{N} = 0$ for completely-separable states, and $\mathcal{N} = 1$ for maximally entangled states.

3.1.1 Concurrence

The second parameter used for estimating the amount of entanglement inside a bipartite state is the Concurrence. Historically, it was introduced as expansion of the concept of Entanglement of Formation (EoF) [68].

In general, Eq. 3.2 is not computable for mixed states. Therefore, it is useful the definition of EoF. Being ρ the density matrix of a generic mixed state, it can be expressed as statistical mixture of pure states:

$$\rho = \sum_i p_i |\psi_i\rangle\langle\psi_i| \equiv \sum_i p_i \rho_i \quad , p_i \in [0,1] \, , \sum_i p_i = 1 \tag{3.22}$$

The EoF associated with ρ is defined as the minimum (over all the possible ensembles of $\{\rho_i\}$) of the entanglement weighted mean calculated on the pure states for which Eq. 3.2 holds:

$$E = \min \sum_i p_i E(\psi_i) \tag{3.23}$$

By definition, the EoF is null for states that can be expressed as a product of pure states, i.e. for separable states. It can be used in order to define entanglement for density

matrices in the form of Eq. 3.22. For this reason, from this point it will simply be indicated as "entanglement". However, its form in Eq. 3.23 is not always computable as well as for entanglement definition in Eq. 3.2, thus Concurrence was introduced.

Let us consider bipartite state density matrices with two non-zero eigenvalues. Every statistical mixture of entangled states and separable states is represented by this kind of density matrices. In the particular case of two-photon states, it is possible to define the *magic* basis with the following four polarization states:

$$\begin{aligned} |e_1\rangle &= \frac{1}{\sqrt{2}}(|HH\rangle + |VV\rangle) \\ |e_2\rangle &= \frac{1}{\sqrt{2}}i(|HH\rangle - |VV\rangle) \\ |e_3\rangle &= \frac{1}{\sqrt{2}}i(|HV\rangle + |VH\rangle) \\ |e_4\rangle &= \frac{1}{\sqrt{2}}(|HV\rangle - |VH\rangle) \end{aligned} \tag{3.24}$$

These are the Bell's states expressed in function of the polarization, with proper global phases.

When a two-photon pure state $|\psi\rangle$ is written as $|\psi\rangle = \sum_{i=1}^{4} \alpha_i |e_i\rangle$, its corresponding entanglement can be expressed as a function of the α_i components. Let us define the following function:

$$\mathcal{E}(x) = H\left(\frac{1}{2} + \frac{1}{2}\sqrt{1-x^2}\right) \quad , 0 \leq x \leq 1 \tag{3.25}$$

where H is the Shannon's entropy [5]with respect to an event with probability vector $\vec{X} = (x, 1-x)$: $H(x) = -\left[x \log_2 x + (1-x)\log_2(1-x)\right]$. By using Eq. 3.2, the entanglement inside $|\psi\rangle$ is:

$$E(\psi) = \mathcal{E}(\mathcal{C}(\psi)) \tag{3.26}$$

where $\mathcal{C}(\psi)$ is the Concurrence:

$$\mathcal{C}(\psi) = \left|\sum_{i=1}^{4} \alpha_i^2\right| \tag{3.27}$$

It is convenient to rewrite the Eq. 3.26 for density matrices. It is introduced the operator $R(\rho)$:

$$R(\rho) = \sqrt{\sqrt{\rho}\rho^*\sqrt{\rho}} \tag{3.28}$$

The complex-conjugated ρ^* with respect to the magic basis is:

$$\rho^* = \sum_{i,j} |e_i\rangle\langle e_j|\rho|e_i\rangle\langle e_j| \tag{3.29}$$

It can be noticed from Eq. 3.28 that $\mathrm{Tr}\,[R] \in [0,1]$ quantifies the "distance" between ρ and ρ^*. Furthermore, $R(\rho)$ is invariant with respect to unitary transformations performed on a single subsystem composing the whole state ρ, as entanglement is.

Computationally, it is beneficial to reformulate the Concurrence as a function of the $R(\rho)$ eigenvalues, i.e. $R(\rho) = \sqrt{\sqrt{\rho}(\sigma_y \otimes \sigma_y)\rho^*(\sigma_y \otimes \sigma_y)\sqrt{\rho}}$ where σ_y is the y Pauli matrix. This can be done by exploiting the following theorem, introduced and demonstrated by Hill and Wooters [61].

Theorem. *Being ρ a bipartite-state density matrix, which has at most two non-zero eigenvalues, and λ_{max} the maximum eigenvalue of $R(\rho)$, the EoF of ρ will be given by:*

$$E(\rho) = \mathcal{E}(c), \quad c = \max\{0, 2\lambda_{max} - \mathrm{Tr}\,[R(\rho)]\} \tag{3.30}$$

where c is the Concurrence of ρ, and it corresponds to the definition given in Eq 3.27 when the state is pure.

Like E, also the Concurrence can assume values within the interval $[0, 1]$, and it is increasing-monotone with respect to the entanglement.

3.1.2 Log-Negativity

The last parameter considered for the entanglement estimation is the Log-Negativity, defined as:

$$\mathcal{LN}(\rho) \equiv \log_2(1 + \mathcal{N}(\rho)) = \log_2 ||\rho^{T_A}|| \tag{3.31}$$

Thus, by definition Log-Negativity is increasing-monotone with respect to the entanglement. Furthermore, it is an additive function, so it is useful for estimating the amount of entanglement inside multi-partite states represented by a density matrix in the form $\rho^{\otimes N}$.

3.1.3 Quantum Geometric Discord

As mentioned before, quantum states can be divided in two categories: separable states and entangled states. The latter category shows *non-local* properties, and it is an important tool for developing quantum technologies, whereas the former is considered *classical* in terms of correlations. Indeed, separable states do not violate the Bell's inequalities [5], but it is important to notice that also some non-separable state families do not, e.g. Werner's states [93]. However, there are other non-classical correlations aside entanglement, and they can represent a useful resource too. An example of this other type of non-classical correlations useful for quantum technologies is given by the discord [94].

In classical information theory, the correlation between two random variables A and B of a classical system is quantified by the mutual information:

$$I(A : B) = H(A) + H(B) - H(A, B) \tag{3.32}$$

where $H(\vec{p})$ is the Shannon's entropy referred to a random-variable probability-distribution vector, and $H(A, B)$ is the Shannon's entropy referred to the joint probability of A and B. Remaining in the classical framework, it is possible to exploit the Bayes' rule in order to rewrite Eq. 3.32:

$$I(A : B) = H(A) - H(A|B) \tag{3.33}$$

where $H(A|B)$ is the Shannon's entropy referred to the conditional probability distribution of A with respect to B.

The quantum equivalent of the Shannon's entropy is the von Neumann entropy $S(\rho)$. By exploiting it in Eqs. 3.32 and 3.33 (referred to subsystems ρ_A and ρ_B), one could obtain two different values of the mutual information $I(\rho)$: the difference between them defines the quantum discord.

A bipartite quantum state is defined inside the Hilbert space $\mathcal{H}_{AB} = \mathcal{H}_A \otimes \mathcal{H}_B$, given by the tensorial product of the Hilbert spaces to which the subsystems A and B belong.

By knowing the ρ density matrix of the whole state, the quantum analogous of the Eq. 3.32 is:

$$I(\rho) = S(\rho_A) + S(\rho_B) - S(\rho) \tag{3.34}$$

where $\rho_{A,B} = \mathrm{Tr}_{B,A}[\rho]$ are the reduced density matrices referred to the two subsystems.

In order to obtain the quantum version of the Eq. 3.33, the conditional von Neumann Entropy $S(\rho_{B|A})$ is required, in which $\rho_{B|A}$ represents the B state conditioned to a measurement over A. In contrast with classical measurements, quantum measurements cause the collapse of the wave function. Therefore, in order to have an alternative version of the mutual information one has to minimize on all the possible measurements of A:

$$Q_A(\rho) = S(\rho_B) - \min_{E_k} \sum_k S(\rho_{B|k}) \tag{3.35}$$

where $\rho_{B|k} = \mathrm{Tr}_A[(E_k \otimes \mathbb{1}_B)\rho] / \mathrm{Tr}[(E_k \otimes \mathbb{1}_B)\rho]$ is the state of B conditioned to the measurement of A realized by the POVM element E_k.

Thus, the quantum discord is defined by:

$$D_A(\rho) = I(\rho) - Q_A(\rho) \tag{3.36}$$

From Eq. 3.35 it is evident that the quantum discord is not symmetrical with respect to the subsystems A e B, then $D_A(\rho) \neq D_B(\rho)$ in general. It is always non-negative, and if $D_A(\rho) = D_B(\rho) = 0$, the state ρ is defined classically correlated. All other states are considered non-classical, and they might ensure an advantage in quantum algorithm with respect to the classical ones [94].

Unfortunately, Eq. 3.36 can be computed just for few quantum states [62]. Therefore, some quantum discord approximations have been introduced [95, 96]. For our work, we chose the quantum geometric discord (QGD), defined as:

$$D_A^{(2)}(\rho) = \min_{\chi \in \Omega_0} ||\rho - \chi||^2 \tag{3.37}$$

where Ω_0 is the ensemble of zero-discord states, and $||X||^2 = \mathrm{Tr}\left[X^2\right]$ is the square norm of an operator in the Hilbert-Schmidt space [97].

For a generic bipartite quantum state $\mathcal{H}_A = \mathcal{H}_B = \mathbb{C}^2$. Thus, its density operator can be written by exploiting the Bloch representation [5]:

$$\rho = \frac{1}{4}\left(\mathbb{1} \otimes \mathbb{1} + \sum_{i=1}^{3} x_i \sigma_i \otimes \mathbb{1} + \sum_{i=1}^{3} y_i \mathbb{1} \otimes \sigma_i + \sum_{i,j=1}^{3} T_{ij} \sigma_i \otimes \sigma_j\right) \tag{3.38}$$

where the σ_i are the Pauli's matrices, $x_i = \mathrm{Tr}[\rho(\sigma_i \otimes \mathbb{1})]$ and $y_i = \mathrm{Tr}[\rho(\mathbb{1} \otimes \sigma_i)]$ are the Bloch vector local components [5], $T_{ij} = \mathrm{Tr}[\rho(\sigma_i \otimes \sigma_j)]$ are the components of the correlation tensor. To each ρ, it is possible to assign the triplet $\{\vec{x}, \vec{y}, T\}$.

Now, it remains to define the states that belong to the Ω_0 set. A zero-discord bipartite state can be written in the form:

$$\chi = p_1 |\psi_1\rangle\langle\psi_1| \otimes \rho_1 + p_2 |\psi_2\rangle\langle\psi_2| \otimes \rho_2 \tag{3.39}$$

where $\{|\psi_1\rangle, |\psi_2\rangle\}$ is an orthonormal basis referred to a subsystem of the state, and $\rho_{1,2}$ are the marginal density matrices with their associated probabilities $p_{1,2}$ ($p_1 + p_2 = 1$). Let me define $t \equiv p_1 - p_2$ and the three following vectors:

$$\begin{aligned} \vec{e} &= \langle\psi_1|\vec{\sigma}|\psi_1\rangle \\ \vec{s}_\pm &= \mathrm{Tr}[p_1\rho_1 \pm p_2\rho_2]\,\vec{\sigma} \end{aligned} \tag{3.40}$$

where the elements of $\vec{\sigma}$ are the Pauli matrices. It is easy to demonstrate that $t\vec{e}$ and $\vec{s}_+$ represent the Bloch vectors respectively of the first and the second subsystem, while $\vec{s}_-$ is linked with the correlation tensor by the relation $T = \vec{e}\,\vec{s}_-^T$. Therefore, the Bloch representation of a zero-discord state is $\chi = \{t\vec{e}, \vec{s}_+, \vec{e}\,\vec{s}_-^T\}$, where $||\vec{e}|| = 1$, $||\vec{s}_\pm|| \leq 1$, and $t \in [-1, 1]$. The trace distance between ρ and χ is given by:

$$\begin{aligned} ||\rho - \chi||^2 &= ||\rho||^2 - 2\mathrm{Tr}\left[\rho\chi\right] + ||\chi||^2 = \\ &= \frac{1}{4}(1 + ||\vec{x}||^2 + ||\vec{y}||^2 + ||T||^2) - \frac{1}{2}(1 + t\vec{x}\cdot\vec{e} + \vec{y}\cdot\vec{s}_+ + \vec{e}^T T\vec{s}_-) + \\ &+ \frac{1}{4}(1 + t^2 + ||\vec{s}_+||^2 + ||\vec{s}_-||^2) \end{aligned} \tag{3.41}$$

In order to obtain the QGD, one has to find the minimum of the distance in Eq. 3.41 by optimizing the parameters t and $\vec{s}_\pm$. This distance is convex and quadratic with respect to the three vectors of Eq. 3.40, the Hessian matrix has no singularity and it is positive, and these conditions are sufficient for having a global minimum of the function, corresponding to the following constraints:

$$\begin{aligned} \frac{\partial}{\partial t}\left[||\rho - \chi||^2\right] &= \frac{1}{2}(t - \vec{x}\cdot\vec{e}) = 0 \\ \frac{\partial}{\partial \vec{s}_+}\left[||\rho - \chi||^2\right] &= \frac{1}{2}(-\vec{y} + \vec{s}_+) = 0 \\ \frac{\partial}{\partial \vec{s}_-}\left[||\rho - \chi||^2\right] &= \frac{1}{2}(-T^T\vec{e} + \vec{s}_-) = 0 \end{aligned} \tag{3.42}$$

with solution $t = \vec{x}\cdot\vec{e}$, $\vec{s}_+ = \vec{y}$ e $\vec{s}_- = T^T\vec{e}$. By substituting in Eq. 3.41 one obtains:

$$||\rho - \chi||^2 = \frac{1}{4}\left[||\vec{x}||^2 + ||T||^2 - \vec{e}^T(\vec{x}\vec{x}^T + TT^T)\vec{e}\right] \tag{3.43}$$

that admits a minimum in the case in which $\vec{e}$ is an eigenvector of the matrix $K = \vec{x}\vec{x}^T + TT^T$, corresponding to the maximum eigenvalue k_{max}. For this reason, by using the Eq. 3.37, a QGD definition easy to calculate is:

$$D_A^{(2)}(\rho) = \frac{1}{4}(||\vec{x}||^2 + ||T||^2 - k_{max}) \quad , D_A^{(2)}(\rho) \in [0, 0.5] \tag{3.44}$$

The QGD is scaled of a factor 2 with respect to the quantum discord: for maximally-entangled states $D_A^{(2)}(\rho) = 0.5$. Thus, it has to be doubled in order to properly estimate the amount of discord into the bipartite state under exam.

3.2 Estimators

For each chosen parameter, we implemented two estimators: one non-optimal and one optimal (i.e. saturating the quantum Cramér-Rao bound). Actually, optimal estimators, when easy to compute, are an excellent solution in practical applications. However, we have introduced both optimal and non-optimal estimators for each parameter, in order to provide a direct comparison between the uncertainties in these two cases to highlight the advantage granted by optimal estimators.

All of them allow estimating the corresponding parameter with a smaller number of measurements with respect to a full reconstruction of the density matrix. However, one

needs some *a priori* knowledge of the family of quantum systems we are going to test. As previously mentioned, our estimators are suited for quantum states whose density matrix can be expressed with Eq. 3.1, i.e. the ones that can be easily realized experimentally by means of our photon pair source based on type-II PDC.

We indicate with $P(|XY\rangle)$ the probability of measuring the polarizations X and Y respectively for the two photons of a bipartite quantum state. Defining a generic linear single-photon polarization as a function of the θ angle with respect to the horizon, its projector $\Pi_\theta = |s(\theta)\rangle\langle s(\theta)|$ (being $|s(\theta)\rangle = \cos\theta|H\rangle + \sin\theta|V\rangle$) is:

$$\Pi_\theta = \begin{pmatrix} \cos^2\theta & \sin\theta\cos\theta \\ \sin\theta\cos\theta & \sin^2\theta \end{pmatrix} \tag{3.45}$$

Therefore, the probability $P(|XY\rangle)$ is given by:

$$P(|s(\theta_A)s(\theta_B)\rangle) = \mathrm{Tr}\left[\rho(\Pi_{\theta_A} \otimes \Pi_{\theta_B})\right] \tag{3.46}$$

All the estimators we implemented are built in the $\{|+\rangle, |-\rangle\}$ polarization basis, with $|+\rangle = (|H\rangle + |V\rangle)/\sqrt{2}$ and $|-\rangle = (|H\rangle - |V\rangle)/\sqrt{2}$. We chose this basis because in our case it is sensitive to an eventual relative phase between the H and V polarization components introduced by the interaction with the measurement setup (described in the following).

3.2.1 Negativity and Concurrence

For states described by density matrices in the form of Eq. 3.1, the behavior of Negativity and Concurrence as a function of the entanglement coincide [98]. Thus, it is possible to exploit the same estimators for both parameters. For this aim, it is convenient to rewrite Eq. 3.1 in the following form:

$$\begin{aligned} \rho_{pq} &= p \begin{pmatrix} 0 & 0 & 0 & 0 \\ 0 & q & -\sqrt{q(1-q)} & 0 \\ 0 & -\sqrt{q(1-q)} & 1-q & 0 \\ 0 & 0 & 0 & 0 \end{pmatrix} + (1-p) \begin{pmatrix} 0 & 0 & 0 & 0 \\ 0 & q & 0 & 0 \\ 0 & 0 & 1-q & 0 \\ 0 & 0 & 0 & 0 \end{pmatrix} \\ &= \begin{pmatrix} 0 & 0 & 0 & 0 \\ 0 & q & -p\sqrt{q(1-q)} & 0 \\ 0 & -p\sqrt{q(1-q)} & 1-q & 0 \\ 0 & 0 & 0 & 0 \end{pmatrix} \quad ; \quad p, q \in [0,1] \end{aligned} \tag{3.47}$$

In our case, $q = 1/2$, but the following considerations are valid for the general case.

By calculating the Negativity (Eq. 3.13) and Concurrence (Eq. 3.30) for a generic state 3.47, one obtains:

$$\mathcal{N}(\rho_{pq}) = \mathcal{C}(\rho_{pq}) = 2p\sqrt{(1-q)q} \tag{3.48}$$

For the parameter in Eq. 3.48, the QFI is:

$$H(\mathcal{N}(\rho_{pq})) = \frac{1}{1-\mathcal{N}^2(\rho_{pq})} = \frac{1}{1-4p^2q(1-q)} \tag{3.49}$$

Therefore, by exploiting the quantum Cramér-Rao bound (see Eq. 3.3), the minimum uncertainty associated with the parameter in Eq. 3.48 is given by:

$$\sigma_{min}(\mathcal{N}(\rho_{pq})) = \sqrt{1-\mathcal{N}^2(\rho_{pq})} = \sqrt{1-4p^2q(1-q)} \tag{3.50}$$

Exploiting the fact that for the singlet state the theoretical $P(|++\rangle)$ is zero, whereas for a completely-decoherent state it is equal to 1/4, intuitively we defined the first (non-optimal) estimator as:

$$\epsilon\mathcal{N}_1 \equiv 4(1/4 - P(|++\rangle) \tag{3.51}$$

Afterwards, by optimizing the QFI (Eq. 3.9) we obtained the following optimal estimator:

$$\epsilon\mathcal{N}_2 \equiv P(|+-\rangle) + P(|-+\rangle) - P(|++\rangle) - P(|--\rangle) \tag{3.52}$$

where again the probabilities are defined as in Eq. 3.46, with $|\pm\rangle \equiv |s(\pm\frac{\pi}{4})\rangle$.

3.2.2 Log-Negativity

The Log-Negativity is defined as a function of the Negativity (see Eq. 3.31). Therefore, it is possible to exploit the estimators in Eqs. 3.51 and 3.52 in order to obtain the corresponding ones for the Log-Negativity.

In this case, the optimal uncertainty is:

$$\sigma_{min}(\mathcal{LN}(\rho_{pq})) = \sqrt{\frac{2^{-\mathcal{LN}(\rho_{pq})}(2 - 2^{\mathcal{LN}(\rho_{pq})})}{\log^2(2)}} = \frac{1 - 2p\sqrt{q(1-q)}}{\log^2 2(1 + 2p\sqrt{q(1-q)}} \tag{3.53}$$

The non-optimal estimator can be written as:

$$\epsilon\mathcal{LN}_1 \equiv \log_2[1 + \epsilon\mathcal{N}_1] = \log_2\left[1 + 4\left(\frac{1}{4} - P(|++\rangle)\right)\right] \tag{3.54}$$

whereas the optimal one will be:

$$\begin{aligned}\epsilon\mathcal{LN}_2 &\equiv \log_2[1 + \epsilon\mathcal{N}_2] \\ &= \log_2[1 + (P(|+-\rangle) + P(|-+\rangle) - P(|++\rangle) - P(|--\rangle))]\end{aligned} \tag{3.55}$$

3.2.3 Quantum Geometric Discord

In principle, estimators for quantum discord would work also for QGD, but for the sake of readability we had to rescale the estimators in order to achieve results in the range $[0, 0.5]$.

By using Eq. 3.44, for polarization states described by a density matrix in the form of Eq. 3.47 the QGM is given by [57]:

$$\mathcal{QGD} = 2p^2(1-p)q = \frac{\mathcal{N}^2}{2} \tag{3.56}$$

In Eq. 3.56 we show that, for the state family under exam, the QGD amount is half the square of the Negativity. Therefore, it is possible to exploit the Negativity estimators defined in Eqs. 3.51 and 3.52 for building QGD estimators.

Calculating the QFI, we obtained the behavior of the smallest achievable uncertainty associated with the QGD as predicted by the quantum Cramér-Rao bound:

$$\sigma_{min}(\mathcal{QGD}(\rho_{pq})) = \sqrt{2\mathcal{QGD}(\rho_{pq})(1 - 2\mathcal{QGD}(\rho_{pq}))} = 4p^2q(1-q)(1 - 4p^2q(1-q)) \tag{3.57}$$

The non-optimal QGD estimator is:

$$\epsilon\mathcal{QGD}_1 \equiv \frac{1}{2}\epsilon\mathcal{N}_1^2 = 8\left(\frac{1}{4} - P(|++\rangle)\right)^2 \tag{3.58}$$

and the optimal one is defined as:

$$\begin{aligned}\epsilon\mathcal{QGD}_2 &\equiv \frac{1}{2}\epsilon\mathcal{N}_2^2 \\ &= \frac{1}{2}\left(P(|+-\rangle) + P(|-+\rangle) - P(|++\rangle) - P(|--\rangle)\right)^2\end{aligned} \tag{3.59}$$

3.3 Experimental setup

The implemented experimental setup is shown in Fig. 3.1 [57].

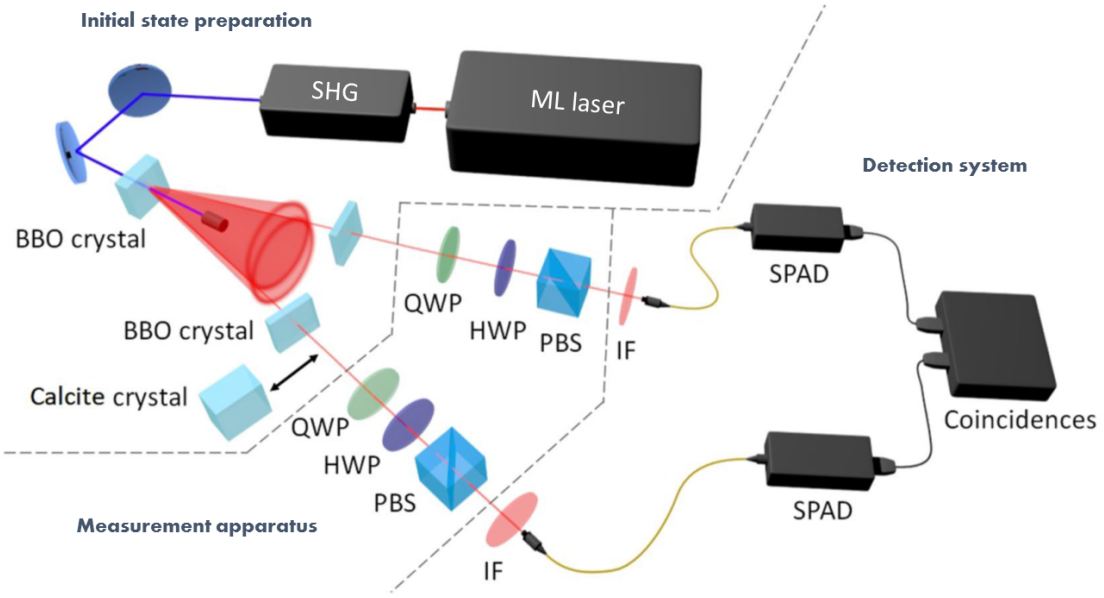

Figure 3.1: The experimental setup is composed of three parts. The first one is a type-II PDC based source of polarization entangled photons, composed by: a Ti:Sapphire mode-locked (ML) laser, a second harmonic generator (SHG), a BBO nonlinear crystal for PDC generation and two BBO crystals for walk-off compensation. A thick calcite birefringent crystal, with optical axis orthogonal to the photon propagation direction, can be inserted in the path of one photon for introducing temporal decoherence. The second part is a tomographic apparatus, that hosts a quarter-wave plate (QWP), a half-wave plate (HWP) and a polarizing beam splitter (PBS) in each branch. Finally, there is the detection part, comprising two interference filters (IFs), two fiber couplers injecting the photons into multi-mode fibers, that address them to Silicon single-photon avalanche diodes (SPADs), and coincidence electronics.

The family of entangled states represented by Eq. 3.1 can be obtained by exploiting the phenomenon of PDC. Thus, the first part of the setup consists of a source of polarization-entangled photons based on a scheme [41] exploited in many experiments concerning foundations of quantum mechanics and quantum technologies [82]. In particular, our source is based on a Ti:Sapphire mode-locked laser, emitting pulses with duration of 150 fs at 808 nm. Such laser beam induces the second harmonic generation in a lithium triborate (LBO) nonlinear crystal. Then, the resulting beam with a wavelength centered at 404 nm is used to pump a 0.5 mm thick β-barium borate (BBO) non-linear crystal, where type-II PDC occurs generating correlated photon pairs [99]. Two irises are used to spatially select the photons belonging to the intersections of the horizontally- and vertically-polarized

degenerate PDC cones (808 nm). On each of the two selected paths, a 0.25 mm thick BBO crystal is used to compensate the temporal delay between the horizontally- and the vertically-polarized photons induced by the birefringence within the PDC crystal.

At the output of these crystals, (ideally) the polarization-entangled photons are in the state:

$$|\psi_\phi\rangle = \frac{|HV\rangle + e^{i\phi}|VH\rangle}{\sqrt{2}} \tag{3.60}$$

where ϕ represents a relative phase between H and V. To produce the singlet state, we performed a fine tilting of one of the compensation BBO crystals, tuning the parameter ϕ until the value π (corresponding to the Bell state $|\psi_-\rangle$) was obtained.

It is possible to generate decoherence inside the produced state by introducing, in one of the two paths, an additional birefringent crystal sufficiently thick: in our case it was sufficient a 2.7 mm thick calcite crystal. In our experiment, we did not physically produce the set of quantum states described in Eq. 3.1, but we generated (independently and at different times) pure singlet states and completely decoherent states. To study states with different amount of decoherence, we realized a statistical mixture of our data in post-processing.

The measurement part consists of a typical polarization quantum tomographic apparatus [100]. Each path hosts a quarter-wave plate (QWP), a half-wave plate (HWP) and a polarizing beam splitter (PBS). The combination of this three elements allows projecting each photon polarization onto any state of the Bloch sphere surface.

Finally, there is the detection part. For each path, an interference filter spectrally selects the photons (within a wavelength band of 3 nm centered at 808 nm), then each photon is injected into a multi-mode fiber and sent to a Silicon single-photon avalanche diode (SPAD) for the detection. A dedicated time correlated counting system performs the temporal post-selection on photon counts.

3.4 Results

To determine the quality of the states generated by our setup, we reconstructed experimentally the density matrices of both the singlet state and the decoherent state by performing quantum state tomography. Then, we calculated the Uhlmann's Fidelity [101] of the reconstructed state with respect to the theoretically-expected one:

$$F = \mathrm{Tr}\left[\sqrt{\sqrt{\rho^{exp}}\rho^{th}\sqrt{\rho^{exp}}}\right] \quad , \quad F \in [0,1] \quad : \quad F = 1 \iff \rho^{exp} = \rho^{th} \tag{3.61}$$

where ρ^{th} indicates the theoretical density matrix and ρ^{exp} the reconstructed one. Since quantum state tomography does not provide uncertainties related to the reconstructed density-matrix elements, the fidelity parameter cannot be reported with an own uncertainty. For this reason, the fidelity is interpreted just as an indicator of the experimental-reconstruction goodness.

As can be inferred from Eq. 3.1, in the $\{|H\rangle, |V\rangle\}$ basis the theoretical density matrices of the singlet state $\rho^{th}_{|\psi_-\rangle}$ and the decoherent state ρ^{th}_{mix} are:

$$\rho^{th}_{|\psi_-\rangle} = \begin{pmatrix} 0 & 0 & 0 & 0 \\ 0 & \frac{1}{2} & -\frac{1}{2} & 0 \\ 0 & -\frac{1}{2} & \frac{1}{2} & 0 \\ 0 & 0 & 0 & 0 \end{pmatrix} \qquad \rho^{th}_{mix} = \begin{pmatrix} 0 & 0 & 0 & 0 \\ 0 & \frac{1}{2} & 0 & 0 \\ 0 & 0 & \frac{1}{2} & 0 \\ 0 & 0 & 0 & 0 \end{pmatrix} \tag{3.62}$$

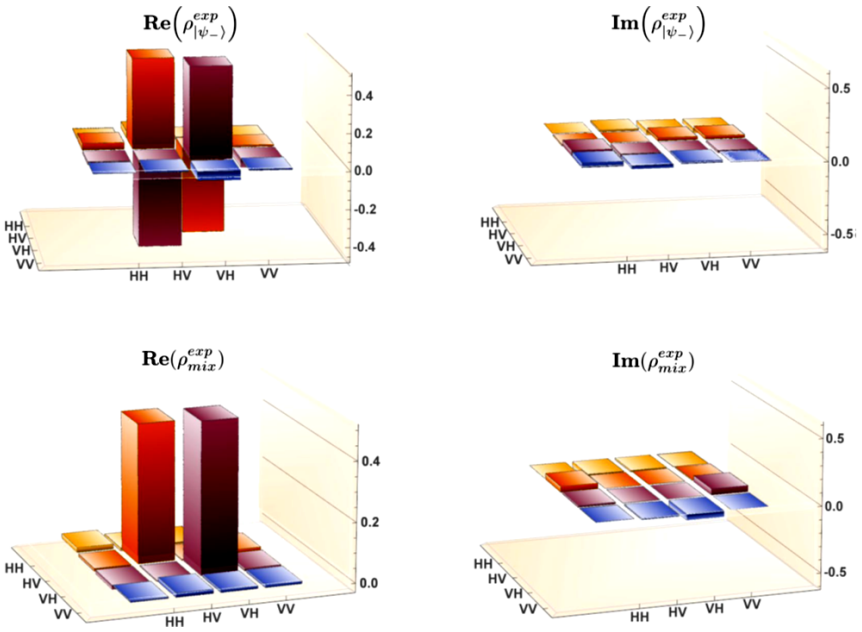

Figure 3.2: Real (left) and imaginary (right) part of the tomographically reconstructed density matrix for the singlet, maximally-entangled state (top) and the completely decoherent mixture (bottom).

The experimental tomographic reconstructions are showed in Fig. 3.2 [57].

By visually comparing the obtained graphs in Fig. 3.2 with the corresponding theoretical matrices in Eq. 3.62 one can argue that the experimental values are in good agreement with the predictions. This is confirmed by the values of the fidelity (see Eq. 3.61), respectively: $F_{\psi_-} = 0.975$ and $F_{mix} = 0.985$.

As mentioned before, for both states we performed all the measurements required for the estimators we were interested in, with an appropriate redundancy. In particular, for both the generated states we took 100 measurements of any possible polarization state of the basis $\{|++\rangle, |+-\rangle, |-+\rangle, |--\rangle\}$, then we divided them in 10 groups. For each group, we considered the mean value N_X^{AB}, where X indicates the singlet or the decoherent state and $A, B = +, -$ are related to the measured polarizations, and its standard deviation $\sigma_{N_X^{AB}}$ as statistical uncertainty. We underline that the $\sigma_{N_X^{AB}}$ have been independently evaluated on the data sample of each group, without any further statistical assumption.

Afterwards, we combined these groups in post-processing:

$$N^{AB}(p) = pN^{AB}_{|\psi_-\rangle} + (1-p)N^{AB}_{mix} \tag{3.63}$$

where p is defined in Eq. 3.1. This procedure was already exploited in several experiments [102, 103], and it is proven to give results indistinguishable from the ones obtained measuring a physical state with the same amount of decoherence.

The uncertainties have been propagated using the traditional statistical rules [104]:

$$\sigma_{N^{AB}} = \sqrt{p^2\sigma^2_{N^{AB}_{|\psi_-\rangle}} + (1-p)^2\sigma^2_{N^{AB}_{mix}}} \tag{3.64}$$

Each estimator ϵ was calculated using the counts in Eq. 3.63. Their statistical uncer-

tainties are extracted with the derivative method:

$$\sigma_\epsilon = \sqrt{\sum_{\{AB\}} \left(\frac{\partial \epsilon}{\partial N^{AB}(p)} \sigma_{N^{AB}(p)} \right)^2} \tag{3.65}$$

in which the sum is extended to all the involved polarization measurements. Such measured polarizations constitute an orthonormal basis for bipartite polarization states, i.e. they are linearly independent. For these reason, in Eq. 3.65 there are not covariance terms.

The experimental results and the related uncertainties of all the estimators are shown in Fig. 3.3 [57].

The experimental points concerning the estimators introduced in this paper are plotted vs. the mixing parameter p ranging from 0 (completely decoherent mixture) to 1 (pure entangled state). For each point, p is evaluated using the tomographic state reconstruction of the corresponding density matrix.

The uncertainty bars associated with the experimental points, defined in Eq. 3.65, represent the standard deviation of the measurement results statistical distribution, i.e. the statistical uncertainty associated with a single measurement. Experimental points are compared with the theoretical value of the estimator, represented by a dashed line. The experimental uncertainty bars are compared with the corresponding theoretical prediction, derived from the quantum Fisher information. Dotted curves represent the theoretical uncertainty for the non-optimal estimator, while solid curves indicate the theoretical uncertainty for the optimal estimator, i.e. the one achieved by saturating the quantum Cramér-Rao bound, representing the minimum uncertainty allowed by quantum estimation theory.

All the theoretical curves shown in Fig. 3.3 are calculated exploiting the knowledge of the experimental values of the parameters p and q (see Eq. 3.47), obtained from the tomographic reconstruction of the density matrices (see Fig. 3.2) of the states involved in the experiment. In Fig. 3.3 different colors have been used for distinguishing the parameters. In particular, the blue is for Negativity and Concurrence, the orange for Log-Negativity and the green for QGD. On the left side of Fig. 3.3 are shown the graphs concerning the non-optimal estimators for each parameter, whereas on the right side one can find the optimal estimators graphs. The figure shows a good agreement between experimental results and theoretical predictions for each estimator, both for the value itself and the statistical uncertainty associated with it. This is particularly relevant and interesting for the optimal estimators case, where our results demonstrate saturation of the quantum Cramér-Rao bound.

As anticipated in the introduction, we have demonstrated optimal estimation of entanglement and discord in two-photon states, showing how optimal estimators are able to saturate the quantum Cramér-Rao bound and, this way, outperform non-optimal estimators in terms of uncertainty. A further remarkable result emerging from this work is that, for the family of quantum states taken into account, there is an identity between the estimators for Negativity and Concurrence, and a smooth monotone relation between the ones for Negativity and Quantum Geometric Discord. Such result was not expected a priori but leads to direct relations between estimators and related quantum Cramér-Rao bound. Therefore, knowing the quantum Cramér-Rao bound and the optimal estimator for Negativity allows an immediate derivation of such quantities also for Log-Negativity, Concurrence and Quantum Geometric Discord. These results pave the way to the diffuse use of these estimators in quantifying resources for quantum technologies.

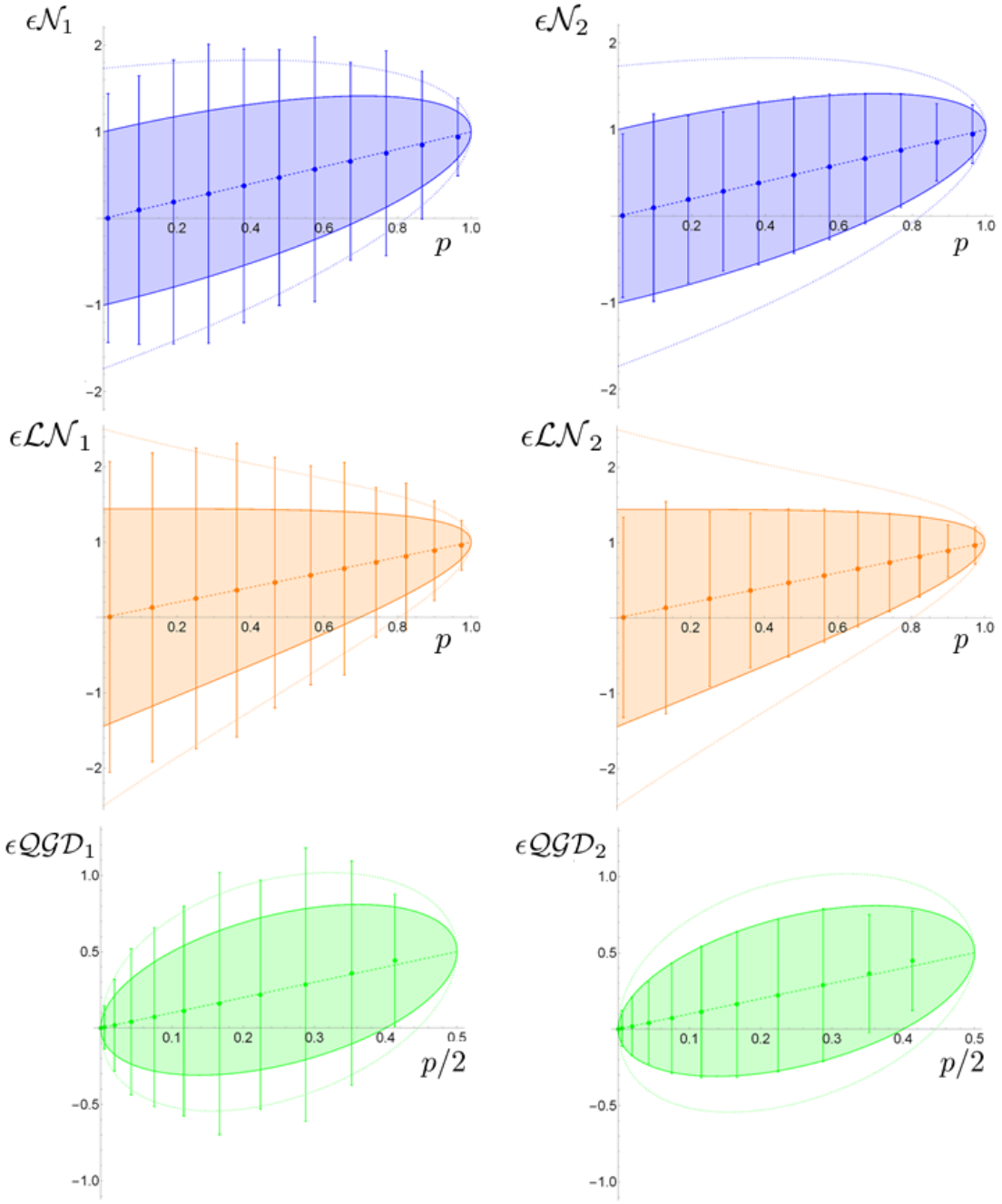

Figure 3.3: Results for Negativity and Concurrence (blue), Log-Negativity (orange), and Quantum Geometric Discord (green) non-optimal (left side) and optimal (right side) estimators, with respect to p (see Eq. 3.47). Experimental points are compared with: theoretical value of the quantity to estimate (dashed line), theoretical uncertainty for the non-optimal estimator (dotted curve) and theoretical uncertainty related to the quantum Cramér-Rao bound (solid curve).

Chapter 4

Beyond the quantum Cramér-Rao bound: Genetic Quantum Measurement

4.1 Introduction

In physics, there exist several quantities of interest that are not directly accessible, either in principle or because of experimental impediments. This is particularly true for quantum mechanical systems, where relevant quantities like entanglement and purity are nonlinear functions of the density matrix and cannot, even in principle, be associated with a proper observable. In these situations indirect measurements are exploited, inferring the value of the quantity of interest by inspecting a set of data coming from the measurement of a different observable, or a set of observables. Therefore, it is of particular interest the field of quantum estimation theory (QET), that provides tools for such parameters estimation problem.

QET can be divided in two main paradigms [59,91]: *global* and *local* QET. The former looks for the POVM minimizing a suitable cost functional, averaged over all possible values of the parameter to be estimated. The result of a global optimization is thus a single POVM, independent on the value of the parameter. The latter, instead, looks for the POVM maximizing the Fisher information (see Eq. 3.4), thus minimizing the variance of the estimator, at a fixed value of the parameter. Global QET has been mostly applied for finding optimal measurements and for evaluating lower bounds on precision for parameters estimation, imposed by unitary transformations. Anyway, euristically one can expect that local QET performs better than global QET, since the optimization concerns a specific value of the parameter, with some adaptive or feedback mechanism granting the possibility to achieve the ultimate precision bound.

In the previous chapter, the definition of optimal measurement has been given, according to local QET paradigm, by introducing the Cramér-Rao bound criterion [91]. However, one could ask: is there a scenario in which it is possible to achieve uncertainties smaller than the minimum one allowed by an optimal measurement, corresponding to the saturation of the quantum Cramér-Rao bound? The aim of this section is to provide an affirmative answer to this question, illustrating a novel quantum measurement paradigm able to go beyond the quantum Cramér-Rao bound in terms of precision.

In the traditional QM framework, measurements cause the collapse of the wave function, because the state $|\psi\rangle$ undergoes a projection onto the eigenstate $|\phi_i\rangle$ corresponding to the

measured eigenvalue α_i. For this reason, those measurements are dubbed *projective*. To obtain the expectation value of an observable $\mathcal{O}$, it is required a statistical evaluation of the experimental results on several identical copies of the same quantum state:

$$\langle \mathcal{O} \rangle = \langle \psi | \mathcal{O} | \psi \rangle = \sum_i p_i \alpha_i \tag{4.1}$$

where p_i represents the probability associated with the outcome α_i. Experimentally, it is possible to extract the p_i probabilities over a large enough amount M of identical copies of the state $|\psi\rangle$. By exploiting the results obtained on an ensemble of identically-prepared quantum states, the statistical uncertainty associated with $\langle \mathcal{O} \rangle$ is calculated as the standard deviation of the measurement outcomes distribution.

However, there are cases in which it can be difficult to realize an experimental setup able to produce several identical copies of a chosen quantum state. Therefore, the search for novel measurement paradigms able to achieve satisfactory uncertainties with a small amount of initial resources (here identified with the quantum states to be produced) is a crucial task of nowadays Quantum Metrology.

For this reason, we designed a new measurement protocol that we dubbed Genetic Quantum Measurement (GQM), because, as will be shown in the following, it seems to naturally exploit some evolution-inspired mechanisms reminding the ones of genetic algorithms [105] in Computer Science.

These algorithms are used for finding solutions of optimization and research problems [106, 107]: they start from an initial ensemble of solutions, then, by exploiting iterative processes organized in subsequent steps, they select the optimal solution. Each step can be divided in three phases, mimicking the dynamics of natural evolution. The first one is called *mutation*, because the ensemble entities undergo a random swing. The second one is a *crossover* phase, in which the mutated entities are recombined, producing a "new generation" of solutions. Finally, the last one is a *selection* process, in which the least fitting solutions are discarded.

In von Neumann measurement scheme [27], the measurement of an observable over a quantum state is described exploiting a unitary operator, U_{vN}, coupling the observable of interest (OoI) $\mathcal{O}$ with an ancillary observable $\mathcal{P}$ called *pointer*:

$$U_{\mathrm{vN}} = \exp\left[ig\mathcal{P} \otimes \mathcal{O}\right] \tag{4.2}$$

where we use the units system $\hbar = 1$, and g is the coupling constant, representing the intensity of the interaction. The information on the OoI is extracted by the reading of the meter observable $\mathcal{X}$, canonically conjugated with $\mathcal{P}$.

An example of von Neumann interaction regarding single-photon states measurement is shown in Fig. 4.1. In this case, the measured quantum system is a single photon and the OoI is the horizontal component of the polarization, represented by the projector $\Pi_H = |H\rangle\langle H|$ over the horizontal polarization state $|H\rangle$. The coupling unitary operator is:

$$U = \exp\left[ig\mathbf{P} \otimes \Pi_H\right] \tag{4.3}$$

where the $\mathbf{P}$ observable is the momentum in a transverse direction with respect to the photon propagation axis, and again $\hbar$ is set equal to 1. In this framework, the meter corresponds to the position X along the direction to which $\mathbf{P}$ belongs.

GQM protocol represents an evolution of von Neumann measurements, introducing an iterative approach able to outperform "traditional" von Neumann measurements in terms of uncertainty. In Fig. 4.1 are shown the first steps of a GQM. The initial polarization state

$|\psi_\theta\rangle$ is prepared by exploiting a polarizer, in which a state-filtering projection $|\psi_\theta\rangle\langle\psi_\theta|$ occurs. Then, in each GQM step, a von Neumann interaction spatially separates (blue circles) in different "paths" the wave functions conjugated with the pointer observable, a mechanism that can be regarded as a "mutation" in evolutionary terms. After that, the photons undergo a projection $\Pi_\theta = |\psi_\theta\rangle\langle\psi_\theta|$ onto the initial state, i.e. same kind of state-filtering occurred in the initial-state preparation stage. This projection can be regarded as a selection mechanism, because it introduces a survival probability associated to each evolutionary path: the closer the path is to the "right" one, i.e to the one corresponding to $|\psi_\theta\rangle$, the higher will be the photon survival probability.

From the second step onwards, thanks to the coherent superposition of some "evolutionary paths" (orange circles), with the same von Neumann interaction also a crossover mechanism occurs, thanks to the coherent recombination of some of the wave functions at the end of the mutation process. At the end of the step, the same state filtering as the one of the preparation stage is made (selection). Furthermore, thanks to the quantum parallelism [17], one of the key features of many quantum technologies, e.g. quantum computation, all the possible evolutionary paths are inspected at the same time, granting a major advantage with respect to any classical implementation of such a bio-inspired measurement paradigm.

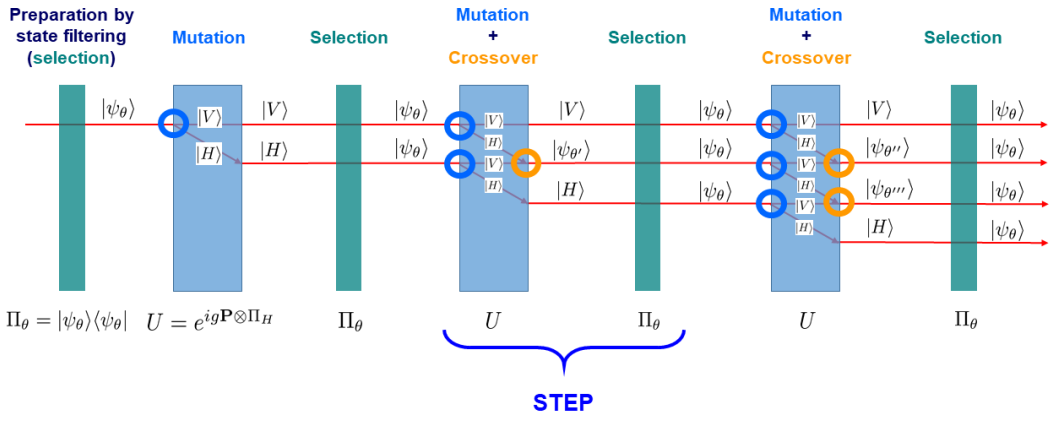

Figure 4.1: GQM scheme: after the initial state-filtering preparation of the polarization $|\psi_\theta\rangle$, the single photons pass through K GQM steps, each one composed by a von Neumann interaction, represented by the operator U, in which the mechanisms of mutation (blue rings) and crossover (orange rings) occur, and a selection performed by projecting onto the initial state $|\psi_\theta\rangle$.

GQM allows obtaining uncertainties below the ones related to the saturation of the quantum Cramér-Rao bound (i.e. the ones associated with optimal measurements). This is due to the fact that, in each step, the selection mechanism exploits *a priori* information on the parameter to be estimated (the photon polarization, in our experiment), i.e., the POVM describing the GQM is parameter-dependent [108, 109]. In this scenario, the quantum Cramér-Rao bound does not hold [91], then there is no violation of QM principles. Therefore, a correct application of GQM can be the characterization of the state filtering

process producing the quantum system under exam, instead of measuring the system itself. For example, let us imagine a quantum mint, that produces quantum coins exploiting a state filtering. If one wants to measure the fairness of this mint, i.e. that the generated quantum coins are not rigged, by using the GQM protocol (exploiting such state filtering as a selection mechanism) will cost less coins than the ones required by a prepare-and-measure strategy to achieve a certain precision.

GQM approach has some analogies (but also significant differences) with respect to a couple of well established theoretical measurement paradigms, namely Sequential Measurement (SM) [110, 111] and Protective Measurement (PM) [112–120]. Specifically, SMs exploit a sequence of interactions analogously to GQMs, but without introducing the selective pressure (the selection measurements in GQMs) and with the aim of estimating a parameter of the interaction rather than a quantum observable. For this reason, sequential measurements do not take advantage of an ancillary Hilbert space (the one of the Pointer observable in the GQMs case). Furthermore, this theoretical idea assumes to be able to obtain some data/information after each interaction without detecting the individual quantum system considered (i.e. without inducing the wave function collapse), a very challenging experimental task. On the contrary, the GQM approach extracts the information on the expectation value of the OoI only at the final detection stage by the measurement of the meter observable: a simpler scheme from the experimentalist's point of view.

The PM concept is somehow analogous to the one of GQM, since it takes advantage of a continuous protection of the quantum state (through a potential, or a quantum-Zeno-like [121] projective measurement) that is connected with an asymptotically infinite sequence of extremely weak interactions. In analogy with GQMs, the OoI estimation is obtained by measuring a pointer observable in an ancillary Hilbert space. The main concept behind PM is that a reliable estimation of the average value of the OoI can be performed by the detection of a SINGLE quantum system. This is possible, from a theoretical point of view, because at each step the interaction is so weak that the probability of losing a photon, through the potential barrier or because of the state-projection, is negligibly small even after an infinite amount of such interaction-protection steps. Obviously, it is experimentally impossible to have the full control at the low level of interaction strength needed, and, at the same time, to realize something even only approximating an infinite amount of interaction-protection steps. GQM approach considers a finite amount of interaction-selection stages (ranging from few units to hundreds, or even thousands) and investigates any interaction intensity, from weak to strong, in order to optimize the trade-off between single quantum system survival and uncertainty reduction. On the contrary, PM pertains only in the domain of weak interactions, because, for the protection mechanism to work properly, the interaction between measured system and measurement apparatus must be faint enough not to cause any wave function collapse.

In the next section, we will illustrate in detail the GQM theoretical framework experimental results related to our GQM proof-of-principle implementation with single-photon states, generated by a PDC-based heralded [122] single-photon source (see also Section §2.2.1).

4.2 Theoretical model

In this section, the GQM theoretical model is described by using the case of our experiment, where the OoI is the polarization of single photons. The corresponding operator is:

$$P = |H\rangle\langle H| - |V\rangle\langle V| \tag{4.4}$$

where H and V are the horizontal and the vertical polarization components, respectively.

As previously mentioned, measurements are indirectly performed onto the pointer Hilbert space. In our case, we exploit the spatial distribution of the quantum state in one of the directions orthogonal with respect to its momentum. After the initial state filtering, the single-photon states are described by:

$$|\Psi_{in}\rangle = |f_x\rangle \otimes |\psi_\theta\rangle \tag{4.5}$$

Where $|f_x\rangle$ represents the spatial distribution of the single photons, while $|\psi_\theta\rangle$ is the polarization state. In our case, these two different single-photon degrees of freedom are described by:

$$\begin{aligned} |\psi_\theta\rangle &= \cos\theta|H\rangle + \sin\theta|V\rangle \\ |f_x\rangle &= \int dx\, f(x)|x\rangle \\ f(x) &= \frac{1}{\sqrt[4]{2\pi\sigma^2}} e^{-\frac{x^2}{4\sigma^2}} \end{aligned} \tag{4.6}$$

i.e. the spatial distribution is Gaussian, and the polarization is linear.

The unitary operator assigned to each interaction is described in Eq. 4.3, where g is the spatial walk-off between the H and V polarizations due to the birefringence of the crystals, and it is proportional to the intensity of the interaction; $\mathbf{P}$ is the momentum operator and $\Pi_H = |H\rangle\langle H|$ is the projector over the H polarization component (OoI).

Birefringent crystals induce also a temporal walk-off between $|H\rangle$ and $|V\rangle$, but this corresponds to a relative phase between the polarization component that can be difficult to manage experimentally. In order to avoid this issue, we used a pair of birefringent crystals for each interaction: the first one with optical axis 45 ° tilted with respect to the photon propagation direction, and the second one with optical axis orthogonal to the photon propagation direction. By choosing a proper thickness of the crystals, it is possible to induce the desired spatial walk-off while compensating the temporal one.

After K steps, thanks to the selecting projections $|\psi_\theta\rangle\langle\psi_\theta|$, for each single photon it turns out the following (not-normalized) state:

$$|\Psi_{out}\rangle = (\Pi_\theta U)^K |\Psi_{in}\rangle = (\langle H|\Pi_\theta|H\rangle e^{ig\mathbf{P}} + \langle V|\Pi_\theta|V\rangle \mathbb{1}_x)^K |\Psi_{in}\rangle \tag{4.7}$$

where $\mathbb{1}_x$ is the identity matrix of the meter Hilbert space.

The survival probability of the single photon after K step is:

$$P_s(K) = Tr\left[|\Psi_{out}\rangle\langle\Psi_{out}|\right] \tag{4.8}$$

while the probability to reveal the single photon in the position x_0 is:

$$\begin{aligned} F_K(x_0) &= \frac{Tr\left[|x_0\rangle\langle x_0|\Psi_{out}\rangle\langle\Psi_{out}|\right]}{P_s(K)} \\ &= \frac{1}{P_s(K)} \left[\sum_i \langle i|x_0\rangle\langle x_0|(\Pi_\theta U)^K|\Psi_{in}\rangle\langle\Psi_{in}|(U^\dagger\Pi_\theta)^K|i\rangle\right] \\ &= \frac{1}{P_s(K)} \left[|\langle x_0| \sum_{n=0}^{K} \frac{K!}{n!(K-n)!} \langle H|\Pi_\theta|H\rangle^n \langle V|\Pi_\theta|V\rangle^{K-n} |\Psi_{in}\rangle|^2\right] \\ &= \frac{1}{P_s(K)} \left(\sum_{n=0}^{K} \frac{K!}{n!(K-n)!} \langle H|\Pi_\theta|H\rangle^n \langle V|\Pi_\theta|V\rangle^{K-n} f(x_0+ng)\right)^2 \end{aligned} \tag{4.9}$$

GQM scheme in Fig. 4.1 shows that mutation, crossover and selection processes determine the probability of observing the single photon over different evolutionary paths, each characterized by its own survival probability. For example, with $|\psi_\theta\rangle = |+\rangle = (|H\rangle + |V\rangle)/\sqrt{2}$, i.e. the polarization state that undergoes the maximum spatial decoherence from the birefringent crystals, the first mutation interaction divides the components of the entering polarization state in two paths with equal survival probability. At the end of the birefringent crystal pair, both the paths passing through the selection $\Pi_+ = |+\rangle\langle+|$ host a photon survival probability equal to 50%. Naïvely, one may think that, after K identical steps, the survival probability of the single photon undergoing the GQM is 2^{-K}. Actually, such probability is much higher because of the crossover mechanism [123], and it can be easily understood by extending the analysis to the first two steps, as shown in Fig. 4.2.

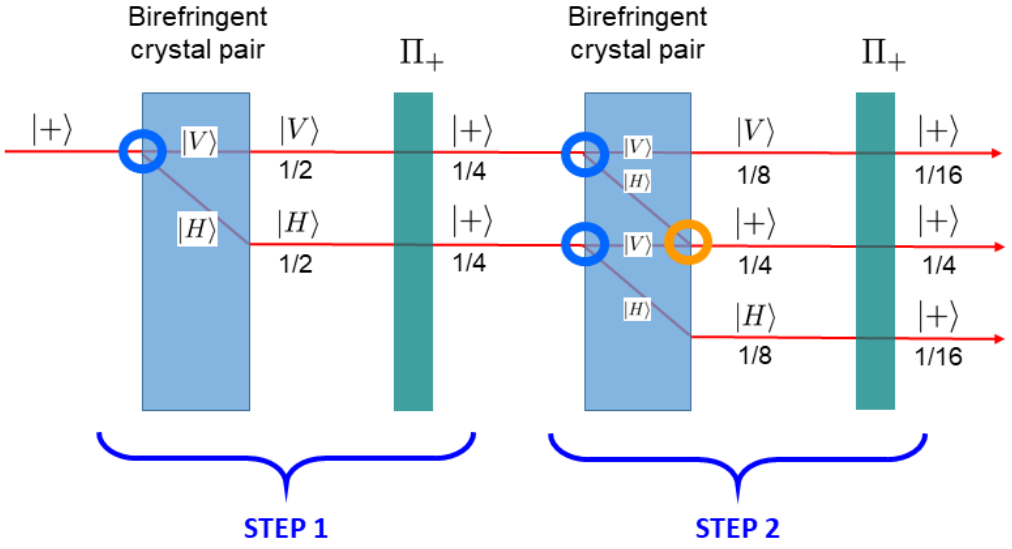

Figure 4.2: First two steps of the GQM protocol with initial polarization state $|\psi_\theta\rangle = |+\rangle$. Each birefringent crystal pair spatially separates $|H\rangle$ and $|V\rangle$. Numbers under the state vectors in the evolutionary paths are the probability that the photon will be mutated/ crossbreed by the birefringence, whereas after each polarizer these numbers represent the product of the mutation/crossover probability and the survival probability after the selection. After the second step, thanks to the crossover, the initial state $|\psi_\theta\rangle$ is recombined over a specific path, forming a $|+\rangle$ state left unperturbed by the subsequent selection process. Thus, the whole survival probability is $\frac{1}{16} + \frac{1}{4} + \frac{1}{16} = \frac{3}{8}$: higher than 2^{-2} (the naïve one).

There we can observe that, in the second step, the coherent superposition of two different paths reproduces a crossbreed state equal to the initial one with probability 50%. Thus, at the end of the second step the survival probability is:

$$P_s(K=2) = \frac{1}{2} \cdot \frac{3}{4} = \frac{3}{8} > \frac{1}{4} \tag{4.10}$$

as showed in Fig. 4.2.

As the number of implemented steps K increases, so do the survival probabilities belonging to the paths corresponding to polarization states close to the one of the initialization/selection filter $|\psi_\theta\rangle\langle\psi_\theta|$.

For $K = 7$ and $K = 100$ steps respectively, in Figs. 4.3 and 4.4 it is shown the behavior of the survival probability depending on the initial polarization state $|\psi_\theta\rangle$ and the (rescaled) intensity of the birefringence interaction g/σ, where g is the spatial walk-off induced in each step by the birefringent crystal pair, and σ is the waist of the initial spatial distribution of the single photon spatial wave function.

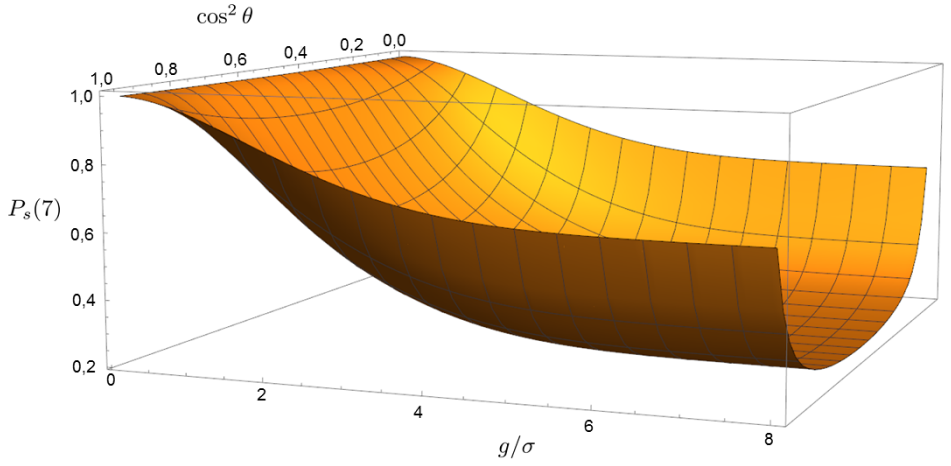

Figure 4.3: Behavior of the survival probability $P_s(K)$ as a function of both the initial state $|\psi_\theta\rangle$, with H polarization component $\cos^2\theta$ and the intensity of the interaction g/σ after $K = 7$ steps.

In Fig. 4.4, it is possible to see that, even for $K = 100$,the survival probability $P_s(100)$ never goes below 10^{-2}. This is surprising, because since after the first step for $|\psi_\theta\rangle = |+\rangle$ the survival probability is $1/2$, intuitively one could think that $P_s(100)$ would be $2^{-100} \sim 10^{-30}$. This 28 orders of magnitude discrepancy is due to the crossover between mutated states. For this reason, together with the quantum parallelism, GQMs allow achieving an effective, disruptive advantage in terms of precision with respect to traditional (projective) quantum measurements, as we will now demonstrate.

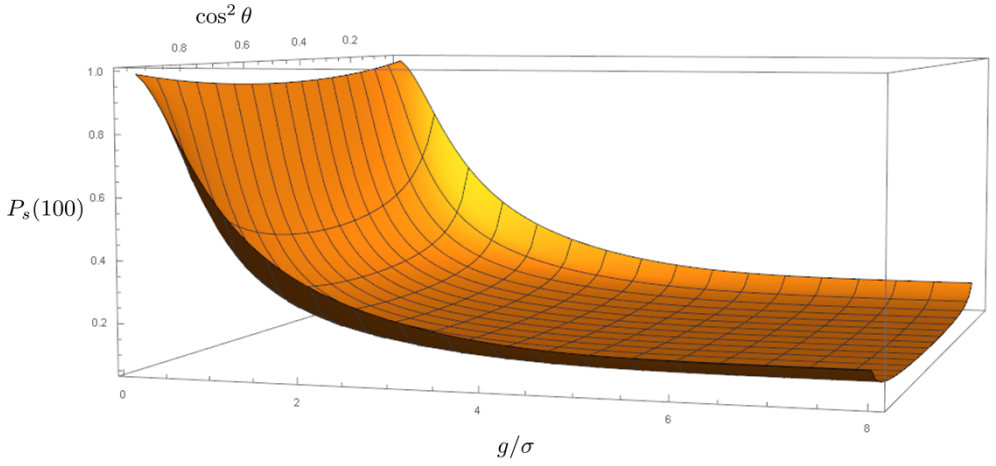

Figure 4.4: Behavior of the survival probability $P_s(K)$ in function of both the initial state $|\psi_\theta\rangle$, with H polarization component $\cos^2\theta$ and the intensity of the interaction g/σ after $K = 100$ steps.

As written before, the measurement of the spatial distribution of the photon at the end of the GQM allows estimating the expected value of the initial polarization state. Therefore, the precision of such estimation depends on the following uncertainty:

$$u(x) = \sqrt{\langle x^2\rangle - \langle x\rangle^2} \quad , \langle x^n\rangle = \int dx\, x^n F_K(x) \tag{4.11}$$

where $F_K(x)$ is defined in Eq. 4.9.

Thus, it is possible to notice the correspondence between the expectation value $\langle P\rangle$ defined in Eq. 4.4, and the average position of the single-photon state spatial distribution $\langle x\rangle$. By assuming a translation in the x axis of $-gK/2$ in order to obtain an analogy with the well-known Stern and Gerlach experiment [5], the uncertainty $u(P)$ associated with $\langle P\rangle$ can be easily obtained by rescaling the one of the meter observable X (canonically conjugated with P):

$$u(P) = \frac{2}{gK} u(x) \tag{4.12}$$

For this analysis, it is useful to compare the uncertainties theoretically obtained with GQM with the ones achievable with projective measurement, e.g. by using a polarizing beam splitter (PBS). For a projective measurement, by starting with M photons in the initial state polarization $|\psi\rangle$ (Eq. 4.6), the probability to observe m photons with polarization $|H\rangle$ (so $M - m$ photons in $|V\rangle$) is given by the binomial coefficient multiplied by the parameter $(\cos\theta)^2$. Therefore, the theoretically-predicted average polarization is $P = \frac{2m}{M} - 1$, whereas the associated uncertainty is:

$$u_{PBS}(P) = \sqrt{\langle P^2\rangle - \langle P\rangle^2} = \frac{|\sin(2\theta)|}{\sqrt{M}} \tag{4.13}$$

This uncertainty is considered *optimal*, because the quantum Fisher information [91] is in

this case $H(\theta) = \sin^{-2}(2\theta)$, saturating the quantum Cramér-Rao bound [91] and allowing for the minimum quantum uncertainty on the estimated parameter.

In order to do a fair comparison, we have to consider the same amount M of initial photons for both measurement protocols. Hence, in GQM we have to take into account the survival probability $P_s(K)$ of the initial polarization state after K steps: in principle, for detecting one photon at the end of a K-step GQM it is needed $M = 1/P_s(K)$. In our analysis, for both GQM and projective measurement protocols we considered $M = 1/P_s(K)$ initial photons. The ratio between GQM and projective measurement uncertainties is:

$$R = \frac{u_{PBS}(P)}{u(P)} \tag{4.14}$$

where $u_{PBS}(P)$ and $u(P)$ are respectively defined in Eqs. 4.13 and 4.12.

In Fig. 4.5 the behavior of R is shown as a function of the initial state polarization $|\psi_\theta\rangle$ (represented by $\cos^2\theta = \langle\psi_\theta|\Pi_H|\psi_\theta\rangle$) and the intensity g/σ of the GQM interactions. The surface in yellow is for $K = 7$, the one in blue corresponds to $K = 100$, whereas the magenta one is the $R = 1$ plane, representing the threshold below which GQM is disadvantageous with respect to projective measurement.

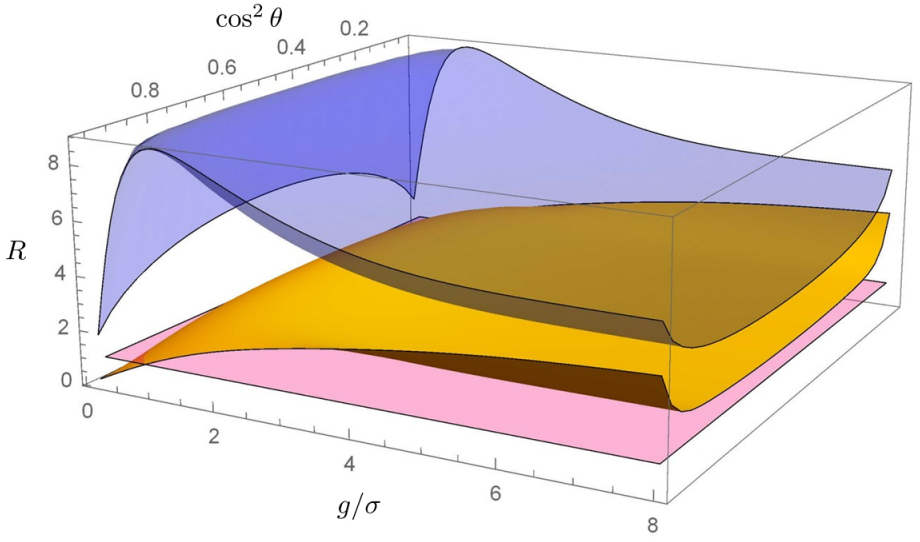

Figure 4.5: Ratio $R = \frac{u_{PBS}(P)}{u(P)}$ between projective measurement and GQM uncertainties. For fixed $K = 7$ (yellow) and $K = 100$ (blue) GQM steps, it is showed R depending on both the initial horizontal polarization component $\cos^2\theta$ and the von Neumann interaction intensity g/σ. The amount of initial photons exploited for both measurement protocols is $M = 1/P_s(K)$ in order to have the same initial resources for both measurements. The surface in magenta is the plane $R = 1$: above it GQM is advantageous in terms of uncertainty with respect to projective measurement.

In both $K = 7$ and $K = 100$ cases it is possible to notice that GQM is almost always more advantageous with respect to projective measurement: in fact, we have $R < 1$ just for extremely weak intensities of GQM interactions ($g/\sigma < 0.02$). These are the cases in which the spatial displacement induced by GQM birefringent crystals is too low for granting a proper resolution power to the measurement process. In our experiment, with $g/\sigma \sim 0.4$ and just $K = 7$, a 10% advantage is already present for most of the possible states, even if the maximum for R corresponds to $g/\sigma \sim 1$. For $K = 100$, instead, the reasonably weak interaction $g/\sigma \sim 0.4$ grants the maximum of the advantage ($R > 8.5$ almost everywhere), while for stronger interaction the advantage is reduced to $R < 4$.

The advantage of the GQM technique comes from the very high survival probability of the single photons. This is due to the fact that, in presence of a sequence of identical interaction-selection stages as in our scheme, the relative probability of losing a photon in a selection step decreases with the single photon advancing in the sequence, since it is more likely to find the photon close to the "right paths" created in our K interaction-selection steps.

4.3 Experimental setup

Our experimental setup (Fig. 4.6) is essentially composed of three parts. The first part (launcher and state preparation/selection) produces single photons in well-defined polarization states, by means of a heralded single-photon source (SPS) [124] based on Type-I PDC. In the second part (genetic evolution) we have created $K = 7$ steps of interaction and the selection mechanisms, implemented by means of birefringent crystal pairs and polarization filters. Finally, in the third part (detection) the photons are detected by a two-dimensional (2D) spatial-resolving detector which consists of an array of single-photon detectors. The SPS is based on a 796 nm mode-locked Ti:Sapphire laser (repetition rate: 76 MHz), whose second harmonic emission pumps a $10 \times 10 \times 5$ mm $LiIO_3$ non-linear crystal, in which correlated photons are produced by PDC. The idler photons ($\lambda_i = 920$ nm) are coupled to a single-mode fiber (SMF) and then addressed to a Silicon Single-Photon Avalanche Diode (SPAD) operated in Geiger mode, heralding the presence of the correlated signal photons ($\lambda_s = 702$ nm). These, after being SMF-coupled, are addressed to a launcher injecting them into the free-space optical path where the GQM protocol is implemented. After the launcher, the heralded single photons are collimated in a Gaussian mode by a telescopic system, and then prepared in the linear polarization state $|\psi_\theta\rangle$ (by means of a calcite polarizer followed by a half-wave plate). We exploited the flexibility of the telescopic system to obtain collimated spatial distributions of different widths (specifically, we observe beam widths of 2.2 pixels (px), 3.0 px and 4.0 px of the SPAD array, corresponding to four different interaction strengths $g/\sigma = 0.78, 0.55, 0.42$). We have estimated the quality of our single-photon emission with a Hanbury-Brown and Twiss interferometer [125], obtaining a value for the parameter α [126] (directly connected to the second-order Glauber autocorrelation function $g^{(2)}(0)$) of 0.13 ± 0.01 without any background or dark count subtraction, that being largely below 1 testifies the goodness of our SPS. The interaction steps of the genetic evolution couple quantum degrees of freedom of the single photon exploiting birefringence. In our optical path we can insert up to $K = 7$ birefringent units, each of them composed of two different calcite crystals. Although, theoretically, the probability of losing a photon between subsequent steps due to unsuccessful verification measurement reduces with K, this advantage is diminished due to losses originating from imperfections of the optical elements. The first crystal of each element is a 2 mm thick birefringent crystal whose extraordinary (e) optical axis lies in the X-Z plane, with an angle of 45 ° with respect to

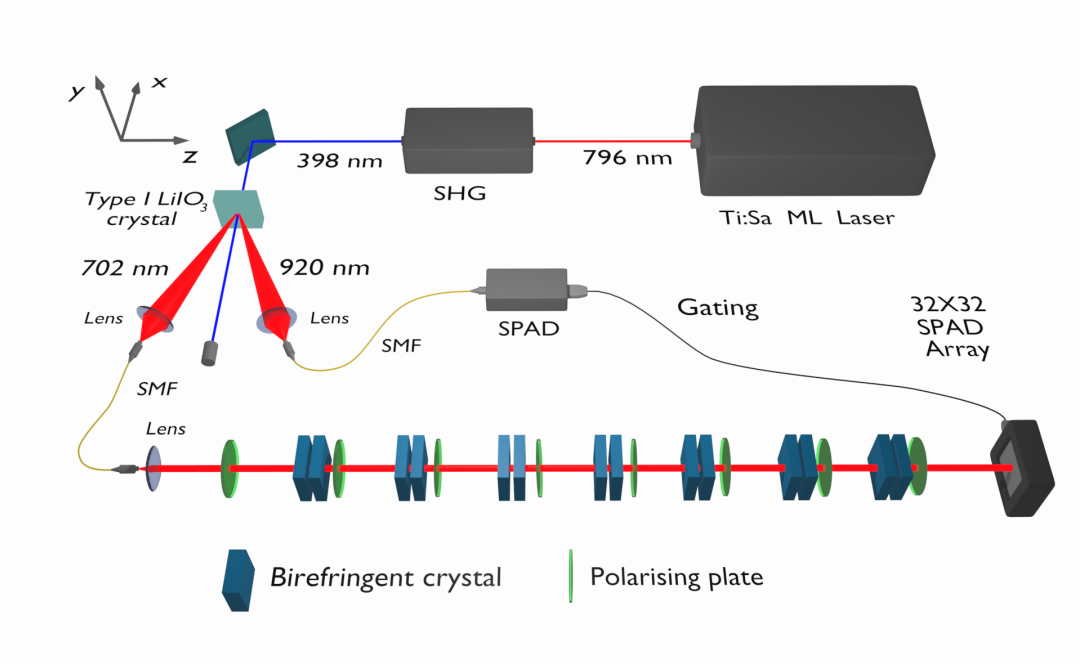

Figure 4.6: GQM experimental setup. Single photons are generated by a type-I PDC heralded source. Then, the initial state is prepared by exploiting a state filtering done through a polarizing plate. Afterward, $K = 7$ GQM steps each realizing the bio-inspired mechanics of mutation, crossover and selection are implemented, each of them hosting a pair of birefringent crystals and a polarizing plate. Finally, single photons are detected by a 32×32 SPAD array detector.

the Z direction. Due to the spatial walk-off effect experienced by the horizontally-polarized photons, horizontal and vertical-polarization paths get slightly separated along the X direction. The second crystal of each unit is a 1.1 mm thick birefringent crystal with the optical (e)-axis along the X direction (thus not contributing to the transversal walk-off) that nullifies, through phase compensation, the temporal walk-off introduced by the first one. The selection of the quantum state is realized by inserting a thin-film polarizer after each birefringent unit, projecting the photons onto the same polarization of the initial state $|\psi_\theta\rangle$. At the end of the optical path, the photons are detected by a spatial-resolving single-photon detector prototype developed by the Polytechnic University of Milan [127]. This device is a two-dimensional array made of 32×32 "smart pixels" - each one hosting a SPAD-based single-photon detector and its front-end electronics. The SPAD array is gated with a 6 ns detection window, triggered by the SPAD in the heralding arm, in order to reduce the dark counts and improve the signal-to-noise ratio.

4.4 Measurement with the 32×32 SPAD-array

As mentioned before, the SPAD array is a prototype. Thus, it has some flawed pixels due to a disruption of the electronics impossible to fix. These pixels register a big amount of false counts with respect to the dark-counts typical values. We called the pixels that register an anomalous amount of dark counts *hot pixels*.

First, by exploiting a continuous-wave ancillary laser at 705 nm (very close to the signal photons wavelength), we placed the SPAD camera in order to be sure that the single

photons spatial-distribution peaks fall in a region as free from hot pixels as possible. Since these pixels can not just be removed, we had to find a method for replacing their counts with proper values. For this reason, we developed an algorithm able to properly replace the hot pixels in post-processing. An example of raw image obtained with the SPAD array is showed in Fig. 4.7. Even at a first glance it is clear that, if we simply removed the hot

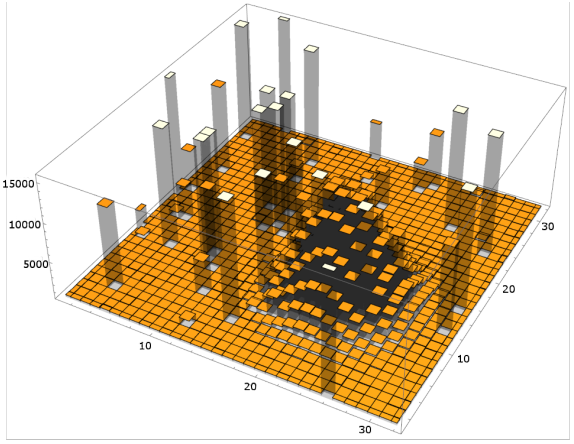

Figure 4.7: Raw detected image of $|V\rangle$-polarized single photons with Gaussian spatial distribution (waist $\sigma = 3.0\,\mathrm{px}$).

pixels, then we would introduce a bias over the average position of the photons (i.e. the peak of the distribution).

Thus, we designed an algorithm that works as explained in the following sentences. It compares each pixel with its nearest neighbors: if its value is higher than a suitably chosen threshold, i.e. the mean value of its neighbor counts multiplied by a factor of 1.6-2 (depending on the acquisition signal-to-noise ratio), then it is identified as a hot pixel, and its value is set to zero. Then, it performs a two-dimensional Gaussian fit over the remaining pixels, in order to replace each pixel previously set to zero with a sensible substitute, not to introduce a bias in the estimation of $\langle x \rangle$.

By running the algorithm for the image in Fig. 4.7, we obtain the following "clean" image (Fig. 4.8).

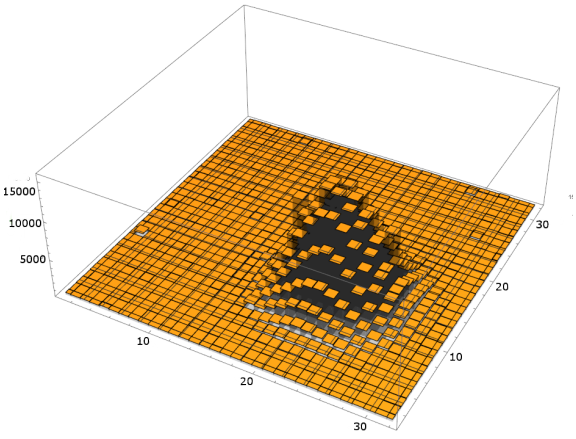

Figure 4.8: Resulting count distribution after running the hot pixels elimination algorithm for the distribution in Fig. 4.7.

4.5 Projective measurement

The aim of the experiment is to demonstrate with an experimental comparison that GQM outperforms projective measurement in terms of uncertainties, starting from the same initial conditions. To do this, it is possible to adapt the setup in Fig. 4.6 for performing both measurement protocols.

As one can see from Fig. 4.1, by removing the polarizing plates realizing the selection inside the GQM steps, a Kg-large spatial separation of the horizontal and vertical polarization components is obtained, as in a Stern-Gerlach experiment. The "modified" setup is schematized in Fig. 4.9.

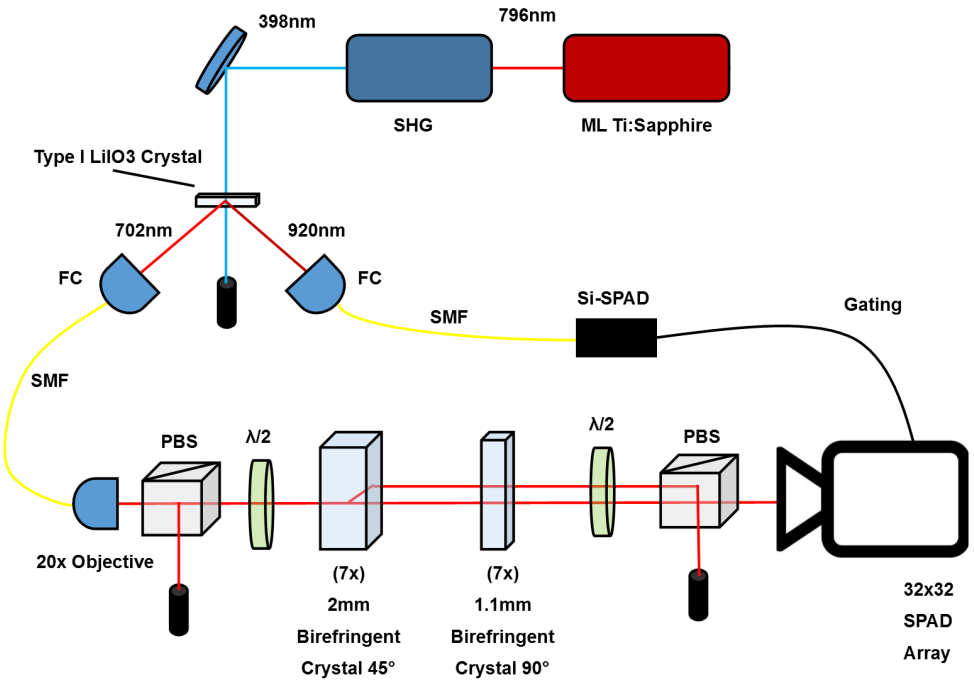

Figure 4.9: Scheme of the adapted setup for projective measurement. The heralded single-photon source and the initial state-filtering preparation are unchanged. After them, the single photons pass through the seven birefringent crystal pairs, each composed of a 2 mm thick birefringent crystal with optical axis inclined of 45° with respect to the photons propagation direction, and a 1.1 mm thick birefringent crystal with optical axis orthogonal to it (for compensating the polarization components temporal walk-off induced together with the spatial displacement by the previous one). Finally, the detection part consists in the combination of a half-wave plate and a PBS. The single photons are detected by the 32×32 same SPAD array prototype used for the GQM realization.

After the initial state-filtering preparation and the interactions with birefringent crystals, the single photons are projected by exploiting a half-wave plate and a PBS, and then they are detected by the SPAD-array. We rescaled the experimental results in order to consider $N_{tot} = M$ measured photons. The initial state $|\psi_\theta\rangle$ can be estimated by:

$$|\psi_\theta\rangle = \cos\theta|H\rangle + \sin\theta|V\rangle = \sqrt{\frac{N_H}{N_{tot}}}|H\rangle + \sqrt{\frac{N_V}{N_{tot}}}|V\rangle \tag{4.15}$$

where the projective measurement are made in the $\{|H\rangle, |V\rangle\}$ basis, and N_H (N_V) is the amount of photons detected after projecting onto $|H\rangle$ ($|V\rangle$) polarization, and $N_{tot} = N_H + N_V$. The expectation value of $P = |H\rangle\langle H| - |V\rangle\langle V|$ is given by:

$$\langle P\rangle = \langle\psi_\theta|P|\psi_\theta\rangle \tag{4.16}$$

and the related uncertainty is defined in Eq. 4.13.

4.6 Measurement operations

In order to identify and eliminate (or at least minimize) eventual systematic uncertainties, we optimized the measurement experimental procedure by following this scheme:

- Setup optimization;
- Spatial calibration of the measurement system;
- Measurement protocols executions;
- Measurement of eventual biases within the optical measurement setup.

These measurement phases will be explained in the paragraphs below. The whole procedure has been repeated for three different initial polarization states $|\psi_{\theta_i}\rangle = \cos\theta_i|H\rangle + \sin\theta_i|V\rangle$, where $i = 1, 2, 3$ and $\theta_1 = \pi/4$, $\theta_2 = \pi/8$, $\theta_3 = 17\pi/60$. For each initial state $|\psi_{\theta_i}\rangle$ we repeated again the measurements with three different spatial-distribution waist σ ($\sigma_1 = 2.2\,\text{px}$, $\sigma_2 = 3.0\,\text{px}$ and $\sigma_3 = 4.0\,\text{px}$), i.e. varying the intensity interaction g/σ into the GQM steps.

4.6.1 Setup optimization

Each birefringent crystal pair in the setup has to be accurately positioned, in order to compensate the temporal walk-off induced by the first crystal. Thus, for each birefringent crystal pair we put the first crystal onto a piezo-electric rotator able to rotate onto the $X-Z$ plane, in order to finely compensate the phase mismatch between the two polarization components. To do this, before any measurement, we set the initial state equal to $|+\rangle = (|H\rangle + |V\rangle)/\sqrt{2}$, and we introduced the crystal pairs one by one.

For each pair, by deviating the photons (normally addressed to the SPAD array) to a fiber coupler connected to a Si-SPAD, we measured the amount of heralded photons projected onto $|+\rangle$ depending on the 45°-birefringent crystal rotation. By rotating the first crystal of the pair over a range of 5° with steps $\Delta\theta = 0.005°$, we choose the position that maximized the visibility of the produced state, defined by:

$$\zeta = \frac{N_{max} - N_{min}}{N_{max} + N_{min}} \tag{4.17}$$

where N_{max} and N_{min} are respectively the interference pattern maximum and minimum.

When the correct position is fixed, it is impossible to remove the crystal pair without compromising the temporal walk-off compensation.

4.6.2 Spatial calibration of the measurement system

With GQM we estimate the expectation value $\langle P \rangle$ of the initial state polarization with the coordinates of the mean position of the detected photons. Therefore, it is required a calibration determining the positions of the vertical and horizontal polarization components on the SPAD array.

After the setup optimization, the configuration is the one shown in Fig. 4.9. Hence, for the calibration we performed two measurements of 300 s: the first one with the prepared initial state $|H\rangle$, the other one for the state $|V\rangle$. For both measurements, we obtained a Gaussian distribution of the detected photons. Then, we analyzed the two spatial distributions obtained, extracting the average $\langle x \rangle$ position for both of them, thus achieving an estimate of the extremes of our OoI eigenvalue spectrum.

4.6.3 Measurement protocols execution

At this point, the experimental setup is still in the configuration shown in Fig. 4.9. For each state-filtering preparation $|\psi_{\theta_i}\rangle$, we performed two 300 s long projective measurements.

To realize the GQM protocol, in this phase we insert the polarizing plates, obtaining the setup configuration shown in Fig. 4.6. For each state-filtering preparation $|\psi_{\theta_i}\rangle$, we performed an acquisition 3000 s long.

4.6.4 Measurement of eventual biases within the optical system

In line of principle, a polarizing plate would not introduce spatial deviations in the single-photon propagation direction. Nonetheless, in practice it could induce a slight displacement on them, and this will generate a bias over the estimated polarization value obtained with the GQM protocol. In order to measure this bias, we removed the birefringent-crystal pairs, and we left the polarizing plates oriented for projecting onto the same state-filtering selection $|\psi_{\theta_i}\rangle$, as during the GQM. Then, we did a 600 s long acquisition, with which we obtained the mean position of the photons $\langle x \rangle_{pol} = x_{pol}$. Finally, we also removed the seven polarizing plates, and we performed again a 600 s long acquisition, obtaining the mean position of the photons spatial distribution without spacial displacements $\langle x \rangle_{free}$.

The induced spacial deviation D_{pol} is given by:

$$D_{pol} = \langle x \rangle_{pol} - \langle x \rangle_{free} \tag{4.18}$$

For GQM, we have to correct the SPAD-array detector calibration with the term D_{pol}, obtaining:

$$\begin{aligned} X_H &= x_H + D_{pol} \\ X_V &= x_V + D_{pol} \end{aligned} \tag{4.19}$$

where x_H and x_V are respectively the horizontal coordinates of $|H\rangle$ and $|V\rangle$ obtained in the previous calibration.

4.7 Data analysis

As previously described, for our comparison between GQM and projective measurement we detected the single photons with the 32×32 SPAD-array, and we elaborated the acquired images with the algorithm explained in section §4.4. In order to extract more precisely the coordinates of the photons spatial distribution average position, for each "clean" image we

selected a squared region of interest (RoI), with side 3σ, where σ is the spatial-distribution waist of the detected photons (expressed in pixels).

Outside of the RoI, we evaluated the noise contribution as the average counts per pixel $\langle N_{noise} \rangle$. Later, we subtracted this value from each pixel inside the RoI, fixing to zero those showing negative values.

4.7.1 Projective measurement

The state $|\psi_\theta\rangle = \cos\theta|H\rangle + \sin\theta|V\rangle$ is defined in Eq. 4.15 as a function of the counts detected in a projective measurement. By using the SPAD array, the amount of detected counts N_X, with $X = H, V$ is given by:

$$N_X = \sum_{(x,y)\in RoI} N_X(x,y) \tag{4.20}$$

where $N_X(x,y)$ is the value of the measured count in the polarization state $|X\rangle$ by the pixel with coordinates (x,y) inside the RoI. The corresponding uncertainties (see Eq. 4.13) have to be multiplied by the survival probability in Eq. 4.8 of the state $|\psi_\theta\rangle$ for $K = 7$ in order to fairly compare the uncertainties between projective measurement and GQM protocols.

In the following figures, we show the single-photon counts acquired by performing the projective measurement. Respectively, the initial polarization states under test are $|\psi_{17\pi/60}\rangle = 0.629|H\rangle + 0.777|V\rangle$ in Fig. 4.10, $|\psi_{\pi/4}\rangle \equiv |+\rangle = (|H\rangle + |V\rangle)/\sqrt{2}$ in Fig. 4.11, and $|\psi_{\pi/8}\rangle = 0.924|H\rangle + 0.383|V\rangle$ in Fig. 4.12. For each initial state, we considered three different Gaussian single-photon spatial distributions with waist $2.2, 3.0$, and 4.0 pixels, thus modifying the induced von Neumann interaction intensity.

Measuring the single photons, we projected at different times onto the polarizations $|H\rangle$ and $|V\rangle$ by means of the half-wave plate and the PBS inserted just before the SPAD array in the setup of Fig. 4.9. This was necessary because the two correspondent count distributions are partially overlapped in the cases of large waist, and we had to assign to each count a precise polarization component in order to extract information about the initial state $|\psi_{\theta_i}\rangle$ (see Eq. 4.15).

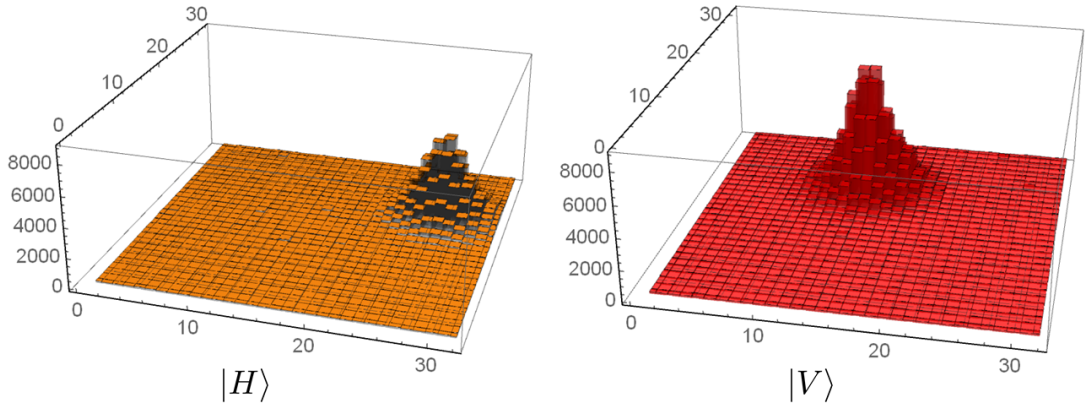

(a) $\sigma = 2.2\,\text{px}$

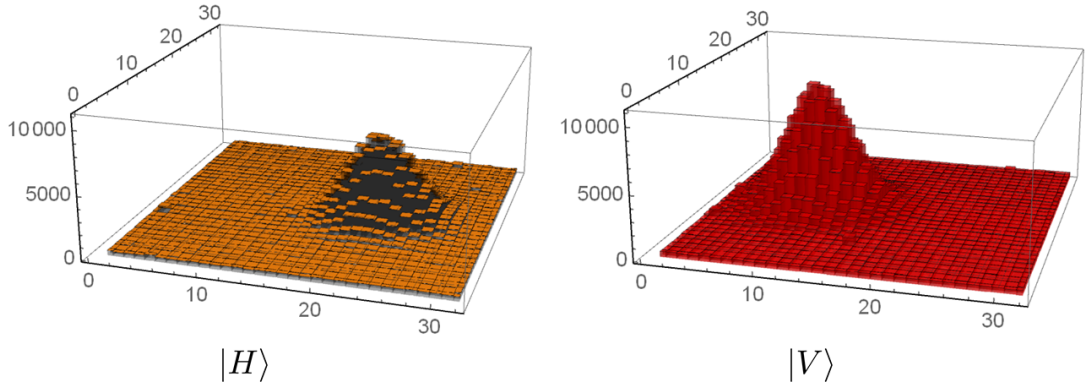

(b) $\sigma = 3.0\,\text{px}$

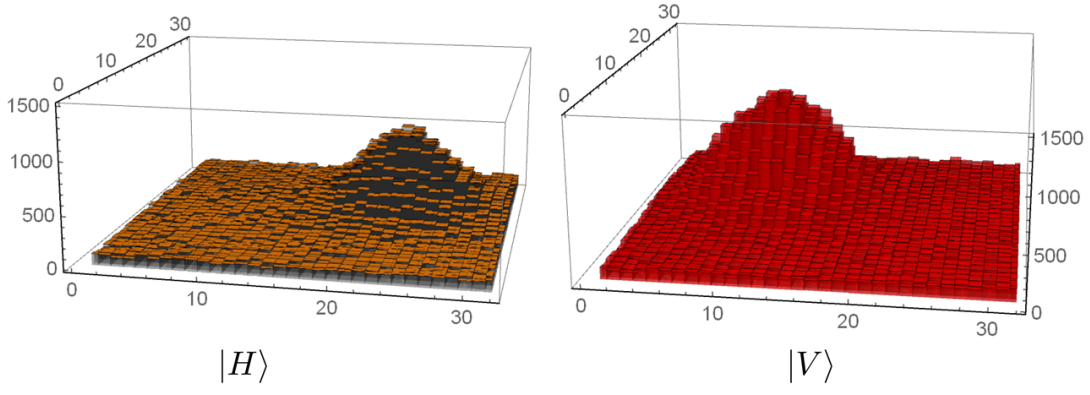

(c) $\sigma = 4.0\,\text{px}$

Figure 4.10: Detected photons with polarization state $|H\rangle$ (yellow) and $|V\rangle$ (red). We performed three projective measurement over the initial state $|\psi_{17\pi/60}\rangle = 0.629|H\rangle + 0.777|V\rangle$, by changing the waist σ of the single photons Gaussian spatial distribution: a) $\sigma = 2.2\,\text{px}$, b) $\sigma = 3.0\,\text{px}$ and c) $\sigma = 4.0\,\text{px}$.

4.7.2 GQM results

As K increases, the survival probability of the single photons (defined in Eq. 4.8) has higher values for the paths next to the one corresponding to the initial polarization state. Therefore, we could expect to observe from the SPAD-array acquisitions a higher collection of counts centered in the position corresponding to the initial polarization $|\psi_\theta\rangle$.

Analogously to the projective measurement protocol, for each acquired image we selected a squared RoI, with side length 3σ. Again, we evaluated from the pixels outside of the RoI the average noise counts per pixel $\langle N_{noise}\rangle$, and we subtracted this value from the RoI pixels with the same procedure illustrated for the projective measurement.

The average position of each measured initial state is given by the average position of the detected photons in function of the counts:

$$\langle X_\psi\rangle = \frac{1}{N_{tot}} \sum_{(x,y)\in RoI} N(x,y) \tag{4.21}$$

where the sum is extended only to the RoI, N_{tot} is the total amount of detected photons and $N(x,y)$ is the number of counts relative to the pixel with coordinates (x,y).

The calculated position $\langle X_\psi\rangle$ stands between the points (X_H) and (X_V); the estimation of $\langle P\rangle$ is given by:

$$\langle P\rangle = \frac{2\langle X_\psi\rangle}{gK} - 1 \tag{4.22}$$

where $gK = \langle X_H\rangle - \langle X_V\rangle$. By remembering Eq. 4.12, in which the uncertainty related to P is defined, the uncertainty associated with the expectation value $\langle P\rangle$ is:

$$u(\langle P\rangle) = \frac{u(P)}{\sqrt{N_{tot}}} \tag{4.23}$$

In the following, we show the images obtained from the GQMs performed on the three states under exam, with different von Neumann interaction intensity g/σ. In particular, Figs. 4.13, 4.14 and 4.15 respectively correspond to the initial states $|\psi_{17\pi/60}\rangle = 0.629|H\rangle + 0.777|V\rangle$, $|\psi_{\pi/4}\rangle = (|H\rangle + |V\rangle)/\sqrt{2}$ and $|\psi_{\pi/8}\rangle = 0.924|H\rangle + 0.383|V\rangle$.

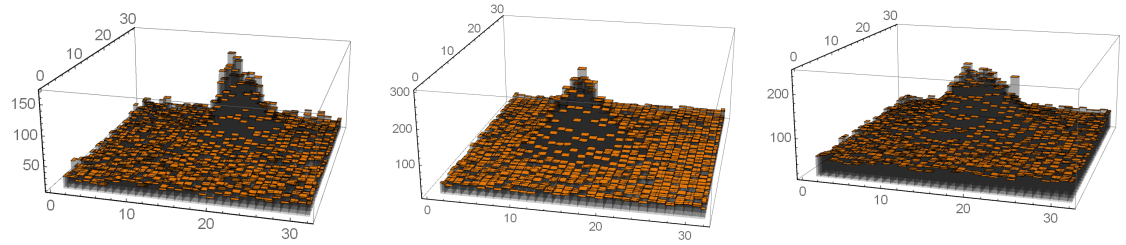

(a) $\sigma = 3.0$ px
$\langle P\rangle = -0.25 \pm 0.02$

(b) $\sigma = 4.1$ px
$\langle P\rangle = -0.14 \pm 0.04$

(c) $\sigma = 5.6$ px
$\langle P\rangle = -0.14 \pm 0.03$

Figure 4.13: GQM results obtained for single photons initially prepared in the polarization state $|\psi_{17\pi/60}\rangle = 0.629|H\rangle + 0.777|V\rangle$, corresponding to the OoI theoretical value $\langle P_{th}\rangle = -0.208$, for three different interaction intensities, achieved by varying the (Gaussian) spatial distribution waist σ.

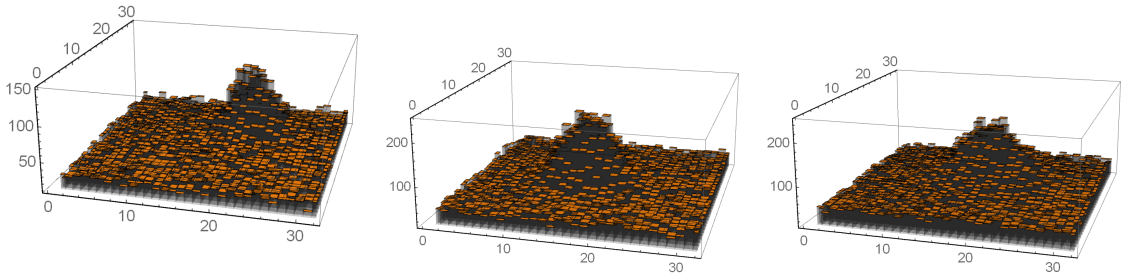

(a) $\sigma = 3.0\,\text{px}$
$\langle P \rangle = -0.005 \pm 0.005$

(b) $\sigma = 4.1\,\text{px}$
$\langle P \rangle = -0.05 \pm 0.03$

(c) $\sigma = 5.6\,\text{px}$
$\langle P \rangle = 0.02 \pm 0.03$

Figure 4.14: GQM results obtained for single photons initially prepared in the polarization state $|\psi_{\pi/4}\rangle = (|H\rangle + |V\rangle)/\sqrt{2}$, corresponding to the OoI theoretical value $\langle P_{th} \rangle = 0$, for three different interaction intensities, achieved by varying the (Gaussian) spatial distribution waist σ.

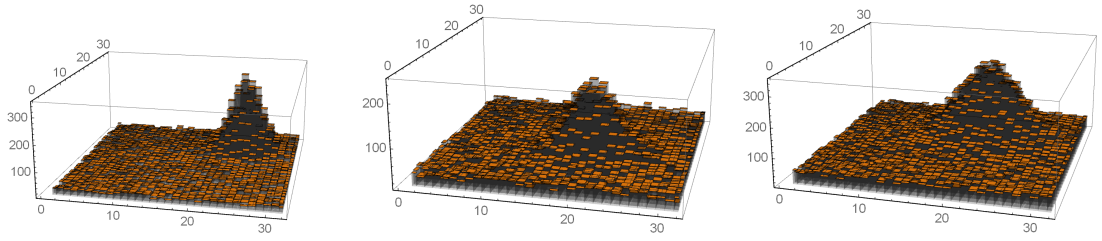

(a) $\sigma = 3.0\,\text{px}$
$\langle P \rangle = 0.709 \pm 0.005$

(b) $\sigma = 4.1\,\text{px}$
$\langle P \rangle = 0.70 \pm 0.09$

(c) $\sigma = 5.6\,\text{px}$
$\langle Pthat \rangle = 0.74 \pm 0.02$

Figure 4.15: GQM results obtained for single photons initially prepared in the polarization state $|\psi_{\pi/8}\rangle = 0.924|H\rangle + 0.383|V\rangle$,corresponding to the OoI theoretical value $\langle P_{th} \rangle = 0.707$, for three different interaction intensities, achieved by varying the (Gaussian) spatial distribution waist σ.

From the experimental results, it emerges that with GQM protocol we obtained the photon counts in a spatial distribution centered on a region whose x coordinate is directly related with the expectation value of the photons initial polarization. Along the X axis, such distribution appears larger than along Y axis, because (see Fig. 4.1) the mutation mechanisms inside the GQM only occur in one direction: in our case the X axis. This asymmetry emerges clearer and clearer as the interaction intensity g/σ increases.

Under each image are reported the corresponding estimated expectation values $\langle P \rangle$, together with their statistical uncertainties, demonstrating how they are in good agreement with the theoretical predictions.

4.7.3 Experimental comparison between GQM and projective measurement

In Fig. 4.16 we show the statistical uncertainties related to the measurements of P.

In these three graphs one can appreciate the comparison between GQM (red) and projective measurement (blue) related uncertainties behavior.

In order to make a fair comparison, one has to take into account that in GQM protocol the single photons have a survival probability due to the selection mechanism. Thus, for

measuring one photon at the end of the protocol, one needs an initial amount of initial photons equal to $P_s(K)^{-1}$, with $P_s(K)$ defined in Eq. 4.8. Therefore, the uncertainty related to the projective measurement is given by Eq. 4.13, where in our case $M = P_s(K)^{-1}$.

In Fig. 4.16 it is possible to notice that $u_{PBS}(P)$ decreases as the interaction intensity g/σ increases, because the survival probability decline entails the increase of the required initial single photons amount.

On the contrary, the GQM uncertainty is defined in Eq. 4.12. We can see that the experimental results are in good agreement with respect the theoretical predictions. In addiction, the GQM uncertainties are always smaller than the ones given by projective measurements, except for the case of $\sigma = 4.0\,\text{px}$ in correspondence with the polarization state $|\psi_{\frac{\pi}{8}}\rangle = 0.924|H\rangle + 0.383|V\rangle$. In that case, the interaction intensities inside the GQM steps are weak, and it is not possible to achieve a sufficient resolution after just $K = 7$ steps.

This is easy to understand by observing the behavior of the ratio R (see Eq. 4.14), that we report again in Fig. 4.17 for $K = 7$, underlining the three sections related to the different polarization states under test.

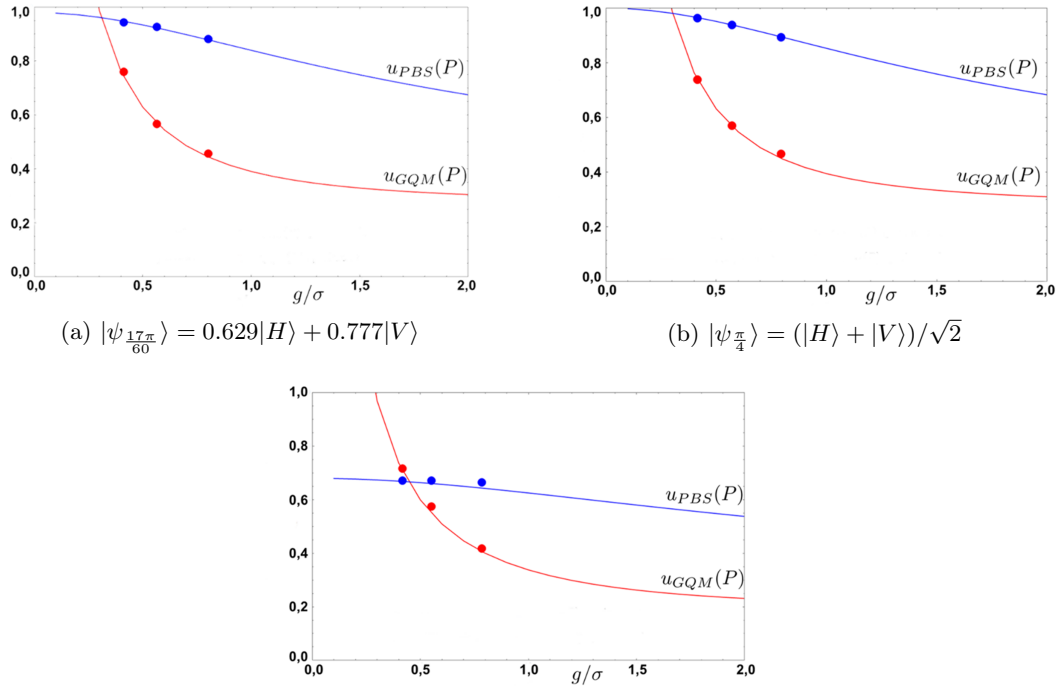

(a) $|\psi_{\frac{17\pi}{60}}\rangle = 0.629|H\rangle + 0.777|V\rangle$

(b) $|\psi_{\frac{\pi}{4}}\rangle = (|H\rangle + |V\rangle)/\sqrt{2}$

(c) $|\psi_{\frac{\pi}{8}}\rangle = 0.924|H\rangle + 0.383|V\rangle$

Figure 4.16: Comparison between statistical uncertainties experimentally obtained from GQM (red) and projective measurement (blue) protocols. For each initial polarization state $|\psi_{\theta_i}\rangle$, the continuous lines represent the theoretical predictions in function of the interaction intensity g/σ, whereas the dots are the obtained experimental values.

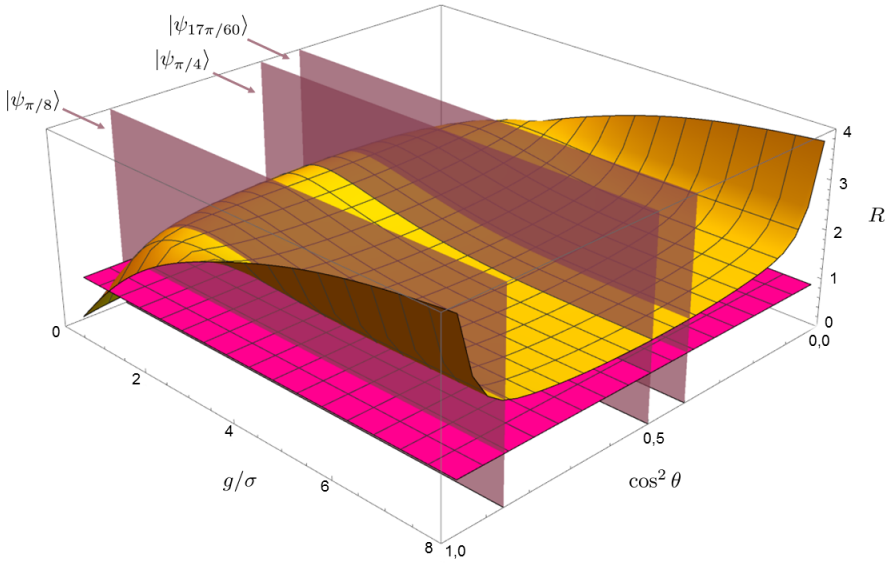

Figure 4.17: Sections (violet) of the R surface for $K = 7$ from Fig. 4.5, n correspondence of the polarization states $|\psi_{\frac{17\pi}{60}}\rangle = 0.629|H\rangle + 0.777|V\rangle$, $|\psi_{\frac{\pi}{4}}\rangle = (|H\rangle + |V\rangle)/\sqrt{2}$ and $|\psi_{\frac{\pi}{8}}\rangle = 0.924|H\rangle + 0.383|V\rangle$. The magenta plane represents $R = 1$: above it GQM is advantageous in terms of uncertainty in comparison to the projective measurement.

In Fig. 4.18 we report the three orthogonal projections of the sections shown in Fig. 4.17. For each state under exam, we also report the experimental values of R. The theoretical behavior of R as a function of the interaction intensity is shown in yellow, whereas the magenta line corresponds to $R = 1$, below which the GQM protocol is not convenient with respect to the traditional projective measurement.

Again, the experimental results are in good agreement with the theoretical predictions. It is remarkable that with just $K = 7$ steps GQM we could achieve a gain of a factor > 2 in terms of precision with respect to projective measurement with the same initial conditions. As mentioned before, the only case in which the GQM was not convenient is the one corresponding to the initial state $|\psi_{\frac{\pi}{8}}\rangle$ for $\sigma = 5.6$. This is due to the von Neumann interaction intensity, that is too weak to efficiently extract information about the OoI P after just $K = 7$ steps, because the induced spatial displacement is too small for granting enough resolution.

Obviously, the above considerations assume an ideal scenario where the only source of losses in the measurement process is represented by the projections responsible for the selection mechanism, without optical losses due to imperfections in the optical elements present in the experimental setup. Unfortunately, in such experimental schemes, the optical losses greatly reduce the advantage discussed so far, but this is a technical limitation that can be, in principle, overcome with technological progress in optics manufacturing. It is important to underline that the advantage of the GQM technique can become absolutely relevant in a less lossy measurement scenario, and that our proof-of-principle experiment and simulations pave the way to the exploitation of the GQM approach, e.g., in atomic or solid state quantum systems, where losses are typically less than the ones experienced in photon-based experiments.

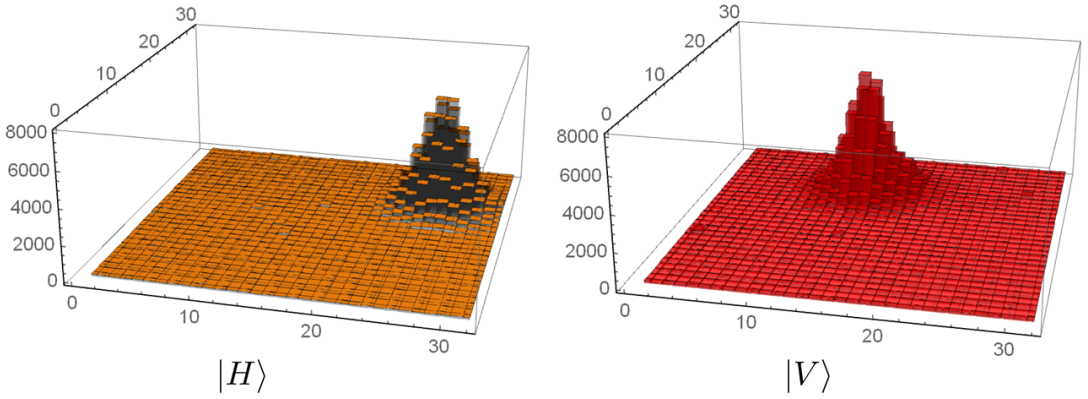

(a) $\sigma = 2.2\,\text{px}$

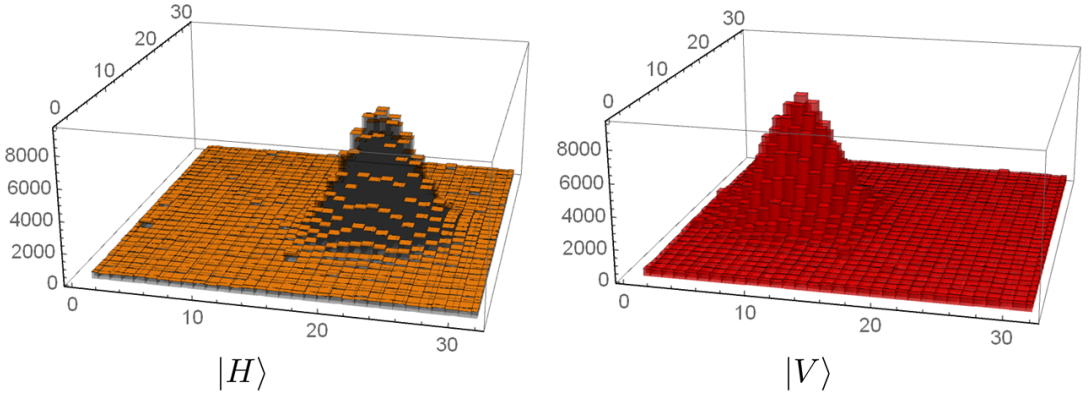

(b) $\sigma = 3.0\,\text{px}$

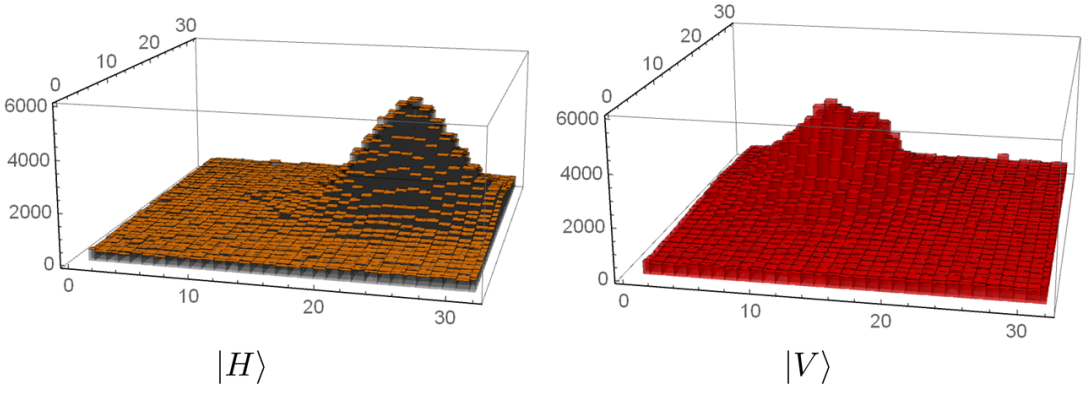

(c) $\sigma = 4.0\,\text{px}$

Figure 4.11: Detected photons with polarization state $|H\rangle$ (yellow) and $|V\rangle$ (red). We performed three projective measurement over the initial state $|\psi_{\pi/4}\rangle = (|H\rangle + |V\rangle)/\sqrt{2}$, by changing the waist σ of the single photons Gaussian spatial distribution: a) $\sigma = 2.2\,\text{px}$, b) $\sigma = 3.0\,\text{px}$ and c) $\sigma = 4.0\,\text{px}$.

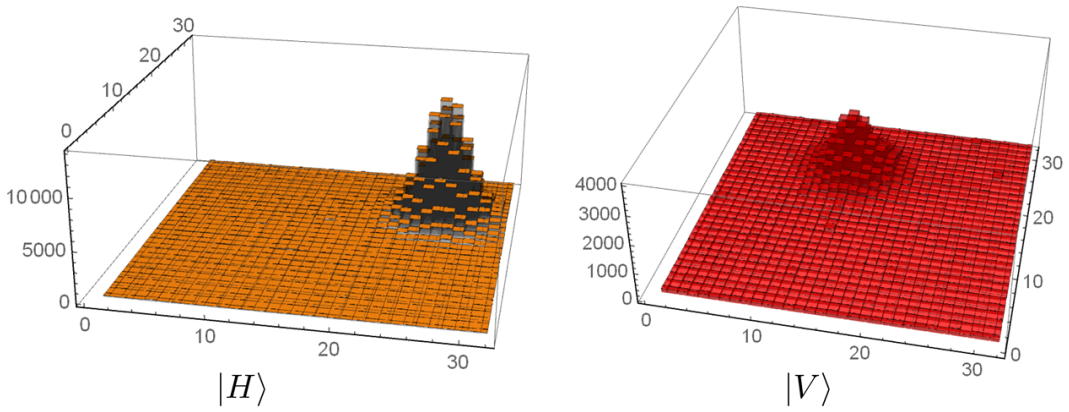

(a) $\sigma = 2.2\,\text{px}$

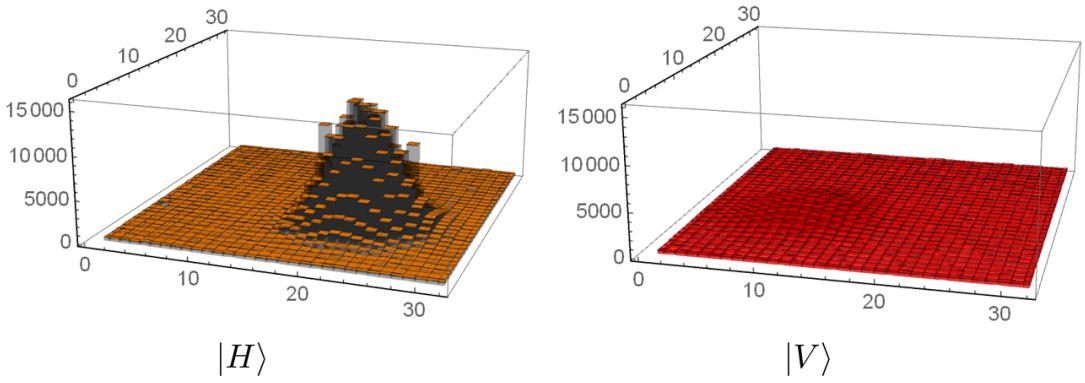

(b) $\sigma = 3.0\,\text{px}$

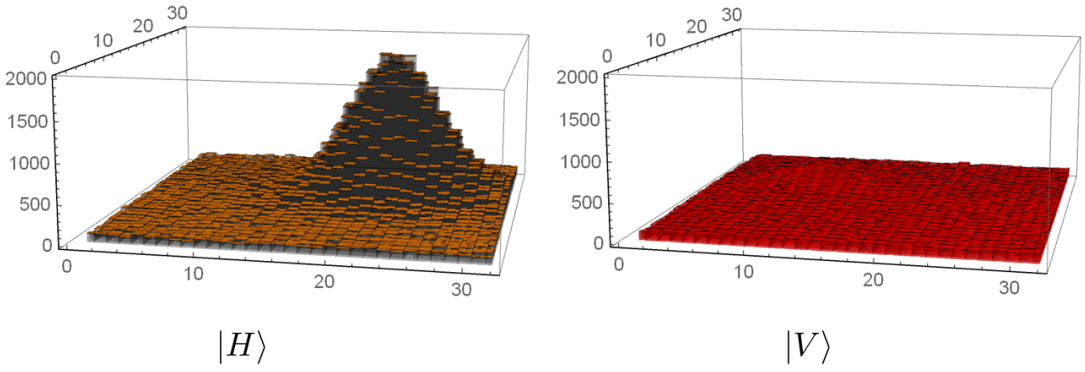

(c) $\sigma = 4.0\,\text{px}$

Figure 4.12: Detected photons with polarization state $|H\rangle$ (yellow) and $|V\rangle$ (red). We performed three projective measurement over the initial state $|\psi_{\pi/8}\rangle = 0.924|H\rangle + 0.383|V\rangle$, by changing the waist σ of the single photons Gaussian spatial distribution: a) $\sigma = 2.2\,\text{px}$, b) $\sigma = 3.0\,\text{px}$ and c) $\sigma = 4.0\,\text{px}$.

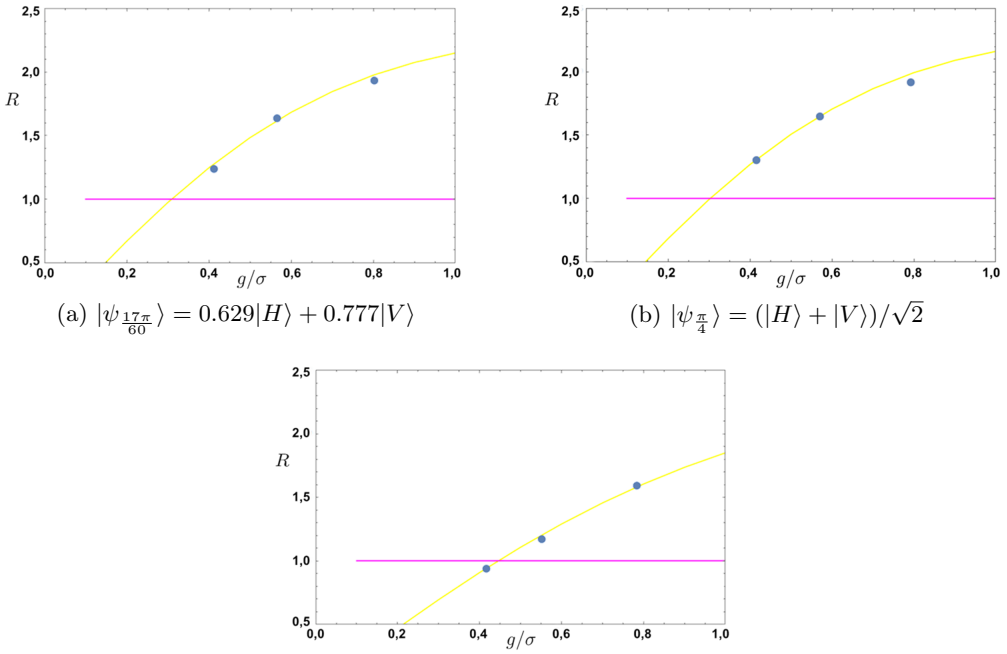

(a) $|\psi_{\frac{17\pi}{60}}\rangle = 0.629|H\rangle + 0.777|V\rangle$

(b) $|\psi_{\frac{\pi}{4}}\rangle = (|H\rangle + |V\rangle)/\sqrt{2}$

(c) $|\psi_{\frac{\pi}{8}}\rangle = 0.924|H\rangle + 0.383|V\rangle$

Figure 4.18: Experimental values (dots) of the ratio R between the obtained projective measurement and GQM statistical uncertainties (Eq. 4.14). For each initial polarization state $|\psi_{\theta_i}\rangle$, the yellow lines is the theoretical prediction (see Fig. 4.5), whereas the magenta line represents the threshold above which the GQM is convenient with respect to the traditional projective measurement in terms of uncertainty.

Chapter 5

Temporal and spatial correlations on an equal footing: the Pseudo-Density Operator

Since Bell's work [23, 128], the study of quantum correlations have been playing a crucial role in quantum foundations investigation. Most of the research works in this field involve spatial correlations, in the form of entanglement and quantum discord [5,55,62,129] (as mentioned in Chapter 3), but different attempts have been made to extend these efforts to the time domain.

Considering its traditional formalism, QM presents a fundamental asymmetry between space and time. This becomes evident when looking at the description of composite quantum systems, whose density matrix, at a given time t, acts on the tensor product of the Hilbert spaces associated with the single subsystems composing the global state, each considered at the same time instant t.

States are defined at a specific instant, and they evolve over time under the action of a Hamiltonian. However, there exists another kind of composite systems besides these, where the components might present both spatial and temporal correlations (even being time-like separated, eventually). In this case, there is no standard prescription for the joint state of such a composite system.

With relativity theory, it has been demonstrated that many distinctions between space and time previously considered to be fundamental are not [130]. Obviously, this argument goes beyond the aim of this thesis. Anyway, it is easy to understand that, in order to achieve a theory that unifies QM and relativity, the research of a quantum formalism treating on an equal footing space-like and time-like correlations is of the utmost relevance for the scientific community.

The space/time asymmetry in QM is also in sharp contrast with classical probability theory, where joint probabilities can be defined for sets of events whatever their spatio-temporal relationships. Hence, although there is a well-developed analogy between density matrices and classical probability distributions, such analogy is limited to time-like separated systems.

If such asymmetry in QM is fundamental, then the understanding of time given by quantum theory must be different from that suggested by a combination of relativity and classical probability theory. If, on the other hand, this is not the case, then this asymmetry should be removable. One way of eliminating it would be to construct quantum states for composite systems over time. States would then be defined across both space and time, without a separate formalism describing temporal evolution.

The most celebrated attempt for formalizing quantum correlations in the time domain is the one from Leggett and Garg, who demonstrated that quantum systems present temporal correlations which cannot be explained by any macro-realistic theory [131].

In recent years, some works have exploited a different approach: to assume QM *a priori*, and then examine the correlations which can arise, e.g., when studying the role of causality in quantum systems [132–134]. Quantum states which violate the Leggett–Garg inequality necessarily manifest these causal correlations: for this reason, recent experimental demonstrations of violations of such inequalities might be seen as a limited observation of such causal correlations [135–139]. In non-relativistic QM, at a given time the state of a physical system is described by the density operator, and it evolves according to Schrödinger's equation; this means that time represent just a parameter, and not an observable of the system. In a recent work [130], it was investigated the possibility of defining joint states over time in a manner that closely matches the standard quantum treatment of composite systems at a given time. The authors showed that, if one fixes a family of operators for describing such states, it is required a product operation, namely a "star" product $\star$, that satisfies five criteria:

- Hermiticity. If the system is defined at two instants t_A and t_B into the Hilbert space $\mathcal{H}_{\mathcal{AB}}$, the star product has to be a map of the form $\star : \mathcal{H}_{\mathcal{AB}} \times \mathcal{H}_{\mathcal{AB}} \to \mathcal{H}_{\mathcal{AB}}$;
- Preservation of probabilistic mixtures. The output state of a quantum evolution for a given input state must be a linear function of both the input state and the evolutionary operator;
- Preservation of classical limit. If a state ρ_A described at time t_A undergoes an evolution at time t_B by the operator E, and the emerging state $E_{B|A}$ commutes with ρ_A, then the star product must satisfy the relation $E_{B|A} \star \rho_A = E_{B|A}\rho_A$;
- Preservation of marginal states. Given the state $\rho_{AB} = E_{B|A} \star \rho_A$, the marginal states of ρ_{AB} have to be obtained by partially tracing over the remaining subsystem.
- Compositionality and associativity. If the system ρ_A at time t_A evolves in $E_{B|A}$ at time t_B, and then it evolves in the state $E_{C|B}$ at time t_C, then the star product has to satisfy that the overall state $\rho_{ABC} = E_{C|B} \star (E_{B|A} \star \rho_A) = (E_{C|B} \star E_{B|A}) \star \rho_A$.

However, they proved with a theorem that there is no way to construct a state over time that satisfies all of these criteria. Nevertheless, if Hermiticity is retained, but the assumption of associativity is dropped, they showed that there exists a formalism that satisfies the remaining criteria: the *pseudo-density operator* (PDO) formalism [140]. This formalism was introduced as an extension of the density operator able to describe spatial and temporal correlations at once, thus representing a new significant tool for describing quantum evolution and measurement in different scenarios. As paradigmatic examples of the PDO formalism application, here I present two works exploiting it to describe two scenarios that the traditional density operator formalism fails to describe in the proper way, since both temporal and spatial correlations are involved and impossible to treat separately. These two scenarios are, respectively, the physics of an entangled pair entering an open time-like curve (OTC) [141], and the black hole information loss paradox [142]. In particular, we perform for the first time an experimental reconstruction of a three-photon state PDO [143, 144] equivalent to the one describing the scenarios mentioned above, also showing how the entanglement monogamy [145,146] violation paradox, arising when modelling these two cases with a density operator, is naturally reconciled by the PDO formalism, in which such violation might appear without giving up on quantum mechanical

states linear evolution. Before going in the details of these works, in the next section the PDO general properties are illustrated.

5.1 Pseudo-density operator

The density operator ρ of a quantum state can be defined as a probability distribution over pure states: $\rho = \sum_i p_i |\psi_i\rangle\langle\psi_i|$, where p_i is the probability associated with the state $|\psi_i\rangle$. Since the Pauli operators, together with the identity, constitute a basis for the spaces of Hermitian operators [5], and any density matrix ρ is Hermitian, one can write the density operator of a generic n-particle multi-partite state as $\rho = a_0\mathbb{1} + \sum_{i=1}^{4^n-1} a_i \hat{S}_i$, where $\hat{S}_i$ is the i-th Pauli operator, and $\{a_i\}_{i=0}^{4^n-1}$ are real numbers. In particular, $a_0 = 1/2^n$, because the Pauli operators are traceless and ρ must have its trace equal to 1. Hence, the expectation value for the Pauli operator $\hat{S}_j$ is given by:

$$\langle \hat{S}_j \rangle = \mathrm{Tr}\left[\hat{S}_j \left(\frac{\mathbb{1}}{2^n} + \sum_{i=1}^{4^n-1} a_i \hat{S}_i\right)\right] = 2^n a_j \tag{5.1}$$

Thus, it is possible to alternatively define ρ as a function of the expectation value of Pauli operators:

$$\rho = \frac{\mathbb{1}}{2^n} + \sum_{i=1}^{4^n-1} \frac{\langle \hat{S}_i \rangle}{2^n} \hat{S}_i \tag{5.2}$$

In order to make the state correlations emerge, one can express each Pauli operator as the tensorial product of n 2×2 Pauli matrices, yielding:

$$\rho = \frac{1}{2^n} \sum_{i_1=0}^{3} \cdots \sum_{i_n=0}^{3} \left\langle \bigotimes_{j=1}^{n} \sigma_{i_j} \right\rangle \left(\bigotimes_{j=1}^{n} \sigma_{i_j} \right) \tag{5.3}$$

where $\sigma_0 = \mathbb{1}$, $\sigma_1 = X$, $\sigma_2 = Y$ and $\sigma_3 = Z$.

Eq. 5.3 can be interpreted as a generalized definition of the density operator. By considering a set of events $\{E_1, \ldots, E_N\}$, where for each event a von Neumann measurement [27] of a single Pauli matrix can be performed, for a particular choice of Pauli operators $\{\sigma_{i_j}\}_{j=1}^{n}$ the corresponding expectation value is indicated with $\langle \{\sigma_{i_j}\}_{j+1}^{n} \rangle$. Then, one can define a PDO as:

$$\mathcal{R} = \frac{1}{2^n} \sum_{i_1=0}^{3} \cdots \sum_{i_n=0}^{3} \langle \{\sigma_{i_j}\}_{j=1}^{n} \rangle \left(\bigotimes_{j=1}^{n} \sigma_{i_j} \right) \tag{5.4}$$

In order to compute $\mathcal{R}$, according with Eq. 5.4 only the expectation values for possible measurements are required.

By definition, the PDO can be non-positive, i.e. it can present negative eigenvalues. When this occurs, it means that the PDO necessarily contains a temporal correlation element [147], allowing partial discrimination between spatial and temporal correlations (since PDOs can be positive without implying space-like separation [140], the absence of a negative eigenvalue is not enough to exclude temporal correlations).

In what follows, I will assume that the dynamics between measurement events are in accordance with non-relativistic QM, and that the action of each measurement is to project the state onto the eigenspace of the measurement operator corresponding to the measurement result. If one assumes that the underlying dynamics are non-relativistic, in general

the resulting PDO is not Lorentz-covariant. However, the definition of the PDO in Eq. 5.4 does not imply a specific dynamics model. Therefore, a PDO can be reconstructed from experimental results or derived from theoretical predictions without implicitly assuming non-relativistic QM. If the measurement events $\{E_1, \ldots, E_N\}$ correspond to simultaneous measurements of different subsystems of a n-partite quantum state, or in the eventuality that these measurements occur on states which are non-interacting between measurement events, then $\mathcal{R}$ corresponds to a "traditional" density operator.

The PDO inherits many of the properties of a density operator, as we will show in the following.

Hermiticity

All PDOs are necessarily Hermitian operators.
Proof: by definition, a PDO is a weighted sum over Pauli matrices. As Pauli matrices are Hermitian and all weights are real, the resulting PDO is Hermitian by construction.

Unit trace

All PDOs have trace equal to 1.
Proof: this property follows from definition of the PDO in Eq. 5.4, because other than the identity, all the Pauli matrices are traceless. Hence, when taking the trace of a PDO, only the weight for the identity term contributes. Then:

$$\mathrm{Tr}\left[\mathcal{R}\right] = \mathrm{Tr}\left[\frac{\langle \mathbb{1}, \ldots, \mathbb{1}\rangle}{2^n}\mathbb{1}\right] = 1 \tag{5.5}$$

Partial trace

Given a bipartite state PDO $\mathcal{R}_{AB}$ defined over two sets of events A and B, the "reduced" PDO obtained from the set A can be derived from $\mathcal{R}_{AB}$ by partially tracing with respect to the subsystem B.
Proof: from the PDO definition one has:

$$\mathcal{R}_A = \frac{1}{D_A}\sum_{\sigma_A}\langle\sigma_A\rangle\sigma_A \tag{5.6}$$

where D_A is the dimension of the subsystem corresponding to A.

Instead, $\mathcal{R}_{AB}$ is given by:

$$\mathcal{R}_{AB} = \frac{1}{D_A D_B}\sum_{\sigma_A}\sum_{\sigma_B}\langle\{\sigma_A, \sigma_B\}\rangle\sigma_A \otimes \sigma_B \tag{5.7}$$

where, analogously to Eq. 5.6, D_B is the dimension of the subsystem corresponding to B.

By partially tracing $\mathcal{R}_{AB}$ in Eq. 5.7 with respect to B, one obtains:

$$\begin{aligned}\mathrm{Tr}_B\left[\mathcal{R}_{AB}\right] &= \mathrm{Tr}_B\left[\frac{1}{D_A D_B}\sum_{\sigma_A}\sum_{\sigma_B}\langle\{\sigma_A, \sigma_B\}\rangle\sigma_A \otimes \sigma_B\right] \\ &= \frac{1}{D_A D_B}\sum_{\sigma_A}\sum_{\sigma_B}\mathrm{Tr}\left[\sigma_B\right]\langle\{\sigma_A, \sigma_B\}\rangle\sigma_A \\ &= \frac{1}{D_A}\sum_{\sigma_A}\langle\{\sigma_A, \mathbb{1}\}\rangle\sigma_A = \mathcal{R}_A\end{aligned} \tag{5.8}$$

Measurements

The PDO $\mathcal{R}$ contains information not only about Pauli measurements, but also about the expectation value of the product of any set of local measurements with eigenvalues restricted to ± 1. For a set of measurement operators $\{M_j\}$, with eigenvalues chosen from $\{-1; 1\}$, the expectation value for the product of their outcomes is given by:

$$\langle \{M_j\}_{j=1}^{T} \rangle = \mathrm{Tr}\left[\left(\bigotimes_{j=1}^{T} M_j \right) \mathcal{R} \right] \tag{5.9}$$

where M_j is defined over the set of m_j subsystems on which measurement events occur at time j.

Proof: it is sufficient to show that the expectation values related to the M_j measurements are just a linear combination of those given by Pauli operators measurements. Considering $M_j = \sum_k \alpha_{jk} \sigma_k^{m_j}$, where m_j denotes that the Pauli operator is related to m_j-th subsystem, the expectation value follows from Eq. 5.9 by substitution:

$$\langle \{M_j\}_{j=1}^{T} \rangle = \sum_{i_1=0}^{4^{m_1}-1} \cdots \sum_{i_T=0}^{4^{m_T}-1} \left(\prod_{j=1}^{T} \alpha_{jk} \right) \langle \{\sigma_{i_j}^{m_j}\}_{j=1}^{T} \rangle \tag{5.10}$$

In general, $\langle \{M_j\}_{j=1}^{T} \rangle = \sum_i p_i o_i$, where p_i is the probability of obtaining a product of measurement outcomes equal to o_i. For non-relativistic quantum systems, the probability p_i can be expressed as:

$$p_i = \sum_{s:\prod_j s_j = o_i} \mathrm{Tr}\left[P_T^{s_T} U_{T-1} \dots P_1^{s_1} \rho P_1^{s_1 \dagger} \dots U_{T-1}^{\dagger} P_T^{s_T \dagger} \right] \tag{5.11}$$

where $P_j^{s_j}$ represents the projector onto eigenspace of M_j corresponding to the eigenvalue s_j, and the dynamics between subsequent measurements is described by the unitary operators U_j.

If the eigenvalues spectrum of M_j has no constraints, then $P_j^{s_j}$ can be a high degree polynomial in M_j, whereas in the case of M_j eigenvalues belonging to the set $\{-1; 1\}$ the projector $P_j^{\pm 1}$ can be written as $P_j^{\pm 1} = (\mathbb{1} \pm M_j)/2$. Therefore, for each measurement operator there exist two probabilities, p_1 and p_{-1}. Furthermore, since $\langle \{M_j\}_{j=1}^{T} \rangle = p_1 - p_{-1}$ the quadratic and constant terms cancel, leaving the purely linear expression in Eq. 5.10.

Thus, there are no differences in method for calculating a measurement expectation value with a PDO with respect to a density operator, provided that the measurement operator has eigenvalues ± 1.

This demonstrates that the PDO carries more than simple correlations between Pauli measurements. It also contains the necessary information to predict measurement outcomes for a wide range of measurements, without any further knowledge of the underlying dynamics giving rise to a particular PDO, other than the non-relativistic assumption. Furthermore, this shows that the information captured by the PDO is invariant under local change of basis.

Let me introduce an example, in order to understand what PDO means physically. Consider the statistics of a physical process where a single qubit [5], initially in a maximally-mixed state, is measured at two different times t_1 and t_2. As specified before, each measurement is considered to be performed in any of the three complementary bases X, Y, Z, represented by the Pauli matrices. According to Eq. 5.7, in this case the PDO takes the form:

$$\mathcal{R}_{12} = \frac{1}{4}(\mathbb{1}_{12} + X_1 X_2 + Y_1 Y_2 + Z_1 Z_2) \tag{5.12}$$

where the subscripts 1 and 2 represent, respectively, the time instants t_1 and t_2, and $\mathbb{1}_{12}$ is the identity matrix within the Hilbert space of the two-qubit state. The PDO in Eq. 5.12 has similarities with the density operator of a singlet state, but here all the correlations have a positive sign, whereas for the singlet $\langle XX\rangle = \langle YY\rangle = \langle ZZ\rangle = -1$. It is easy to notice that $\mathcal{R}_{12}$ is not-positive, i.e. at least one of its eigenvalues is negative.

Interestingly, if one traces out one of the two subscripts from the Eq. 5.12, the obtained marginal is a "valid" density matrix, corresponding to the maximally-mixed state $\mathbb{1}/2$. Therefore, the marginals of $\mathcal{R}_{12}$ are both perfectly allowed physical states, whereas the overall state is not.

Anyway, experimentally it is impossible to realize directly a *negative* projection (i.e. a projection onto the state corresponding to a negative eigenvalue), because it would involve negative probabilities [147]. Thus, we designed and implemented in an on-purpose quantum optical setup a novel tomographic technique able to reconstruct PDOs, described in the next section together with the first scenario that we considered, i.e. the simulation of the dynamics of an entangled pair entering an open time-like curve.

5.2 Open time-like curve scenario simulation and PDO tomographic reconstruction

QM and general relativity each provide well-verified predictions, in their respective domains. However, they also provide predictions that cannot be experimentally investigated yet, but nevertheless give the opportunity of examining a rather different physics with respect to the one we directly perceive at our scales, e.g. the physics of black holes [148]. Furthermore, there are other interesting predictions regarding space-time correlations violating the standard properties of QM, such as superpositions of different space-time geometries in quantum gravity, resulting in superposing different causal orders [132].

In these cases, one might relax some of QM assumptions in order to maintain a coherent picture which leads to proposals for new frameworks going beyond quantum theory. An important example of such violations is the dynamics of a quantum system near closed time-like curves (CTCs) [149], allowed solutions of Einstein's equations constituting a model for time travel. CTCs allow observers to travel backwards in time and, possibly, even to interact with their former selves. Obviously, this kind of solutions has been argued to be unphysical in classical general relativity, because paradoxes could arise, e.g. the grandfather's paradox [150, 151]. Some researchers even invoke a chronology-protection principle to rule out their existence in physical reality [152].

A possible resolution for these paradoxes is given by merging general relativity with QM, by considering the dynamics of a quantum system (e.g. a qubit) going back in time through a CTC and interacting with its past copy, as in [149].
Here, the author demonstrates how these paradoxes, arising from chronology-violating solutions of Einstein equations in general relativity, can be translated in computational language by identifying the CTC space-time with an informational network including an interaction gate with a negative delay; then, by extending these models to a quantum mechanical framework, the reconciliation of those paradoxes becomes possible. Specifically, the scheme for such a CTC-involving quantum network is reported in Fig. 5.1. The chronology-respecting qubits and the ones entering the CTC (hosting the negative time delay $-\mathrm{T}$) are represented, respectively, by the density operators ρ_{CR} and ρ_{CTC}. The joint state $\rho_{\mathrm{CR}} \otimes \rho_{\mathrm{CTC}}$ undergoes evolution, mediated by the unitary operator U, by means of the quantum gate G. Then, the global state outgoing the quantum gate G can be written

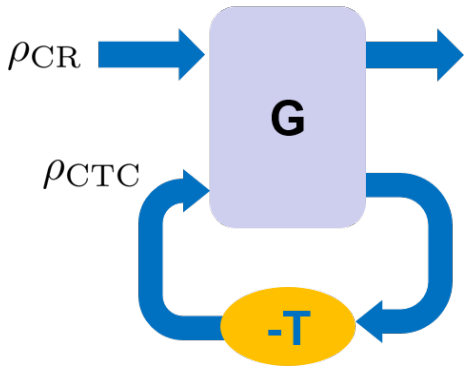

Figure 5.1: Scheme of a CTC quantum network. The density operator ρ_{CR} indicates the state of the chronology-respecting qubits, while ρ_{CTC} the state of the ones entering the CTC (indicated by the negative time delay $-$T). The quantum gate G, instead, is responsible for the unitary evolution U on the joint state Hilbert space.

as:

$$\rho_G = U\left(\rho_{CR} \otimes \rho_{CTC}\right) U^\dagger \tag{5.13}$$

From this, one can find the consistency conditions for this kind of time-travel, by imposing:

$$\rho_{CTC} = \mathrm{Tr}_{CR}\left[U\left(\rho_{CR} \otimes \rho_{CTC}\right) U^\dagger\right] \tag{5.14}$$

It can be shown that Eq. 5.14 admits solutions for every density operator ρ_{CR}, without any further constraint on the chronology-respecting qubits state (in contrast to what happens in the classical scenario, in which an eventual CTC-involving quantum network would be mathematically consistent only with a strict constraint on the chronology-respecting particle).
In the last years, a number of works investigated this scenario [153–157]. However, even if it seems that these paradoxes can be reconciled in this way, the cost of the proposed approach is that the resulting dynamical evolution of each of the involved qubit copies is non-linear [149]. This causes significant changes to the usual QM formalism. Because of non-linearity, CTCs can be used to perform perfect discrimination of non-orthogonal states and other tasks forbidden in traditional QM [158], e.g. quantum cloning [159, 160]. Experimentally, this kind of non-linear evolution has also been simulated, by means of a quantum-optical setup reproducing the dynamics of a qubit entering a CTC [155].

If we have no interaction between the earlier and the later copies of the involved quantum state, instead of a CTC we have a time-travel scenario called open time-like curve (OTC). Interestingly, although paradoxes like the grandfather's one are avoided in OTCs, violations of entanglement basic properties (e.g. the entanglement monogamy principle) can occur if the quantum system entering the OTC is initially entangled with another (chronology-respecting) system [158, 161]. Within the traditional QM formalism, the usual monogamy-preserving approach to an OTC is assuming that the resulting dynamics on the subsystems in the OTC regions violates unitarity by being entanglement breaking.

5.2.1 PDO formalism and entanglement monogamy principle

As an emblematic example of the use of PDO, we considered the case of application to OTC, realizing also an experimental simulation of the relative PDO [143]. In particular, this approach allows one to describe the overall state of the chronology-violating region,

even allowing violations of the monogamy of entanglement under specific circumstances, i.e. when temporal correlations are involved. Furthermore, with this approach linearity is preserved, because PDOs are related by linear transformations. This opens a new line of investigation in which, alternatively to modify the linearity of quantum theory we, modify other properties, specifically the positivity of the quantum state in agreement with the PDO formalism, to accommodate features induced by other physical requirements (in this case general relativity).

In particular, we considered the scenario schematically shown in Fig. 5.2: a qubit (Q2), initially maximally entangled with a second qubit (Q1), enters an OTC, from which its future copy (Q3) emerges from. Although in the remote past and in the distant future we can find only two spatially-correlated qubits (Q1-Q2 and Q1-Q3, respectively), and therefore the density operator could perfectly describe their state, the PDO formalism is needed in the chronology-violating region in which all of the three qubits are present.

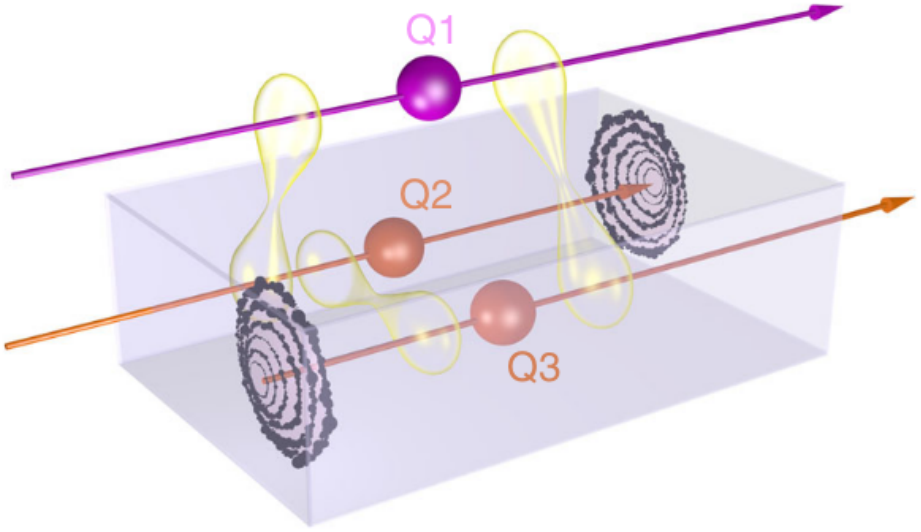

Figure 5.2: Pictorial representation of an OTC circuit. Initially, the qubits Q1 and Q2 are maximally entangled. Then, Q2 enters a chronology-violating region, emerging as a qubit Q3. In the chronology-violating region (shaded volume) in which the three qubits are present, qubits Q1 and Q2 must maintain the maximum entanglement, and the same holds for qubits Q1 and Q3 (being Q3 just a copy of Q2). Within the traditional QM formalism, this situation violates the entanglement monogamy principle, forbidding a quantum system to be maximally-entangled with more than another quantum system.

The corresponding PDO fully describes the three-qubit system even within the OTC chronology-violating region, and also encapsulates the entanglement monogamy violation within it. Here, we conjecture that the PDO $\mathcal{R}_{23}$ of the same form as in Eq. 5.12 describes the state formed by the qubit entering the OTC (Q2) and by its copy emerging from it (Q3), because the two qubits are then perfectly correlated in all bases. More in detail, a maximally-entangled qubit pair (Q1-Q2) is created in the distant past of the region of space-time that contains the OTC. Then, Q2 is sent into the OTC, and its copy emerging from it is represented by a third qubit (Q3). Both in the distant past and in the distant future, the system state corresponds to a maximally-entangled pair, described by the PDO:

$$\mathcal{R}_{1j} = \frac{1}{4}(\mathbb{1}_{1j} - X_1X_j - Y_1Y_j - Z_1Z_j) \qquad j = 2, 3. \tag{5.15}$$

However, in the chronology-violating region we exploit a PDO $\mathcal{R}_{123}$ for modelling the whole state, thus describing the fact that Q1 has to be maximally-entangled both with the qubit emerging from the OTC (Q3) and with the one entering it (Q2) (see Fig. 5.2). Thus, the two marginal PDOs $\mathcal{R}_{12}$ and $\mathcal{R}_{13}$ must correspond to two density operators of the form of Eq. 5.15, because they both represent a maximally-entangled pair, whereas the marginal $\mathcal{R}_{23}$ is a PDO (not a physical state) describing perfect correlation in time between the past and the future copy of the same qubit. The whole descriptor $\mathcal{R}_{123}$ is also not a physical state (i.e. it presents negative eigenvalues), and it can be written as:

$$\mathcal{R}_{123} = \frac{1}{8}(\mathbb{1}_{123} - \Sigma_{12} + \Sigma_{23} - \Sigma_{13}) \tag{5.16}$$

where $\Sigma_{ij} = X_iX_j\mathbb{1}_k + Y_iY_j\mathbb{1}_k + Z_iZ_j\mathbb{1}_k$ and $\mathbb{1}_k$ is the identity in the k-th qubit Hilbert space.

By partially tracing $\mathcal{R}_{123}$ in Eq. 5.16 with respect to one of the subsystems, one can obtain the following marginals:

$$\mathcal{R}_{12} = \frac{1}{4}(\mathbb{1}_{12} - \Sigma_{12})$$

$$\mathcal{R}_{23} = \frac{1}{4}(\mathbb{1}_{23} + \Sigma_{23}) \tag{5.17}$$

$$\mathcal{R}_{13} = \frac{1}{4}(\mathbb{1}_{13} - \Sigma_{13})$$

As described before, the qubits Q1 and Q2 are prepared in a maximally-entangled state, but also Q1 and Q3 are maximally entangled, being qubit Q3 the copy of Q2 that entered the OTC. Furthermore, Q2 and Q3 are maximally correlated in all bases, because they describe the later and earlier qubits in the chronology-violating region (i.e. they are described by a PDO, which is not a physical state). The whole PDO $\mathcal{R}_{123}$ represents a state in which three qubits are maximally anti-correlated in every basis, which is, again, an unphysical state.

It is important to notice that the qubit entering an OTC could undergo some unitary transformation. This transformation would not change its being maximally entangled with the other qubit, so it could be incorporated in the description above by modifying the reduced state of Q1 and Q2 and of Q2 and Q3 to be different maximally entangled states. However, it still remains true that the qubit just before entering the OTC (Q2) and just after emerging from it (Q3) are two copies of the same qubit, which is why they can be described by $\mathcal{R}_{23}$.

In this scenario, for measuring a violation of the entanglement monogamy principle, a simple way is to exploit the marginals $\mathcal{R}_{ij}$ for verifying the violation of a Bell's inequality, e.g. the Clauser-Horne-Shimony-Holt (CHSH) inequality [24], in more than one bipartite subsystem at the same time. In particular, setting $C_{ij} = \mathrm{Tr}\left[\mathcal{R}_{ij}B_ij\right]$, where $B_{ij} = \sqrt{2}(X_iZ_j + Z_iX_j)$ is the observable used in the CHSH inequality tests on qubits i and j, the entanglement monogamy principle can be expressed as [162]:

$$C_{mk} + C_{nk} \leq 4 \tag{5.18}$$

with $k, m, n = 1, 2, 3$ and $k \neq m, n$. It is immediate to show that the inequality in Eq. 5.18 is violated in the state described by $\mathcal{R}_{123}$, because both $\mathcal{R}_{12}$ and $\mathcal{R}_{13}$ describe a maximally-entangled bipartite state, then $C_{12} = C_{13} = 2\sqrt{2}$. Since $\mathcal{R}_{23}$ describes perfect correlations in all basis, we have also $C_{23} = 2\sqrt{2}$, as expected. Note that this is an application of the PDO to describe two distinct time-like separated qubits, i.e. the past and future copy of the qubit within the OTC, which are perfectly correlated in all bases. This differs from the standard use of the PDO as a tool to describe time-like correlations belonging to the same qubit (already known to violate monogamy of entanglement).

5.2.2 Experimental simulation

As a paradigmatic example of the use of the PDO formalism, we implemented a quantum-optical simulation of an OTC, allowing to demonstrate experimentally the entanglement monogamy violation and, at the same time, to reconstruct (for the first time) the PDO modelling the three-qubit system within the OTC chronology-violating region described above. Such simulation consists in reconstructing all the statistics contained in the PDO $\mathcal{R}_{123}$ defined in Eq. 5.16, which represents the OTC in our model. This statistics was collected by creating different sub-ensembles of entangled photon pairs, on which different measurements were realized.

For this purpose, we generated a number of ensembles of polarization-entangled photon pairs, and we exploited each ensemble for generating different statistics. Our setup is built such that one photon can only be measured one time at $t = t_1$, whereas the other one undergoes two sequential measurements respectively at time t_1 and t_2. In the simulation, the former photon takes the role of qubit Q1, while the latter photon represents the qubit entering the OTC (Q2) and its copy emerging from the OTC (Q3).

The experimental setup is shown in Fig. 5.3. We exploit type-II parametric down-conversion (PDC) to generate the entangled state $|\psi_-\rangle = (|HV\rangle - |VH\rangle)/\sqrt{2}$ [163].

In order to evaluate both spatial and temporal correlations, in one of the two photon branches two polarization measurements occur consecutively (Q2 and Q3), both carried by a half-wave plate (HWP, labeled H in Fig. 5.3) followed by a quarter-wave plate (QWP, labeled Q in the figure) and a polarizing beam splitter (PBS). After the PBS in Q2, we put again a QWP and a HWP, for counterbalancing the polarization rotation induced in the measurement process before the Q3 measurement takes place. The other photon branch hosts an identical combination of HWP, QWP and PBS, realizing the Q1 measurement.

The entangled photons are filtered by interference filters (IFs) centered at $\lambda = 808\,\text{nm}$ and with a 3 nm full width at half-maximum (FWHM), and coupled to multi-mode optical fibers connected to silicon single-photon avalanche diodes (SPADs), whose outputs are sent to coincidence electronics.

To obtain the $\mathcal{R}_{123}$ reconstruction we exploited different measurements to collect the three-point and the two-point correlations on the two-photon polarization states. The three-point and two-point measurements have been properly chosen in order to constitute a minimal quorum allowing for a full tomographic reconstruction [100] of $\mathcal{R}_{123}$. This was needed because, in our experimental simulation, it would be impossible to realize a standard three-qubit quantum tomography procedure able to reconstruct $\mathcal{R}_{123}$, because at t_1 the Q2 measurement would obviously affect the one at time t_2 (Q3). Thus, we restricted ourselves to a particular sub-sample of the standard three-qubit tomographic measurements quorum in which the sequential measurements Q2 and Q3 involved commuting observables (i.e. they have been performed in the same polarization basis), avoiding the issues deriving from the measurements temporal ordering. The remaining information needed for the PDO

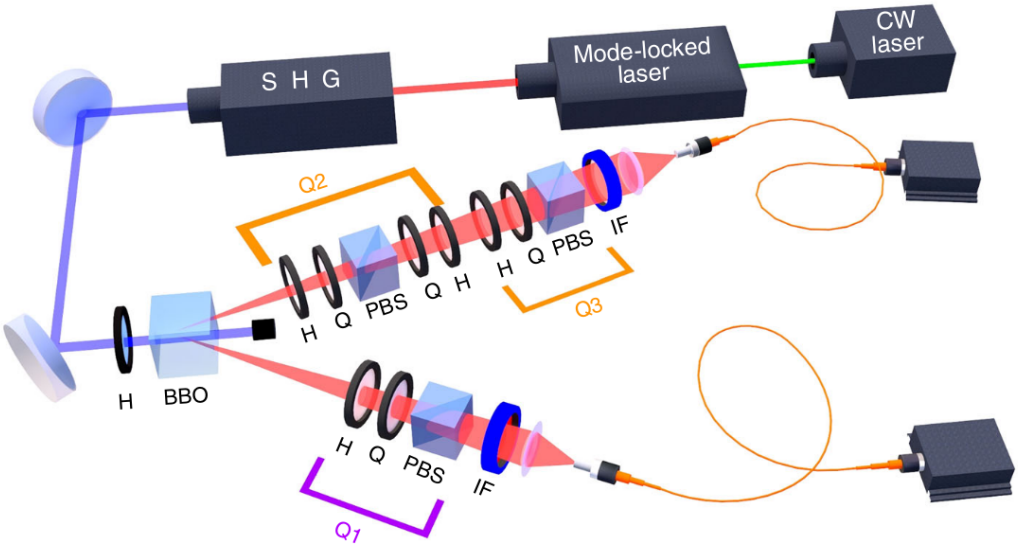

Figure 5.3: Experimental setup. A CW laser at 532 nm pumps a Ti:Sapphire crystal in an optical cavity, generating a mode-locked laser at 808 nm with a 76 MHz repetition rate. The pulsed laser is frequency-doubled by second harmonic generation (SHG) and then injected into a 0.5 mm thick β-barium borate (BBO) crystal, where degenerate non-collinear type-II PDC occurs. By spatially selecting the photons belonging to the intersections of the two PDC cones with interference filters (IFs) and properly compensating the temporal walk-off between the horizontal (H) and vertical (V) polarizations by adding a 0.25 mm thick BBO crystal in both photon paths, we generate the entangled state $|\psi_-\rangle = (|HV\rangle - |VH\rangle)/\sqrt{2}$. Exploiting the combination of a quarter-wave (Q), a half-wave plate (H) and a polarizing beam splitter (PBS), two polarization measurements (Q2 and Q3) are performed in sequence on a branch and one (Q1) on the other branch. Correlations among them allow demonstrating violation of monogamy relation for PDO, simulating the OTC scenario.

reconstruction, instead, is obtained from the two-point correlation measurements. More in detail, for the two-point correlations we prepared an ensemble for which one photon undergoes the measurement of the whole set of observables $\{X, Y, Z\}$ at time t_1 and t_2, including all possible cross-correlations between different observables. This provides the full reconstruction of the reduced pseudo-state $\mathcal{R}_{23}$ defined in Eq. 5.17. To complete the two-point correlations extraction procedure, other two ensembles are needed: one for measuring $\{X, Y, Z\}$ on both photons at time t_1, providing $\mathcal{R}_{12}$, and the other for reconstructing $\mathcal{R}_{13}$, where one of the two photons undergoes the measurement of $\{X, Y, Z\}$ at time t_2. Finally, for computing the three-point correlations, it is necessary an ensemble where one measures $\{X, Y, Z\}$ once at time t_1 on one photon, and twice at time t_1 and t_2 on the other one. From the conjectured $\mathcal{R}_{123}$ (see Eq. 5.16) we expect all the three-point correlations to be equal to zero.

Our predictions are well confirmed by the experimental results, shown in the following section.

5.2.3 Experimental results

The reconstructed PDO $\mathcal{R}_{123}$ and its marginals are shown in Fig. 5.4 [143] compared with the respective theoretical expectations. This procedure highlights interesting prop-

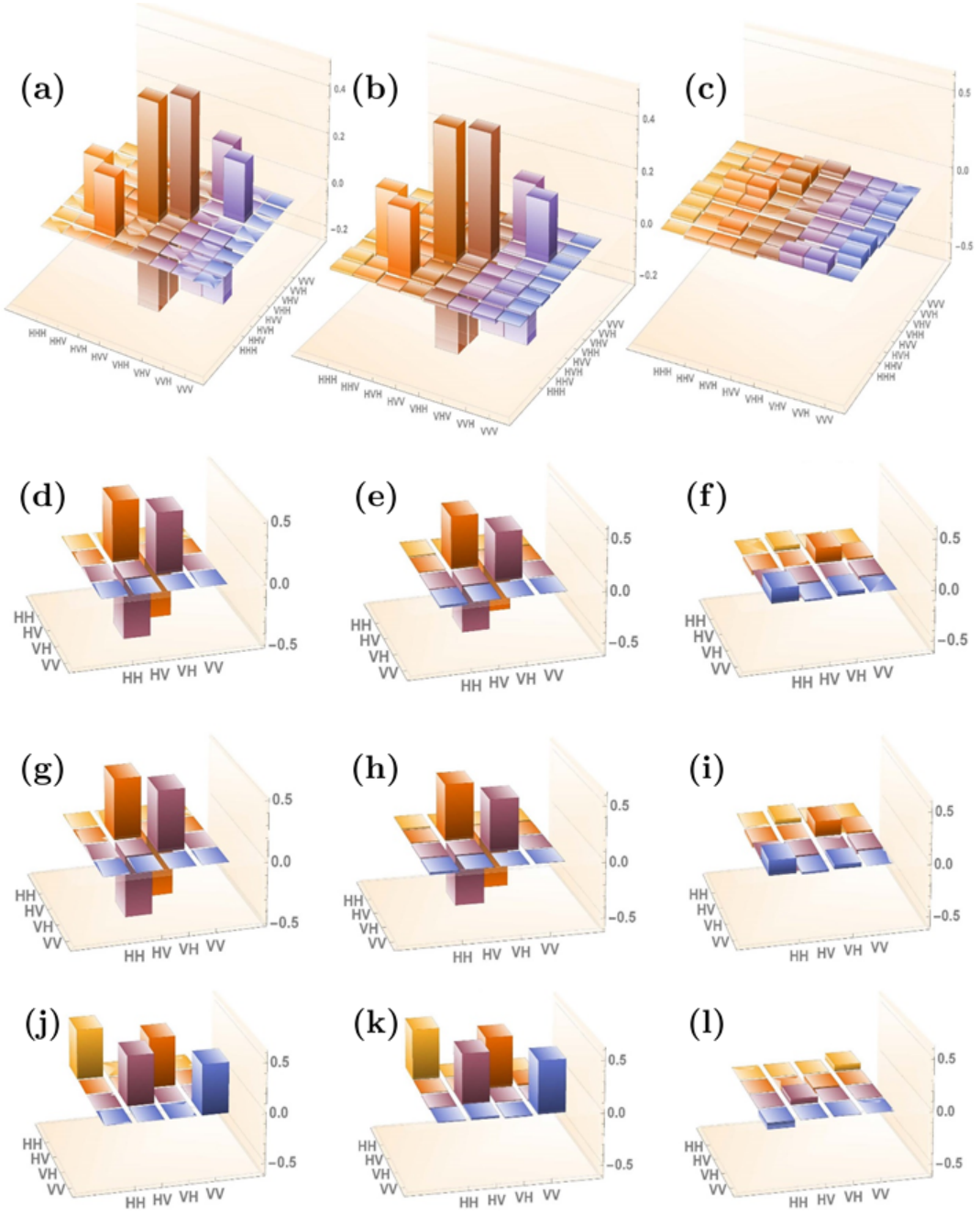

Figure 5.4: PDO tomographic reconstruction. In the upper row, we plot the real part of the theoretical $\mathcal{R}_{123}$ **(a)** (since, theoretically, $\mathrm{Im}\left[\mathcal{R}_{123}\right] = 0$), compared with the real **(b)** and imaginary **(c)** part of the experimentally-reconstructed $\mathcal{R}_{123}$. Below, theoretical marginals $\mathcal{R}_{12}$, $\mathcal{R}_{13}$ and $\mathcal{R}_{23}$ (plots **(d)**, **(g)** and **(j)** respectively, again considering that in our model $\mathrm{Im}\left[\mathcal{R}_{12}\right] = \mathrm{Im}\left[\mathcal{R}_{13}\right] = \mathrm{Im}\left[\mathcal{R}_{23}\right] = 0$) compared with the real (plots **(e)**, **(h)** and **(k)**) and imaginary (plots **(f)**, **(i)** and **(l)**) part of their reconstructed counterparts.

erties of the PDO, which had gone unnoticed until now. Formally, just like for density operators, the reduced PDO of some subsystems is obtained by taking the trace on the remaining subsystems, e.g. $\mathcal{R}_{13} = \mathrm{Tr}_2\left[\mathcal{R}_{123}\right]$ in our case.

However, unlike for density operators, $\mathcal{R}_{13}$ cannot be reconstructed experimentally by

exploiting the measurements obtained for the three-point correlations and then averaging over the results of the measurements on the other photon measured at time t_1. This is because the trace over a temporal degree of freedom is not equivalent to averaging with respect to all possible values of the observables that can be measured at that time. Indeed, $\mathrm{Tr}\left[\Pi\mathcal{R}_{123}\right]$, where Π is a generic projector could be negative, hence it cannot be interpreted, in general, as a probability (unless we allow probabilities to take negative values [147]). This is a general property of PDOs: they are not-positive operators because the subsystems' degrees of freedom they describe do not always represent spatial subsystems, but they could represent time-like separated systems, as in the case of qubits Q2 and Q3. Therefore, the full tomographic reconstruction procedure for a PDO is necessarily different with respect to the one needed for a traditional density operator.

Concerning our OTC quantum-optical simulation, all the PDO reconstructions are in excellent agreement with the theoretical predictions, as certified by the Uhlmann fidelities [101] obtained for the two PDO marginals modelling proper physical states, i.e. $\mathcal{R}_{12}$ and $\mathcal{R}_{13}$, for which we respectively obtained $F_{12} = 0.964$ and $F_{13} = 0.963$ (being F_{ij} the fidelity of the reconstructed $\mathcal{R}_{ij}$ marginal with respect to the theoretically-expected singlet state density operator).

By using Eq. 5.18, we also reconstructed the statistics from a CHSH test on all the possible pairs among the qubits Q1, Q2 and Q3, to demonstrate the predicted violation of the entanglement monogamy principle. For the temporal domain, the CHSH inequality is $C_{23}^{(exp)} = 2.84 \pm 0.02$, in perfect agreement with the predicted maximal violation, corresponding to the Tsirelson's bound $2\sqrt{2}$. Then, we measured the CHSH on both the photons at time t_1 (Q1 and Q2, spatial domain), achieving $C_{12}^{(exp)} = 2.69 \pm 0.02$: a sharp violation of the classical bound. From these results, it follows:

$$C_{12}^{(exp)} + C_{23}^{(exp)} = 5.52 \pm 0.03 \tag{5.19}$$

showing a 160 standard deviations violation of the entanglement monogamy relation given by Eq. 5.18. Furthermore, since we could not perform a direct CHSH inequality measurement on qubits Q1 and Q3 because of the occurring Q2 measurement, in this case we extracted the CHSH inequality value directly from the reconstructed $\mathcal{R}_{13}$, obtaining $C_{13}^{(rec)} = 2.73$. This allows obtaining the remaining entanglement monogamy violations:

$$C_{12}^{(exp)} + C_{13}^{(rec)} = 5.42 \pm 0.07 \tag{5.20}$$

$$C_{23}^{(exp)} + C_{13}^{(rec)} = 5.55 \pm 0.07 \tag{5.21}$$

where, as uncertainty, we consider a 99% confidence interval on the experimental data. These results, showing the first PDO reconstruction, give a clear demonstration of the robustness and reliability of our technique, granting the possibility of using PDOs to describe scenarios in which temporal correlations play a crucial role in the dynamics of the system, preserving at the same time the linearity of such dynamics.

5.3 PDO formalism and the reconciliation of the black hole information loss paradox

In a subsequent work [144], we applied the PDO formalism to the second scenario mentioned in this chapter introduction, i.e. the black hole evaporation [148]. This process represents a problem from the quantum mechanical perspective [142, 148, 164, 165], as well

as other cosmological aspects [166–169]. In short, if the process is unitary as prescribed by quantum theory, then entanglement must be created between the exterior and the interior of the black hole as particle pairs are generated through the process of Hawking radiation [170–173].

This can be better understood by considering an elementary model of evaporation based on a finite number of qubits. After half of the qubits in the black hole has evaporated, one can conjecture that a maximally-entangled state has formed between the qubits in the interior and the ones in the exterior of the black hole, assuming thermal radiation has been emitted in the process. As the black hole continues to evaporate, Hawking radiation would imply that even more entanglement is generated between the interior and the exterior of the black hole. Anyway, for the previously mentioned entanglement monogamy principle, this cannot happen, since qubits already maximally entangled cannot be made entangled with anything else. Therefore, the claim is that, if one is trying to preserve the unitarity of black hole evaporation, then the black hole evaporation itself ought to violate the monogamy of entanglement [174].

Actually, the issue of whether such a paradox exists or not goes beyond the aim of this thesis. However, it has been hotly debated, and the reader can see e.g. Ref. [175] and references herein. With our work, we would like instead to suggest that, assuming that the paradox exists, a simple re-interpretation of the evaporation process could provide a reconciliation of such paradox. In general relativity, crossing the event horizon of a black hole for a particle is equivalent to swapping the signatures of the spatial and temporal coordinates of the space-time [176]. If one thinks of a typical quantum phase factor $e^{i(kx-\omega t)}$, the change of the sign of space and time simply corresponds to complex conjugation of such phase factor. For these reason, the effect on a density operator of an in-falling quantum system should be described by the operation of transposition (which swaps the operator off-diagonal elements, therefore implementing the complex conjugation). It is well known that transposition is a positive, but not completely positive, operation. Then, if one performs the transposition on just one of two entangled subsystems, the overall system may not end up being a physical density operator. Here, we proposed to use this fact to resolve the apparent entanglement monogamy violation during the evaporation of a black hole by exploiting the PDO formalism, because of its possibility of describing temporal correlations, thus including physical scenarios efficiently described by Hermitian operators that are not positive.

Our point is that, given that the partial transposition can model what happens to a pair of entangled qubits due to one of them falling into a black hole, one could use the PDO $\mathcal{R}_{12}$ defined in Eq. 5.12 as a candidate for describing the state of such pair after one of the qubits has entered the black hole.

Based on this heuristic reasoning, we proposed a PDO to model the situation where one of the qubits in the pair gets further entangled with a third particle. In particular, we showed that a viable solution to the black hole information problem can be achieved by postulating that the PDO $\mathcal{R}_{123}$ defined in Eq. 5.17, generalizing the above pseudo-state $\mathcal{R}_{12}$, represents the state of two initially entangled qubits after one of them has crossed the event horizon and fallen into the black hole, getting entangled with a third qubit. This PDO can perfectly model the correlations associated with the black-hole evaporation scenario, because it treats equally temporal and spatial correlations and, unlike density operators, PDOs can be used to describe a situation in which one of two maximally temporally-correlated qubits becomes entangled (i.e. maximally spatially correlated) with another qubit.

Since the PDO needed to describe this scenario is formally equivalent to the one mod-

elling the OTC framework, we can consider the experimental results obtained in our OTC quantum-optical simulation to be valid also for the case of an entangled particle falling into the evaporating black hole. Aside of the reconstruction of the physical system PDO $\mathcal{R}_{123}$ presented in Fig. 5.4, what is more interesting in this case is that, even in the black-hole evaporation framework, the occurring entanglement monogamy violations reported in Eqs. 5.19-5.21 are not paradoxical anymore within this new formalism, as the PDO could accommodate and describe correlations generating such violations when temporal degrees of freedom are involved.

This work only offers a first exploration of applying this idea to the specific scenario of black-hole evaporation, leaving a more general theory to be developed in the future, should this approach prove useful. More generally, some models of quantum gravity might require space-time to be quantized, whereby the distinction between time-like and space-like degrees of freedom may become blurred below certain scales. This has prompted a number of proposals, for example, to modify the commutation relations of observables of different subsystems [177], or to incorporate indefinite causal order [132, 134, 178]. The PDO formalism, in light of what is proposed in our papers in Refs. [143] and [144], might be a candidate to generalize the notion of quantum states to these scenarios.

Chapter 6

Conclusions

During my PhD studies, I was involved in several experiments regarding different measurement paradigms in QM and their possible applications to both the fundamental research and the quantum technologies framework (e.g. Quantum Metrology and Quantum Information). All of these experiments were based on quantum-optical setups, implemented within the "Carlo Novero" Quantum Optics laboratories of the Istituto Nazionale di Ricerca Metrologica (INRiM). Among them, in this thesis I presented the four works in which I was more involved.

The first one aimed to demonstrate an efficient method to obtain the optimal estimation (i.e. the one giving the minimum quantum uncertainty achievable) of several nonclassicality parameters, related either to entanglement or discord in two-qubit states. We directly evaluated the amount of entanglement by estimating Negativity, Concurrence and Log-Negativity, while we approximately evaluated the amount of discord by estimating the Quantum Geometric Discord. For each of these quantities, we introduced two estimators, a non-optimal one and an optimal one, for a particular family of states that have a recognized importance in the field of quantum information and related technologies. By evaluating the statistical uncertainties as the standard deviations on repeated measurements, we achieved a good agreement between the theoretical predictions and the experimental results. In particular, we demonstrated that optimal estimators allow reaching the ultimate theoretical precision limit represented by the quantum Cramér-Rao bound. The agreement between the computed uncertainty bars and theoretical uncertainty curves, also for what concerns non-optimal estimators, represents a further check on the consistency between our experimental data and the theory. It is possible to note a significant reduction of the uncertainties given by the optimal estimators with respect to the ones granted by the non-optimal estimators, demonstrating a strong and practical advantage in the use of the optimal ones. These results pave the way to the diffuse use of these estimators in quantifying resources for quantum technologies.

For our second work, we theoretically derived and experimentally implemented a new paradigm of quantum measurement: the Genetic Quantum Measurement (GQM). Such paradigm takes advantage of a genetic-like approach to significantly surpass, in terms of precision, the performances of the conventional projector-based quantum measurement techniques. GQMs exploit a sequence of identical steps, each composed of a first part of (unitary) interaction/interference, and a second part in which a selective measurement occurs. The effect of the interaction-interference event consists in coupling the observable of interest (OoI) with an ancillary "meter" observable that will be used to perform the indirect measurement of the OoI, as in von Neumann measurement, and then applying a "selection pressure" on the resulting state. This procedure is repeated several times, before detecting

the quantum system. By looking at the whole GQM process, one can find similarities with the bio-inspired mechanisms of mutation, crossover and selection (the first two mediated by the interaction/interference, the last one by the selective measurement) typical of genetic algorithms. Furthermore, GQM allows obtaining an uncertainty substantially reduced with respect to the one achievable with the usual projective measurement approach when the same initial resources, i.e. the number of initial individual quantum systems, are considered, a quite surprising feature, because projective measurements saturate the Quantum Cramér-Rao bound in the investigated framework. Thus, with our results we showed both theoretically and experimentally that GQMs represent a real paradigm shift in quantum measurement, granting unprecedented measurement capability and representing a potentially groundbreaking tool for Quantum Metrology and other quantum technologies. GQMs can be extremely useful, e.g., for testing the fairness of quantum random number generators, largely exploited in Quantum Key Distribution protocols.

In the last two works, we investigated the properties of a new formalism for describing quantum mechanical systems, i.e. the Pseudo-Density Operator (PDO): a generalization of the density operator formalism allowing to describe on an equal footing both spatial and temporal correlations within quantum states.

In the first of these works, our proposal was to show a radically different way of generalizing quantum theory to describe chronology-violating regions containing an open timelike curve (OTC), whose features we have simulated experimentally. The proposed PDO is a viable descriptor of the physical situation where a qubit, entangled with a second qubit, enters an OTC. By proposing to use a PDO to describe the three qubits in the chronology-violating region, we depart from standard quantum mechanics, because we use a non-positive operator to describe the (pseudo-)state of the qubits within the chronology-violation region. Our proposal hints at a different way of formulating quantum theory, where, to describe a physical system with a certain dynamics, one gives the PDO as a faithful description of that physical situation. In order to experimentally demonstrate our claims, we performed for the first time a variant of traditional quantum state tomography, able to reconstruct the three-qubit PDO modelling the OTC physical scenario. Then, we calculated the violation of the entanglement monogamy principle (a paradoxical event in the traditional density operator framework, naturally allowed by the PDO when temporal correlations are involved) directly with the marginals obtained from such experimental PDO reconstruction, achieving an excellent agreement with respect to the theoretical predictions.

Now, once that step is taken, is it still possible to preserve some notion of linearity even when describing situations where properties like entanglement monogamy are violated? We conjecture that the answer is yes, because any two PDOs describing such physical situations (e.g. two OTCs with different initial states) can be related by a linear transformation. This notion of linearity is, however, different from the linearity of quantum mechanical evolution.

In the second experiment, instead, we proposed an alternative resolution of the information loss paradox in black hole evaporation, based on the PDO formalism. We conjectured that the phenomenology of black hole evaporation, as described by Hawking's radiation, could be modeled by a PDO instead of a standard density operator. We proposed a specific form for the PDO that could describe a pair of initially entangled qubits, one falling into a black hole and the other maximally entangled with a third qubit, after evaporating. The usual paradoxes due to violations of entanglement monogamy did not arise in this formalism, as the PDO could accommodate and describe correlations that violated monogamy. In order to illustrate the temporal and spatial correlations in the proposed PDO, we used a quantum optical demonstration, building an experiment that simulated this physical

phenomenon as described by the same pseudo-density matrix. We reconstructed experimentally the correlations in the proposed pseudo-density matrix, demonstrating how the violation of entanglement monogamy could emerge in the analyzed framework.

All these results promise to have further implications both in the Quantum Metrology and the QM foundations research frameworks, representing a first step towards novel theoretical and experimental approaches both in fundamental research and for the applied, fast-growing field of quantum technologies.

Acknowledgments

I would like to thank Dr. Marco Genovese, who gave me the opportunity to make my PhD research work in the Quantum Optics laboratories at INRiM, constantly supervising and promoting my scientific progresses within the PhD period.
I also thank the whole INRiM Quantum Optics group, in particular Dr. Alessio Avella, Dr. Ivo Pietro Degiovanni, Dr. Marco Gramegna, Dr. Alice Meda and Dr. Fabrizio Piacentini (who also gave me precious suggestions for this thesis), for always being helpful and willing to share their know-how both in experimental and theoretical aspects of my research work.

In particular, I want to thank my fiancée Melinda, my parents Francesco and Lina, and my sister Ivana, for always strongly supporting me in my decisions.

Bibliography

[1] N. Gisin, G. Ribordy, W. Tittel, and H. Zbinden. Quantum cryptography. *Rev. Mod. Phys.*, 74:145–195, 2002.

[2] C.H. Bennett, F. Bessette, G. Brassard, L. Salvail, and J. Smolin. Experimental quantum cryptography. *Journal of Cryptology*, 5(1):3–28, 1992.

[3] T. Jennewein, C. Simon, G. Weihs, H. Weinfurter, and A. Zeilinger. Quantum cryptography with entangled photons. *Phys. Rev. Lett.*, 84:4729–4732, 2000.

[4] V. Scarani, H. Bechmann-Pasquinucci, N. J. Cerf, M. Dušek, N. Lütkenhaus, and M. Peev. The security of practical quantum key distribution. *Rev. Mod. Phys.*, 81:1301–1350, 2009.

[5] M.A. Nielsen and I.L. Chuang. *Quantum Computation and Quantum Information*. Cambridge Series on Information and the Natural Sciences. Cambridge University Press, 2000.

[6] R. Rivest, A. Shamir, and L. Adleman. A method for obtaining digital signatures and public-key cryptosystems. *Communications of the ACM*, 21(2):120–126, 1978.

[7] A. Ekert and R. Jozsa. Quantum computation and shor's factoring algorithm. *Rev. Mod. Phys.*, 68:733–753, 1996.

[8] T. D. Ladd, J. R. Goldman, F. Yamaguchi, Y. Yamamoto, E. Abe, and K. M. Itoh. All-silicon quantum computer. *Phys. Rev. Lett.*, 89:017901, 2002.

[9] R. Raussendorf and H. J. Briegel. A one-way quantum computer. *Phys. Rev. Lett.*, 86:5188–5191, 2001.

[10] B. E. Kane. A silicon-based nuclear spin quantum computer. *Nature*, 393(6681):133–137, 1998.

[11] D. Kielpinski, C. Monroe, and D. J. Wineland. Architecture for a large-scale ion-trap quantum computer. *Nature*, 417(6890):709–711, 2002.

[12] F. Arute *et al.* Quantum supremacy using a programmable superconducting processor. *Nature*, 574(7779):505–510, 2019.

[13] A. Meda, E. Losero, N. Samantaray, F. Scafirimuto, S. Pradyumna, A Avella, I. Ruo Berchera, and M. Genovese. Photon-number correlation for quantum enhanced imaging and sensing. *Journal of Optics*, 19(9):094002, 2017.

[14] M. Genovese. Real applications of quantum imaging. *Journal of Optics*, 18(7):073002, 2016.

[15] G. Brida, M. Genovese, and I. Ruo Berchera. Experimental realization of sub-shot-noise quantum imaging. *Nature Photonics*, 4(4):227–230, 2010.

[16] L. Mandel and E. Wolf. *Optical Coherence and Quantum Optics*. Cambridge University Press, 2014.

[17] A. M. Fox. *Quantum Optics: An Introduction*. Oxford Master Series in Physics. OUP Oxford, 2006.

[18] V. Giovannetti, S. Lloyd, and L. Maccone. Quantum-enhanced measurements: Beating the standard quantum limit. *Science*, 306(5700):1330–1336, 2004.

[19] K. Goda, O. Miyakawa, E. E. Mikhailov, S. Saraf, R. Adhikari, K. McKenzie, R. Ward, S. Vass, A. J. Weinstein, and N. Mavalvala. A quantum-enhanced prototype gravitational-wave detector. *Nature Physics*, 4(6):472–476, 2008.

[20] I. Ruo-Berchera, I. P. Degiovanni, S. Olivares, P. Traina, N. Samantaray, and M. Genovese. Improving interferometers by quantum light: toward testing quantum gravity on an optical bench. In Ronald E. Meyers, Yanhua Shih, and Keith S. Deacon, editors, *Quantum Communications and Quantum Imaging XIV*, volume 9980, pages 35 – 43. International Society for Optics and Photonics, SPIE, 2016.

[21] K. Kraus, A. Böhm, J.D. Dollard, and W.H. Wootters. *States, Effects, and Operations: Fundamental Notions of Quantum Theory*. Lecture Notes in Physics. Springer Berlin Heidelberg, 1983.

[22] A. Einstein, B. Podolsky, and N. Rosen. Can quantum-mechanical description of physical reality be considered complete? *Phys. Rev.*, 47:777–780, 1935.

[23] J. S. Bell. On the einstein podolsky rosen paradox. *Physics*, 1(3):195–200, 1964.

[24] J. F. Clauser, M. A. Horne, A. Shimony, and R. A. Holt. Proposed experiment to test local hidden-variable theories. *Phys. Rev. Lett.*, 23:880–884, 1969.

[25] L. K. Shalm *et al.* Strong loophole-free test of local realism. *Phys. Rev. Lett.*, 115:250402, 2015.

[26] M. Giustina *et al.* Significant-loophole-free test of bell's theorem with entangled photons. *Phys. Rev. Lett.*, 115:250401, 2015.

[27] J. von Neumann, R.T. Beyer, and N.A. Wheeler. *Mathematical Foundations of Quantum Mechanics: New Edition*. Princeton University Press, 2018.

[28] R. J. Glauber. Coherent and incoherent states of the radiation field. *Phys. Rev.*, **131**:2766–2788, 1963.

[29] R. W. Boyd. *Nonlinear Optics, Third Edition*. Academic Press, 3 edition, 2008.

[30] P. A. Franken, A. E. Hill, C. W. Peters, and G. Weinreich. Generation of optical harmonics. *Phys. Rev. Lett.*, 7:118–119, 1961.

[31] Y. R. Shen. Quantum statistics of nonlinear optics. *Phys. Rev.*, 155:921–931, 1967.

[32] Y. R. Shen. *The principles of nonlinear optics*. Wiley, New York, NY, 1984.

[33] M. Hillery and L. D. Mlodinow. Quantization of electrodynamics in nonlinear dielectric media. *Phys. Rev. A*, 30:1860–1865, 1984.

[34] M. Schubert and B. Wilhelmi. *Nonlinear optics and quantum electronics*. 1986.

[35] Kozierowski. M. and R. Tanaś. Quantum fluctuations in second-harmonic light generation. *Optics Communications*, 21(2):229 – 231, 1977.

[36] A. Migdall, S.V. Polyakov, J. Fan, and J.C. Bienfang. *Single-Photon Generation and Detection: Physics and Applications*. ISSN. Elsevier Science, 2013.

[37] D. Magde and H. Mahr. Study in ammonium dihydrogen phosphate of spontaneous parametric interaction tunable from 4400 to 16 000 å. *Phys. Rev. Lett.*, 18:905–907, 1967.

[38] S. A. Akhmanov, V. V. Fadeev, R. V. Khokhlov, and O. N. Chunaev. *J.Exptl.Theoret.Phys.(JETP) Letters*, 6:85–87, 1967.

[39] R. L. Byer and S. E. Harris. Power and bandwidth of spontaneous parametric emission. *Phys. Rev.*, 168:1064–1068, 1968.

[40] D. C. Burnham and D. L. Weinberg. Observation of simultaneity in parametric production of optical photon pairs. *Phys. Rev. Lett.*, 25:84–87, 1970.

[41] P.G. Kwiat, K. Mattle, H. Weinfurter, A. Zeilinger, A.V. Sergienko, and Y. Shih. New high-intensity source of polarization-entangled photon pairs. *Physical Review Letters*, 75(24):4337–4341, 1995.

[42] G. Weihs, T. Jennewein, C. Simon, H. Weinfurter, and A. Zeilinger. Violation of bell's inequality under strict einstein locality conditions. *Phys. Rev. Lett.*, 81:5039–5043, 1998.

[43] T. Jennewein, C. Simon, G. Weihs, H. Weinfurter, and A. Zeilinger. Quantum cryptography with entangled photons. *Physical Review Letters*, 84(20):4729–4732, 2000.

[44] D. Bouwmeester, J.-W. Pan, K. Mattle, M. Eibl, H. Weinfurter, and A. Zeilinger. Experimental quantum teleportation. *Nature*, 390(6660):575–579, 1997.

[45] D. Bouwmeester, J.-W. Pan, M. Bongaerts, and A. Zeilinger. Observation of three-photon greenberger-horne-zeilinger entanglement. *Physical Review Letters*, 82(7):1345–1349, 1999.

[46] W.P. Grice and I.A. Walmsley. Spectral information and distinguishability in type-ii down-conversion with a broadband pump. *Physical Review A - Atomic, Molecular, and Optical Physics*, 56(2):1627–1634, 1997. cited By 393.

[47] W. Wasilewski, C. Radzewicz, R. Frankowski, and K. Banaszek. Statistics of multiphoton events in spontaneous parametric down-conversion. *Phys. Rev. A*, 78:033831, 2008.

[48] W. Mauerer, M. Avenhaus, W. Helwig, and C. Silberhorn. How colors influence numbers: Photon statistics of parametric down-conversion. *Phys. Rev. A*, 80:053815, 2009.

[49] J. A. Armstrong, N. Bloembergen, J. Ducuing, and P. S. Pershan. Interactions between light waves in a nonlinear dielectric. *Phys. Rev.*, 127:1918–1939, 1962.

[50] K. N. Cassemiro, K. Laiho, and C. Silberhorn. Accessing the purity of a single photon by the width of the hong–ou–mandel interference. *New Journal of Physics*, 12(11):113052, 2010.

[51] W. Wasilewski, P. Kolenderski, and R. Frankowski. Spectral density matrix of a single photon measured. *Phys. Rev. Lett.*, 99:123601, 2007.

[52] J.H. Eberly. Schmidt analysis of pure-state entanglement. *Laser Physics*, 16(6):921–926, 2006.

[53] G. Vidal and R. F. Werner. Computable measure of entanglement. *Phys. Rev. A*, 65:032314, 2002.

[54] A. Avella. Theory of parametric down conversion in bulk non-linear crystals: An introduction. *Journal of Advanced Physics*, 4(3):252–262, 2015.

[55] H. Ollivier and W. H. Zurek. Quantum discord: A measure of the quantumness of correlations. *Phys. Rev. Lett.*, 88:017901, 2001.

[56] M. Genovese and M. Gramegna. Quantum correlations and quantum non-locality: A review and a few new ideas. *Applied Sciences*, 9:5406, 2019.

[57] S. Virzì, E. Rebufello, A. Avella, F. Piacentini, M. Gramegna, I. Ruo Berchera, I. P. Degiovanni, and M. Genovese. Optimal estimation of entanglement and discord in two-qubit states. *Scientific Reports*, 9(1):3030, 2019.

[58] D. F. V. James, P. G. Kwiat, W. J. Munro, and A. G. White. *On the Measurement of Qubits*.

[59] M. G. A. Paris and J. Rehacek. *Quantum State Estimation*. Springer-Verlag Berlin Heidelberg, 2004.

[60] I. Bengtsson and K. Życzkowski. *Geometry of Quantum States: An Introduction to Quantum Entanglement*. Cambridge University Press, 2017.

[61] S. Hill and W. K. Wootters. Entanglement of a pair of quantum bits. *Phys. Rev. Lett.*, 78:5022–5025, 1997.

[62] B. Dakić, V. Vedral, and Č. Brukner. Necessary and sufficient condition for nonzero quantum discord. *Phys. Rev. Lett.*, 105:190502, 2010.

[63] C. H. Bennett, H. J. Bernstein, S. Popescu, and B. Schumacher. Concentrating partial entanglement by local operations. *Phys. Rev. A*, 53:2046–2052, 1996.

[64] R. Horodecki, P. Horodecki, M. Horodecki, and K. Horodecki. Quantum entanglement. *Rev. Mod. Phys.*, 81:865–942, 2009.

[65] Otfried Gühne and Géza Tóth. Entanglement detection. *Physics Reports*, 474(1):1 – 75, 2009.

[66] R. Augusiak and M. Lewenstein. Towards measurable bounds on entanglement measures. *Quantum Information Processing*, 8(6):493–521, 2009.

[67] P. Horodecki. Measuring quantum entanglement without prior state reconstruction. *Phys. Rev. Lett.*, 90:167901, 2003.

[68] V. Vedral, M. B. Plenio, M. A. Rippin, and P. L. Knight. Quantifying entanglement. *Phys. Rev. Lett.*, 78:2275–2279, 1997.

[69] H. Wunderlich and M. B. Plenio. Quantitative verification of entanglement and fidelities from incomplete measurement data. *Journal of Modern Optics*, 56(18-19):2100–2105, 2009.

[70] J. Eisert, F. G. S. L. Brandão, and K. M. R. Audenaert. Quantitative entanglement witnesses. *New Journal of Physics*, 9(3):46–46, 2007.

[71] K. M. R. Audenaert and M. B. Plenio. When are correlations quantum?—verification and quantification of entanglement by simple measurements. *New Journal of Physics*, 8(11):266–266, 2006.

[72] P. Lougovski and S. J. van Enk. Characterizing entanglement sources. *Phys. Rev. A*, 80:052324, 2009.

[73] G. Jaeger, M. A. Horne, and A. Shimony. Complementarity of one-particle and two-particle interference. *Phys. Rev. A*, 48:1023–1027, 1993.

[74] M. Horodecki, P. Horodecki, and R. Horodecki. Separability of n-particle mixed states: necessary and sufficient conditions in terms of linear maps. *Physics Letters A*, 283(1):1 – 7, 2001.

[75] B. M. Terhal. Bell inequalities and the separability criterion. *Physics Letters A*, 271(5):319 – 326, 2000.

[76] O. Gühne, P. Hyllus, D. Bruß, A. Ekert, M. Lewenstein, C. Macchiavello, and A. Sanpera. Detection of entanglement with few local measurements. *Phys. Rev. A*, 66:062305, 2002.

[77] F. G. S. L. Brandão and R. O. Vianna. Witnessed entanglement. *International Journal of Quantum Information*, 04(02):331–340, 2006.

[78] P. Krammer, H. Kampermann, D. Bruß, R. A. Bertlmann, L. C. Kwek, and C. Macchiavello. Multipartite entanglement detection via structure factors. *Phys. Rev. Lett.*, 103:100502, 2009.

[79] P. Facchi, G. Florio, and S. Pascazio. Characterizing and measuring multipartite entanglement. *International Journal of Quantum Information*, 05(01n02):97–103, 2007.

[80] M. V. Fedorov, M. A. Efremov, P. A. Volkov, and J. H. Eberly. Short-pulse or strong-field breakup processes: a route to study entangled wave packets. *Journal of Physics B: Atomic, Molecular and Optical Physics*, 39(13):S467–S483, 2006.

[81] P. A. Volkov, Yu. M. Mikhailova, and M. V. Fedorov. Spectral entanglement in parametric down-conversion with nondegenerate frequencies. *Advanced Science Letters*, 2(4):511–516, 2009.

[82] M. Genovese. Research on hidden variable theories: A review of recent progresses. *Physics Reports*, 413(6):319 – 396, 2005.

[83] M. Bourennane, M. Eibl, C. Kurtsiefer, S. Gaertner, H. Weinfurter, O. Gühne, P. Hyllus, D. Bruß, M. Lewenstein, and A. Sanpera. Experimental detection of multipartite entanglement using witness operators. *Phys. Rev. Lett.*, 92:087902, 2004.

[84] M. V. Fedorov, M. A. Efremov, P. A. Volkov, E. V. Moreva, S. S. Straupe, and S. P. Kulik. Anisotropically and high entanglement of biphoton states generated in spontaneous parametric down-conversion. *Phys. Rev. Lett.*, 99:063901, 2007.

[85] M. V. Fedorov, M. A. Efremov, P. A. Volkov, E. V. Moreva, S. S. Straupe, and S. P. Kulik. Spontaneous parametric down-conversion: Anisotropical and anomalously strong narrowing of biphoton momentum correlation distributions. *Phys. Rev. A*, 77:032336, 2008.

[86] G. Brida, V. Caricato, M. V. Fedorov, M. Genovese, M. Gramegna, and S. P. Kulik. Characterization of spectral entanglement of spontaneous parametric-down conversion biphotons in femtosecond pulsed regime. *EPL (Europhysics Letters)*, 87(6):64003, 2009.

[87] M. Avenhaus, M. V. Chekhova, L. A. Krivitsky, G. Leuchs, and C. Silberhorn. Experimental verification of high spectral entanglement for pulsed waveguided spontaneous parametric down-conversion. *Phys. Rev. A*, 79:043836, 2009.

[88] M. Barbieri, F. De Martini, G. Di Nepi, P. Mataloni, G. M. D'Ariano, and C. Macchiavello. Detection of entanglement with polarized photons: Experimental realization of an entanglement witness. *Phys. Rev. Lett.*, 91:227901, 2003.

[89] S. P. Walborn, P. H. Souto Ribeiro, L. Davidovich, F. Mintert, and A. Buchleitner. Experimental determination of entanglement with a single measurement. *Nature*, 440(7087):1022–1024, 2006.

[90] M. P. Almeida, F. de Melo, M. Hor-Meyll, A. Salles, S. P. Walborn, P. H. S. Ribeiro, and L. Davidovich. Environment-induced sudden death of entanglement. *Science*, 316(5824):579–582, 2007.

[91] M. G. A. Paris. Quantum estimation for quantum technology. *International Journal of Quantum Information*, 07(supp01):125–137, 2009.

[92] A. Peres. Separability criterion for density matrices. *Phys. Rev. Lett.*, 77:1413–1415, 1996.

[93] R. F. Werner. Quantum states with einstein-podolsky-rosen correlations admitting a hidden-variable model. *Phys. Rev. A*, 40:4277–4281, 1989.

[94] E. Knill and R. Laflamme. Power of one bit of quantum information. *Phys. Rev. Lett.*, 81:5672–5675, 1998.

[95] A. Brodutch and D. R. Terno. Quantum discord, local operations, and maxwell's demons. *Phys. Rev. A*, 81:062103, 2010.

[96] P. Giorda and M. G. A. Paris. Gaussian quantum discord. *Phys. Rev. Lett.*, 105:020503, 2010.

[97] K. Zyczkowski and H.J. Sommers. Hilbert-schmidt volume of the set of mixed quantum states. *Journal of Physics A: Mathematical and General*, 36(39):10115–10130, 2003.

[98] S. Virmani and M.B. Plenio. Ordering states with entanglement measures. *Physics Letters A*, 268(1):31 – 34, 2000.

[99] N. Boeuf, D. Branning, I. Chaperot, E. Dauler, S. Guerin, G. Jaeger, Antoine Muller, and Alan L. Migdall. Calculating characteristics of noncollinear phase matching in uniaxial and biaxial crystals. *Optical Engineering*, 39:1016–1024, 2000.

[100] Y. I. Bogdanov, G. Brida, I. D. Bukeev, M. Genovese, K. S. Kravtsov, S. P. Kulik, E. V. Moreva, A. A. Soloviev, and A. P. Shurupov. Statistical estimation of the quality of quantum-tomography protocols. *Phys. Rev. A*, 84:042108, 2011.

[101] R. Jozsa. Fidelity for mixed quantum states. *Journal of Modern Optics*, 41(12):2315–2323, 1994.

[102] G. Brida, I. P. Degiovanni, A. Florio, M. Genovese, P. Giorda, A. Meda, M. G. A. Paris, and A. Shurupov. Experimental estimation of entanglement at the quantum limit. *Phys. Rev. Lett.*, 104:100501, 2010.

[103] G. Carvacho, F. Graffitti, V. D'Ambrosio, B. C. Hiesmayr, and F. Sciarrino. Experimental investigation on the geometry of ghz states. *Scientific Reports*, 7(1):13265, 2017.

[104] J.R. Taylor and S.L.L.J.R. Taylor. *Introduction To Error Analysis: The Study of Uncertainties in Physical Measurements*. ASMSU/Spartans.4.Spartans Textbook. University Science Books, 1997.

[105] M. Mitchell. *An Introduction to Genetic Algorithms*. MA: MIT Press, 1996.

[106] P.C. Chu and J.E. Beasley. A genetic algorithm for the generalised assignment problem. *Computers & Operations Research*, 24(1):17 – 23, 1997.

[107] S. Hartmann. A competitive genetic algorithm for resource-constrained project scheduling. *Naval Research Logistics (NRL)*, 45(7):733–750, 1998.

[108] L. Seveso and M. G. A. Paris. Quantum enhanced metrology of Hamiltonian parameters beyond the Cramér-Rao bound. *International Journal of Quantum Information*, 18(03):2030001, 2020.

[109] L. Seveso, M. A. C. Rossi, and M. G. A. Paris. Quantum metrology beyond the quantum Cramér-Rao theorem. *Phys. Rev. A*, 95:012111, 2017.

[110] D. Burgarth, V. Giovannetti, A. N. Kato, and K. Yuasa. Quantum estimation via sequential measurements. *New Journal of Physics*, 17(11):113055, 2015.

[111] F. Piacentini, A. Avella, M. P. Levi, M. Gramegna, G. Brida, I. P. Degiovanni, E. Cohen, R. Lussana, F. Villa, A. Tosi, F. Zappa, and M. Genovese. Measuring incompatible observables by exploiting sequential weak values. *Phys. Rev. Lett.*, 117:170402, 2016.

[112] Y. Aharonov and L. Vaidman. Measurement of the Schrödinger wave of a single particle. *Physics Letters A*, 178(1):38 – 42, 1993.

[113] F. Piacentini, A. Avella, E. Rebufello, R. Lussana, F. Villa, A. Tosi, M. Gramegna, G. Brida, E. Cohen, L. Vaidman, I. P. Degiovanni, and M. Genovese. Determining the quantum expectation value by measuring a single photon. *Nature Physics*, 13(12):1191–1194, 2017.

[114] C. Rovelli. Comment on "meaning of the wave function". *Phys. Rev. A*, 50:2788–2792, 1994.

[115] W. G. Unruh. Reality and measurement of the wave function. *Phys. Rev. A*, 50:882–887, 1994.

[116] G. M. D'Ariano and H. P. Yuen. Impossibility of measuring the wave function of a single quantum system. *Phys. Rev. Lett.*, 76:2832–2835, 1996.

[117] Y. Aharonov, J. Anandan, and L. Vaidman. The meaning of protective measurements. *Foundations of Physics*, 26(1):117–126, 1996.

[118] N. D. Hari Dass and T. Qureshi. Critique of protective measurements. *Phys. Rev. A*, 59:2590–2601, 1999.

[119] J. Uffink. How to protect the interpretation of the wave function against protective measurements. *Phys. Rev. A*, 60:3474–3481, 1999.

[120] S. Gao. *Protective Measurement and Quantum Reality: Towards a New Understanding of Quantum Mechanics*. Cambridge University Press, 2015.

[121] W. M. Itano, D. J. Heinzen, J. J. Bollinger, and D. J. Wineland. Quantum Zeno effect. *Phys. Rev. A*, 41:2295–2300, 1990.

[122] A. L. Migdall, D. Branning, and S. Castelletto. Tailoring single-photon and multiphoton probabilities of a single-photon on-demand source. *Phys. Rev. A*, 66:053805, 2002.

[123] M. M. Müller, S. Gherardini, A. Smerzi, and F. Caruso. Fisher information from stochastic quantum measurements. *Phys. Rev. A*, 94:042322, 2016.

[124] G. Brida, I. P. Degiovanni, M. Genovese, F. Piacentini, P. Traina, A. Della Frera, A. Tosi, A. Bahgat Shehata, C. Scarcella, A. Gulinatti, M. Ghioni, S. V. Polyakov, A. Migdall, and A. Giudice. An extremely low-noise heralded single-photon source: A breakthrough for quantum technologies. *Applied Physics Letters*, 101(22):221112, 2012.

[125] Y. Bromberg, Y. Lahini, E. Small, and Y. Silberberg. Hanbury brown and twiss interferometry with interacting photons. *Nature Photonics*, 4(10):721–726, 2010.

[126] P. Grangier, G. Roger, and A. Aspect. Experimental evidence for a photon anticorrelation effect on a beam splitter: A new light on single-photon interferences. *Europhysics Letters (EPL)*, 1(4):173–179, 1986.

[127] F. Villa, R. Lussana, D. Bronzi, S. Tisa, A. Tosi, F. Zappa, A. Dalla Mora, D. Contini, D. Durini, S. Weyers, and W. Brockherde. Cmos imager with 1024 spads and tdcs for single-photon timing and 3-d time-of-flight. *IEEE Journal of Selected Topics in Quantum Electronics*, 20(6):364–373, 2014.

[128] P. Busch. *The Time–Energy Uncertainty Relation. In: Muga J., Mayato R.S., Egusquiza Í. (eds) Time in Quantum Mechanics.*, volume 734 of *Lecture Notes in Physics*. Springer, Berlin, Heidelberg, 2008.

[129] L. Henderson and V. Vedral. Classical, quantum and total correlations. *Journal of Physics A: Mathematical and General*, 34(35):6899–6905, 2001.

[130] D. Horsman, C. Heunen, M. F. Pusey, J. Barrett, and R. W. Spekkens. Can a quantum state over time resemble a quantum state at a single time? *Proceedings of the Royal Society A: Mathematical, Physical and Engineering Sciences*, 473(2205):20170395, 2017.

[131] A. J. Leggett and A. Garg. Quantum mechanics versus macroscopic realism: Is the flux there when nobody looks? *Phys. Rev. Lett.*, 54:857–860, 1985.

[132] O. Oreshkov, F. Costa, and Č. Brukner. Quantum correlations with no causal order. *Nature Communications*, 3(1):1092, 2012.

[133] Y. Aharonov, S. Popescu, J. Tollaksen, and L. Vaidman. Multiple-time states and multiple-time measurements in quantum mechanics. *Phys. Rev. A*, 79:052110, 2009.

[134] G. Chiribella, G. M. D'Ariano, P. Perinotti, and B. Valiron. Quantum computations without definite causal structure. *Phys. Rev. A*, 88:022318, 2013.

[135] G. C. Knee, S. Simmons, E. M. Gauger, J. J. L. Morton, H. Riemann, N. V. Abrosimov, P. Becker, H.J. Pohl, K. M. Itoh, M. L. W. Thewalt, G. A. D. Briggs, and S. C. Benjamin. Violation of a leggett–garg inequality with ideal non-invasive measurements. *Nature Communications*, 3(1):606, 2012.

[136] J. Dressel, C. J. Broadbent, J. C. Howell, and A. N. Jordan. Experimental violation of two-party leggett-garg inequalities with semiweak measurements. *Phys. Rev. Lett.*, 106:040402, 2011.

[137] A. Avella, F. Piacentini, M. Borsarelli, M. Barbieri, M. Gramegna, R. Lussana, F. Villa, A. Tosi, I. P. Degiovanni, and M. Genovese. Anomalous weak values and the violation of a multiple-measurement leggett-garg inequality. *Phys. Rev. A*, 96:052123, 2017.

[138] Agustin Palacios-Laloy, F. Mallet, F. Nguyen, P. Bertet, D. Vion, D. Esteve, and A. N. Korotkov. Experimental violation of a bell's inequality in time with weak measurement. *Nature Physics*, 6(6):442–447, 2010.

[139] G. Waldherr, P. Neumann, S. F. Huelga, F. Jelezko, and J. Wrachtrup. Violation of a temporal bell inequality for single spins in a diamond defect center. *Phys. Rev. Lett.*, 107:090401, 2011.

[140] J. F. Fitzsimons, J. A. Jones, and V. Vedral. Quantum correlations which imply causation. *Scientific Reports*, 5(1):18281, 2015.

[141] J. L. Pienaar, T. C. Ralph, and C. R. Myers. Open timelike curves violate heisenberg's uncertainty principle. *Phys. Rev. Lett.*, 110:060501, 2013.

[142] S. L. Braunstein and A. K. Pati. Quantum information cannot be completely hidden in correlations: Implications for the black-hole information paradox. *Phys. Rev. Lett.*, 98:080502, 2007.

[143] C. Marletto, V. Vedral, S. Virzì, E.o Rebufello, A. Avella, F. Piacentini, M. Gramegna, I. P. Degiovanni, and M. Genovese. Theoretical description and experimental simulation of quantum entanglement near open time-like curves via pseudo-density operators. *Nature Communications*, 10(1):182, 2019.

[144] C. Marletto, V. Vedral, S. Virzì, E.o Rebufello, A. Avella, F. Piacentini, M. Gramegna, I. P. Degiovanni, and M. Genovese. Non-monogamy of spatio-temporal correlations and the black hole information loss paradox. *Entropy*, 22(1):228, 2020.

[145] V. Coffman, J. Kundu, and W. K. Wootters. Distributed entanglement. *Phys. Rev. A*, 61:052306, 2000.

[146] M. Koashi and A. Winter. Monogamy of quantum entanglement and other correlations. *Phys. Rev. A*, 69:022309, 2004.

[147] D. Bohm, B.J. Hiley, and F.D. Peat. *Quantum Implications: Essays in Honour of David Bohm*. Physics/Philosophy/Psychology. Routledge, 1991.

[148] D. Marolf. The black hole information problem: past, present, and future. *Reports on Progress in Physics*, 80(9):092001, 2017.

[149] D. Deutsch. Quantum mechanics near closed timelike lines. *Phys. Rev. D*, 44:3197–3217, 1991.

[150] P.J. Nahin. *Time Machines: Time Travel in Physics, Metaphysics, and Science Fiction*. Springer New York, 2001.

[151] S. Krasnikov. Time travel paradox. *Phys. Rev. D*, 65:064013, 2002.

[152] S.W. Hawking and G.F.R. Ellis. *The Large Scale Structure of Space-Time*. Cambridge Monographs on Mathematical Physics. Cambridge University Press, 1973.

[153] S. Lloyd, L. Maccone, R. Garcia-Patron, V. Giovannetti, Y. Shikano, S. Pirandola, L. A. Rozema, A. Darabi, Y. Soudagar, L. K. Shalm, and A. M. Steinberg. Closed timelike curves via postselection: Theory and experimental test of consistency. *Phys. Rev. Lett.*, 106:040403, 2011.

[154] T. A. Brun, J. Harrington, and M. M. Wilde. Localized closed timelike curves can perfectly distinguish quantum states. *Phys. Rev. Lett.*, 102:210402, 2009.

[155] M. Ringbauer, M. A. Broome, C. R. Myers, A. G. White, and T. C. Ralph. Experimental simulation of closed timelike curves. *Nature Communications*, 5(1):4145, 2014.

[156] C. H. Bennett, D. Leung, G. Smith, and J. A. Smolin. Can closed timelike curves or nonlinear quantum mechanics improve quantum state discrimination or help solve hard problems? *Phys. Rev. Lett.*, 103:170502, 2009.

[157] T. C. Ralph and T. G. Downes. Relativistic quantum information and time machines. *Contemporary Physics*, 53(1):1–16, 2012.

[158] X. Yuan, S. M. Assad, J. Thompson, J. Y. Haw, V. Vedral, T. C. Ralph, P. K. Lam, C.n Weedbrook, and M. Gu. Replicating the benefits of deutschian closed timelike curves without breaking causality. *npj Quantum Information*, 1(1):15007, 2015.

[159] T. A. Brun, M. M. Wilde, and A. Winter. Quantum state cloning using deutschian closed timelike curves. *Phys. Rev. Lett.*, 111:190401, 2013.

[160] D. Ahn, C. R. Myers, T. C. Ralph, and R. B. Mann. Quantum-state cloning in the presence of a closed timelike curve. *Phys. Rev. A*, 88:022332, 2013.

[161] J. L. Pienaar, T. C. Ralph, and C. R. Myers. Open timelike curves violate heisenberg's uncertainty principle. *Phys. Rev. Lett.*, 110:060501, 2013.

[162] B. Toner. Monogamy of non-local quantum correlations. *Proceedings of the Royal Society A: Mathematical, Physical and Engineering Sciences*, 465(2101):59–69, 2009.

[163] G. Brida, M. V. Chekhova, M. Genovese, M. Gramegna, and L. A. Krivitsky. Dispersion spreading of biphotons in optical fibers and two-photon interference. *Phys. Rev. Lett.*, 96:143601, 2006.

[164] W. G. Unruh and R. M. Wald. Information loss. *Reports on Progress in Physics*, 80(9):092002, 2017.

[165] S. W. Hawking, M. J. Perry, and A. Strominger. Soft hair on black holes. *Phys. Rev. Lett.*, 116:231301, 2016.

[166] S. Choudhury, S. Panda, and R. Singh. Bell violation in the sky. *European Physical Journal C*, 77(2):60, 2017.

[167] J. Martin and V. Vennin. Obstructions to bell cmb experiments. *Phys. Rev. D*, 96:063501, 2017.

[168] J. Maldacena. A model with cosmological bell inequalities. *Fortschritte der Physik*, 64(1):10–23, 2016.

[169] S. Choudhury and S. Panda. Retracted article: Spectrum of cosmological correlation from vacuum fluctuation of stringy axion in entangled de sitter space. *The European Physical Journal C*, 80(1):67, 2020.

[170] S. W. Hawking. Black holes in general relativity. *Communications in Mathematical Physics*, 25(2):152–166, 1972.

[171] S. W. Hawking. Particle creation by black holes. *Communications in Mathematical Physics*, 43(3):199–220, 1975.

[172] S. W. Hawking. Breakdown of predictability in gravitational collapse. *Phys. Rev. D*, 14:2460–2473, 1976.

[173] S. W. Hawking. Information loss in black holes. *Phys. Rev. D*, 72:084013, 2005.

[174] D. N. Page. Information in black hole radiation. *Phys. Rev. Lett.*, 71:3743–3746, 1993.

[175] D. Wallace. Why black hole information loss is paradoxical, *arXiv preprint*, 2018.

[176] C.W. Misner, K.S. Thorne, J.A. Wheeler, W.H. Freeman, and Company. *Gravitation*. Number pt. 3 in Gravitation. W. H. Freeman, 1973.

[177] D. Deutsch. Qubit field theory, preprint at https://arxiv.org/abs/quant-ph/0401024v1. 2004.

[178] G. Rubino, L. A. Rozema, A. Feix, M. Araújo, J. M. Zeuner, L. M. Procopio, Č. Brukner, and P. Walther. Experimental verification of an indefinite causal order. *Science Advances*, 3(3), 2017.